TECHNISCHE UNIVERSITÄT MÜNCHEN

Fachgebiet Hydromechanik

Unsteady porous-media flows

Tao Zhu

Vollständiger Abdruck der an der Ingenieurfakultät Bau Geo Umwelt der Technischen Universität zur Erlangung des akademischen Grades eines

Doktor-Ingenieurs

genehmigten Dissertation.

Vorsitzender:	Prof. Dr.-Ing. Markus Disse
Prüfer der Dissertation:	
	1. Prof. Dr.-Ing. Michael Manhart
	2. Prof. Dr. rer. nat. Barbara Wohlmuth
	3. Prof. Dr.-Ing. Rainer Helmig, Universität Stuttgart (nur schriftliche Beurteilung)

Die Dissertation wurde am 28.10.2015 bei der Technischen Universität München eingereicht und durch die Ingenieurfakultät Bau Geo Umwelt am 07.04.2016 angenommen.

Abstract

This PhD thesis mainly consists of three parts.
In part one, unsteady and linear porous-media flow is considered, and the behavior of the coefficients in the unsteady Darcy equation is investigated. One of the coefficients, the time scale, can be obtained by consistent volume-averaging of the Navier-Stokes (VANS) equations together with a closure for the interaction term. Two different closures can be found in the literature, a steady-state closure and a virtual mass approach considering unsteady effects. These approaches are contrasted with an unsteady form of Darcy's equation derived by volume-averaging the equation for the kinetic energy. A series of direct numerical simulations (DNS) of unsteady flow in the pore space with various complexities is used to assess the applicability of the unsteady Darcy equation with constant coefficients. The results imply that the new kinetic energy approach shows perfect agreement for transient flow in porous media. The time scale predicted by this approach represents the ratio between the integrated kinetic energy in the pore space and that of the intrinsic velocity. This ratio can be significantly larger than that obtained by VANS using the steady-state closure for the flow resistance term.
In part two, the extension of part one into oscillatory (sinusoidal) flow is investigated. DNS has been performed to benchmark the analytical solutions of the unsteady Darcy equation with the time scales obtained by VANS with a steady-state closure, and by the energy approach. For small and medium frequencies, the analytical solutions with the time scale by the energy approach compare well with the DNS results in terms of amplitude and phase lag. For large dimensionless frequencies ($\omega\tau \gtrsim 10$) the time scale obtained by the energy approach is slightly bigger than the DNS results, and it can be explained in a change in the velocity fields toward a potential flow solution. However, the time scale predicted by the VANS approach with a steady-state closure is too small. In general, this study supports the use of the unsteady Darcy equation with constant coefficients to solve oscillatory Darcy flow, provided, the proper time scale has been found.
In part three, unsteady and non-linear porous-media flow is considered. The physical quantity that determines the instants at which the non-linear effects set in (onset) is searched, and the applicability of the unsteady Forchheimer equation with constant coefficients has been investigated. Mathematical expressions have been derived to describe the onset of the non-linear effects, and a series of direct numerical simulations (DNS) of unsteady flow in the pore space with various complexities is used to assess these questions. The results imply that, instead of the instantaneous pore Reynolds number, the Stokes Reynolds number based on the Stokes boundary layer thickness should be considered to examine the onset of the non-linear effects. Moreover, the DNS results show that some non-linear flows subjected to a sudden step change in pressure gradient experience overshoot in superficial velocity before the steady-state takes place, and this overshoot can hardly be expressed by the unsteady Forchheimer equations with constant coefficients.

Preface

After finishing my undergraduate study in Mechanical engineering and graduate study in Computational Mechanics, I made an important decision to do a PhD research at Fachgebiet Hydromechanik, Technical University Munich, in Computational Fluid Dynamics (CFD). My topic concerns unsteady porous-media flows, their mathematical modeling on a macroscopic level and assessment of these models using Direct Numerical Simulations (DNS). I made this decision simply because this research consists of some subjects that I became mostly interested in since middle school: mathematics and physics. Besides of that, fluid dynamics, building mathematical models, programming and solving equations numerically have been introduced to me as very interesting tasks already since my university time. Another big reason for me to do this research is that, because some example applications are in the oil industry and in environmental engineering, the study in porous-media flows would give a contribution to the protection of the environment, no matter how big or small the contributions one can make. The target group for which my thesis is written includes mostly scientific researchers and engineers who might think about the flows inside porous media.

I would like to first give my thanks to my advisor Prof. Dr.-Ing. habil. Michael Manhart. Without his extraordinary constructive guidance and continuous solid support, this work could never have been done. I have always been benefiting from his deep knowledge, his kindness and intelligence, and the long scientific discussions I have had with him.

My special thanks to Prof. Dr. rer. Barbara Wohlmuth for being my second mentor, providing solid support from the numerical mathematics chair, giving extraordinary and excellent guidance, and for building up an amazing interdisciplinary research team under the framework of the International Graduate School of Science and Engineering (IGSSE). It has always been a honour for me to work with mathematicians, as their deep knowledge and special talents always make the scientific discussions highly interesting.

I also would like to thank Prof. Dr.-Ing. Reiner Helmig from Stuttgart, who is always a nice and warm-hearted person and supported me during my difficult times.

Many thanks to Dr. Christian Waluga, for his special contributions in being an excellent project team leader, and for his productive discussions in scientific problems and impressively trained skills in scientific writting. I also would like to give thanks to my colleague Sheema Kooshapur, with whom I held many scientific discussions. Thanks to the rest of my colleagues, such as Wolfgang Schanderl, Daniel Quosdorf, Claudia Strobl and Evelyn Wegner, for supporting me in my time at the Fachgebiet Hydromechanik.

I would especially like to thank my wife, Yi Hu, and my parents, Fuzhong Zhu and Ling Hua, who gave me continuous and solid support in the past years. Without them, I could have never completed this work.

Financial support from the International Graduate School of Science and Engineering (IGSSE)

of the Technische Universität München for research training group 6.03 is gratefully acknowledged.

Contents

List of Tables

List of Figures

Nomenclature

Roman letters

A	interfacial area between solid and fluid phases
A_m	amplitude of the oscillatory superficial velocity
A_Q	cross-sectional area of a certain flow rate
a	coefficient of the linear velocity term in Darcy's law
B	blockage ratio
b	coefficient of the quadratic velocity term in Forchheimer equation
C_{vm}	virtual mass coefficient
c	coefficient of the derivative term in unsteady Darcy Eq.
D	cylinder/sphere diameter
d	pore diameter
$\mathbf{e}_x$	unit vector in x-direction
$\boldsymbol{F}$	Forchheimer tensor
F	Forchheimer coefficient
F_0	Forchheimer number
$\boldsymbol{g}$	gravitational force
H	pore pacing
h	half channel width
$\boldsymbol{I}$	unit matrix
J_0	Bessel function of order zero
J_1	Bessel function of order one
$\boldsymbol{K}$	permeability tensor
K	permeability
K_D	Darcy permeability
L	macroscopic scale
l	pore scale
m	exponent of the non-linear term
$\boldsymbol{n}$	unit outwardly directed normal vector
$\boldsymbol{O}$	order of magnitude
p	pressure
p_x	x component of the pressure gradient
Q	flow rate
r	distance to the center of a pipe
R	radius of a pipe
$\Re$	real part
Re	Reynolds number
Re_{pore}	pore Reynolds number

Re_{Stokes}	Stokes Reynolds number
r_0	radius of the averaging volume
$\boldsymbol{s}$	symmetric part of the velocity gradient
t	time
U	macroscopic mean velocity
$\boldsymbol{u}$	velocity vector
u	velocity component
V	averaging volume
x	position parameter

Greek letters

α	Wormersley number
β	fluid phase
δ	ratio between micro and macro scales
δ^ν	viscous layer depth
ϵ	porosity
μ	dynamic viscosity of fluid
ν	kinematic viscosity of fluid
ρ	mass density of fluid
σ	solid phase
σ_u	deviation of the normalized non-linear superficial velocity from the linear ones
τ	time scale
τ_{dns}	time scale measured from DNS
τ_{en}	time scale derived from the energy approach
τ_{vans}	time scale derived from the VANS system with a steady-state closure
τ_{vm}	time scale derived from the VANS system with a virtual mass closure
ϕ	phase lag
Θ	constant part of the oscillating pressure gradient
Ψ	oscillatory part of the oscillating pressure gradient
φ	arbitrary physical quantity
ω	oscillatory frequency

Symbols

div	divergence
$\langle\cdots\rangle_{\text{i}}$	intrinsic volume-averaging operator
$\langle\cdots\rangle_{\text{s}}$	superficial volume-averaging operator
$\widetilde{\cdots}$	spatial deviation
:	Frobenius inner product
$\boldsymbol{\nabla}$	Nabla operator in physical space
∂_t	time derivative
∂V	spatial boundaries

1 Introduction

1.1 Unsteady porous-media flow

A porous medium is a substance that contains pores or spaces between solid material through which liquid or gas can pass. Unsteady flows in porous media play an important role in many various fields of technical applications and environmental problems. Some examples are listed as follows.

The catalytic converter in a vehicle allows the conversion from harmful compounds to less harmful ones, mainly the conversion from Nitrogen Oxides, hydrocarbons and Carbon Monoxide to Nitrogen, water and Carbon Dioxide (Martínez-Martínez et al., 2010). Because of the flow complexity, it is essentially a difficult task for engineers to optimize the geometry, characteristics and position of the catalytics in order to increase conversion efficiency and engine performance (D'Errico et al., 2000). Because the catalytic substances such as platinum or palladium usually lie on a ceramic porous bed, porous media flow models have been adopted by many researchers to investigate these problems (Żmudka and Postrzednik, 2011; Laxmi et al., 2013; Wahid, 2014). Many researchers also noted that due to significant pressure and temperature oscillations, the exhaust flow is unsteady (D'Errico et al., 2000; Hwang et al., 2007).

Fischer-Tropsch synthesis, which is responsible for conversion of synthesis gas (carbon monoxide and hydrogen mixture) into a mixture of linear hydrocarbons, is the most common stage in Gas-to-liquids technology. Active catalysts might help to realize the high conversion performance. The recent work of Ermolaev et al. (2015) has shown that unsteady porous media flow models can be applied to model gas flow through Multitubular fixed-bed reactors in the Fischer-Tropsch synthesis industry.

In the cooling system of gas turbines, e.g., coolant gas transfers through a porous wall which requires cooling, resulting mixing between coolant gas and hot gas stream on the other side of the wall. The mixed gas layer lies between the warmer surface of the porous wall and the hot gas stream, which reduces the heat flux from the hot gas to the porous wall, thus increases thermodynamic efficiencies. Such a process is referred to as transpiration cooling (Cerri et al., 2007). For such problems, Dahmen et al. (2013) and Huang et al. (2014) have conducted numerical simulations using porous media models, but are restricted in steady-state solutions. Swapna and Varmab (2014) however, focused on unsteady results.

Bioheat usually refers to heat transfer in human tissues. Example processes are heat conduction, heat transfer due to blood convection and metabolic heat generation (Khaled and Vafai, 2003). Attempts have been carried out by biomedical engineers to set up accurate models for bioheat, since it is the basis for the human thermotherapy and thermoregulation system (Sanyal and Maji, 2001; Khaled and Vafai, 2003). These models can be developed either by the mixture theory of continuum mechanics or by the porous-media theory (Fan

and Wang, 2011). In the porous media theory unsteady flows have been considered for mass diffusion, flow convection and bioheat equations in blood flow (Fan and Wang, 2011; Khaled and Vafai, 2003).
Submerged aquatic canopies describe many benthic organisms forming very rough surfaces on the sea floor. The flow structure within them can significantly affect the ecology of the benthic organisms and the biological processes such as nutrient exchange and uptake. In turn the presence of the porous submerged canopies affect the hydromechanics occurring withing them (Lowe et al., 2008). Understanding the flow structure within the canopies is of significant importance. Submerged canopies in general constitute porous media. In the ocean they will be exposed to nearly oscillatory (Lowe et al., 2005) and thus unsteady flow due to the wave motion.
The Earth's terrestrial vegetation plays an important role in the hydrological, nitrogen, and phosphorus cycles. The oxidation capacity or cleansing ability of the atmosphere, e.g., can be significantly influenced by a variety of chemical compounds that are produced by living foliage (Fuentes et al., 2000; Guenther et al., 2006). Thus understanding the processes in plant canopy-atmosphere exchange is of critical importance for weather, climate and environmental forecasting as well as for agricultural and natural resource management (Patton and Finnigan, 2013). In many cases plant canopies constitute porous media, and the heat and mass transfer between a canopy and the atmospheric boundary layer is governed by the turbulent flow which is unsteady (Finnigan, 2000).
In places where it is snow covered for most of the year, the chemistry of the atmosphere and the underlying snow and firn is affected by snow-air exchanges (Albert and Shultz, 2002). The production of CO_2 in the frozen soil and how it is transported to the atmosphere also affect the annal CO_2 generation (Winston et al., 1995). In general, understanding the transfer process of gas and other chemical species (e.g. CO_2) through the upper layers of soil and/or snow is of significant important for geological studies concerning glacial ice or climatology studies concerning CO_2 generation. These processes are influenced by unsteady turbulent pressure fluctuations. This effect has been commonly treated under the term *pressure pumping* (Bowling and Massman, 2011; Maier et al., 2011).
So far, a unique description and modeling of these unsteady flow problems cannot be found in the literature, and different concepts on how to treat them exist.

1.2 Main approaches

Porous-media flows can be classified not only into *steady* and *unsteady* flows, depending on whether the physical quantities inside the fluids vary with respect to time, but also into *linear* and *non-linear* flows (if we do not consider turbulence), depending on whether the macroscopic pressure gradient is linear to the macroscopic mean velocity. For different combinations of these classifications, different governing equations must be considered to describe the flows on the macro scale.
Steady and *linear* porous-media flows take place when the flow is steady and with a very low pore Reynolds number $Re_{\text{pore}} = \frac{Ud}{\nu}$, where U is the macroscopic mean velocity, d is the pore size and ν is the kinematic viscosity. In such flows, the viscous forces are dominant, and the

Darcy's law

$$\boldsymbol{\nabla} p = aU, \tag{1.1}$$

is commonly applied to predict the flow on the macro scale(Darcy, 1856), which states that the macroscopic pressure gradient $\boldsymbol{\nabla} p$ is balanced by a linear term of the macroscopic mean velocity U, and the coefficient a represents the linear part of the interaction force.
For *steady* and *non-linear* flows, the pore Reynolds number Re_{pore} is usually larger than 1, and inertia effects gain weight. The macroscopic pressure gradient becomes non-linear to the macroscopic mean velocity. A quadratic macroscopic velocity term(Forchheimer, 1901) has been added to correct the momentum balance

$$\boldsymbol{\nabla} p = aU + bU^2, \tag{1.2}$$

where the coefficient b represents the quadratic part of the interaction force. This equation is called the *Forchheimer equation*.
For *unsteady* and *linear* flows, a phase shift between pressure drop and macroscopic mean velocity can exist (Laushey and Popat, 1968). It results from the inertia of the accelerated fluid, and must be represented by a time derivative of the mean velocity. The resulting equation can be written as the *unsteady Darcy equation*(Burcharth and Andersen, 1995; Kuznetsov and Nield, 2006; Rajagopal, 2007; Sollitt and Cross, 1972)

$$\boldsymbol{\nabla} p = aU + c\,\partial_t U, \tag{1.3}$$

where the coefficient c represents the inertia term due to flow acceleration.
For *unsteady* and *non-linear* flows, many researchers (Gu and Wang, 1991; Hall et al., 1995; Burcharth and Andersen, 1995; Lowe et al., 2005) used the *unsteady Forchheimer equation*

$$\boldsymbol{\nabla} p = aU + bU^2 + c\,\partial_t U, \tag{1.4}$$

to describe the flow.
A summary of the macroscopic governing equations in different flow regimes can be found in Fig. 1.1.
In steady flows, for both Darcy's law (1.1) and Forchheimer equation (1.2), general mathematical expressions of the coefficients a and b have already been determined from experiments (Darcy, 1856; Forchheimer, 1901). Both equations (1.1) and (1.2) have been proved to be accurate when describing steady flows on the macro scale (for details, see section 2.2).
While in unsteady flows, a full agreement between experimental results and behavior predicted by the unsteady Darcy and Forchheimer equations (1.3) and (1.4) with fitted co-

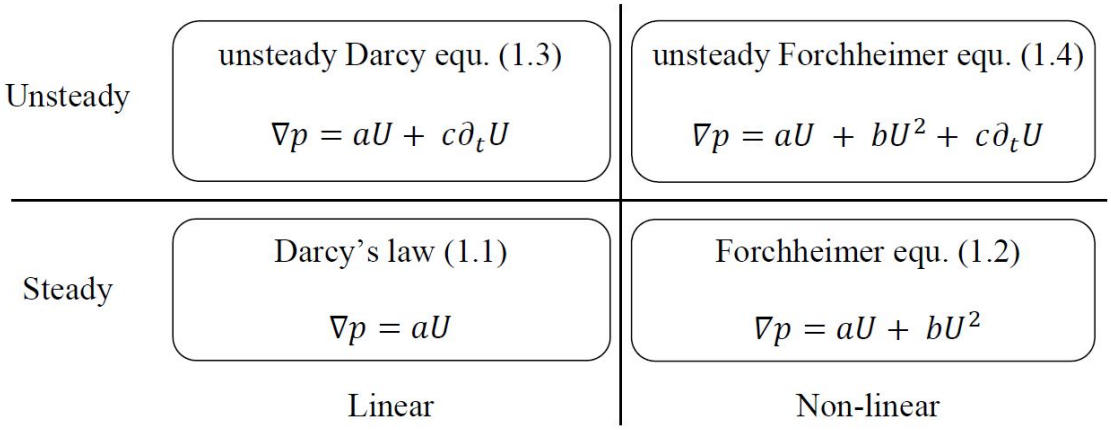

Figure 1.1: Macroscopic governing equations in different flow regimes

efficients has not yet been achieved, although attempts have been made to determine the coefficients a, b, and c from experiments (Gu and Wang, 1991; Hall et al., 1995; Burcharth and Andersen, 1995; Lowe et al., 2005). One could assume a and b in unsteady problems to have the same values as those in steady problems, and verify this later in experiments; the coefficient c, however, is essentially the most difficult part in these problems. Agreements on a general mathematical expression of c for all porous mediums have never been made.

For *unsteady* and *linear* flows, the general mathematical expression for this coefficient c (or the time scale $\tau = c/a$) can mainly be derived with the so-called *Volume-Averaged Navier-Stokes (VANS)*(Whitaker, 1986, 1996) approach. It defines a volume-averaging operator, which integrates any physical quantity inside a *Representative Elementary Volume (REV)* and divide it by the volume, leading to an averaged quantity. Applying the volume-averaging operator to the momentum equation of the Navier-Stokes equations, Whitaker (1996) derived the volume averaged momentum equation. However, in such a system of the averaged equations, the number of the unknowns are greater than the number of the equations, thus a closure is required, in order to make the system of equations solvable. Whitaker (1996) proposed that the interaction term at the pore/grain interface could be closed by the steady-state Darcy and Forchheimer approximations. Under the conditions of unidirectional flow through isotropic, homogeneous material at low Reynolds number, this equation can be written with a structure identical to that of the unsteady Darcy equation (1.3), and c (or $\tau = c/a$) can be determined. Another closure which can be used to close the averaged momentum equations in the VANS approach results from the so-called *virtual mass* approach, which was proposed by Sollitt and Cross (1972) to account for the inhomogeneity of the flow field surrounding individual structures in the porous material during transient flow, when inertial nonlinearities cannot be neglected. Applying such a closure to the volume-averaged momentum equations also results in the same form of the unsteady Darcy equation (1.3), and one can obtain another mathematical expression of c (or $\tau = c/a$). However, in this way it results in a larger time scale in unsteady porous media flow, compared to the VANS approach with steady-state closure. To the author's best knowledge, a systematic comparison and assessment of the different formulations of the unsteady Darcy equation (1.4) and of the

coefficient c has not been done so far.
Many difficulties are exposed when only exploring *unsteady* and *linear* flows; while for *unsteady* and *non-linear* flows, the situations are even more complicated. The first questions one could instantly come across might be: at which instants do the non-linear effects set in, and which physical variable determines the 'onset' (starting point) of these instants in *unsteady* porous-media flows? In *steady* porous-media flows, the answer to these questions seems to be very simple: when the pore Reynolds number is comparable to unity, the non-linear effects set in (e.g. Lasseux et al., 2011). While in unsteady porous-media flows, this is not yet verified. More importantly, we still do not know if the unsteady Forchheimer equation (1.4) with constant coefficient a, b and c can be used to describe *unsteady* and *non-linear* flows on the macroscopic scale very accurately. This needs to be assessed. There are still too many questions remain unanswered in *unsteady* and *non-linear* flows, and this PhD thesis only aims to answer a few of them.

1.3 Global problem statement

This PhD thesis mainly aims to answer the following questions:

- For *unsteady* and *linear* flows, is the unsteady Darcy equation (1.3) together with constant coefficients accurate, and can it be used to describe these flows on the macroscopic scale?
- Is there a general mathematical expression for the coefficient c in unsteady Darcy equation (1.3)? If yes, what is it?
- What would be the case in *linear*, oscillatory flows? Is the unsteady Darcy equation (1.3) accurate in all frequency ranges?
- For *unsteady* flows, which physical variable determines the onset of the non-linear effects?
- For *unsteady* and *non-linear* flows, is the unsteady Forchheimer equation (1.4) together with constant coefficients accurate, and can it be used to describe these flows on the macroscopic scale?

2 State of the Art

2.1 Mathematical descriptions of porous media flow

There are different ways of mathematical descriptions of porous media flow. On the pore scale, the flow is normally described by the Navier-Stokes equations. While on the macroscopic scale, since macro scale is far larger than the pore scale, a full resolution of the pore scale costs too much computational power. Thus applying models such as the VANS is necessary. In this section, we discuss about these mathematical descriptions.

2.1.1 Navier-Stokes equations

On the microscopic scale, the incompressible flow of a Newtonian fluid through a porous medium can be described by the *Navier-Stokes equations*:

$$\rho \partial_t \boldsymbol{u} + \rho \boldsymbol{u} \cdot \boldsymbol{\nabla} \boldsymbol{u} = -\boldsymbol{\nabla} p + \rho \boldsymbol{g} + \mu \boldsymbol{\nabla}^2 \boldsymbol{u}, \tag{2.1}$$

$$\operatorname{div} \boldsymbol{u} = 0, \tag{2.2}$$

where ρ denotes the density of the fluid, p denotes the pressure field and $\boldsymbol{u}$ denotes the (Eulerian) velocity field. The gravitational force $\boldsymbol{g}$ will be dropped in the next sections, as it could be lumped together with the pressure term. The convective operator is defined as usual, i.e., $\boldsymbol{u} \cdot \boldsymbol{\nabla} \boldsymbol{u} := \sum_{i=1}^{d} u_i \, \partial_{x_i} \boldsymbol{u}$.
The Navier-Stokes equations are derived by applying Newton's second law to a continuum, the principle of mass conservation and a constitutive law which relates the shear stresses in a fluid to the rate of deformation of a fluid element.
To solve the Navier-Stokes equations without applying any additional mathematical models, one applies the *Direct Numerical Simulations (DNS)*. In this method all turbulent eddies in turbulent flow ranging from the large scale (L) down to the Kolmogorov scale (η) are resolved by very fine computational grids. The ratio between large and small scales is given by $Re^{3/4}$. Thus, because of three dimensionality of the flow, the number of grid points (and thus the required memory) scales with $Re^{9/4}$. As a result, DNS is a very clean but expansive tool for solving the Navier-Stokes equations in turbulent flow. In laminar flows however, the Kolmogorov scales do not exit and thus grid study is necessary to determine the overall grid resolution.

2.1.2 Volume-Averaged Navier-Stokes

On the computational basis, theoretically all of the unsteady porous media flow problems can be solved by Direct Numerical Simulations (DNS). However, due to the fact that in most cases the macroscopic flow domain is far larger than the pore scale, fully resolving the pore scales requires a huge amount of computational power. Thus building mathematical models for computations with coarser grids is necessary.
The *volume-averaging* procedure has been applied by many authors to investigate steady-state porous-media flow in early studies (Bear, 1972; Gray and O'Neill, 1976; Hassanizadeh and Gray, 1979; Shapiro, 1981; Slattery, 1969; Whitaker, 1969), and further developed by Whitaker (1986, 1996), being applied on Stokes and Navier-Stokes equations, which can be used to derive the Darcy's law and the Forchheimer equation.
For consistency with the prior work of Whitaker (1986), we denote the fluid phase by β and the solid phase by σ. Figure 2.1 illustrates the β and σ phases in flow in a rigid porous medium.
The averaging volume is denoted by V, and V_β denotes the volume occupied by the fluid. The *superficial average* of any physical quantity φ that is associated with the fluid phase β is defined by

$$\langle\varphi\rangle_{\mathrm{s}} = \frac{1}{|V|}\int_{V_\beta} \varphi \, \mathrm{d}x. \tag{2.3}$$

We also introduce the *intrinsic average*

$$\langle\varphi\rangle_{\mathrm{i}} = \frac{1}{|V_\beta|}\int_{V_\beta} \varphi \, \mathrm{d}x, \tag{2.4}$$

which is related to the superficial average by $\langle\varphi\rangle_{\mathrm{s}} = \epsilon\langle\varphi\rangle_{\mathrm{i}}$, where the ratio of the volumes $\epsilon = |V_\beta|/|V|$ denotes the *porosity*. Let us recall that we can decompose any physical quantity $\varphi = \langle\varphi\rangle_{\mathrm{i}} + \widetilde{\varphi}$ into its *intrinsic average* $\langle\varphi\rangle_{\mathrm{i}}$ and a *spatial deviation* $\widetilde{\varphi}$ (Whitaker, 1986). Figure 2.2 gives an illustration of macroscopic porous medium and local volume for averaging.
Whitaker (1986) applied the volume-averaging operator to the Stokes equations

$$0 = -\boldsymbol{\nabla} p + \rho \boldsymbol{g} + \mu \boldsymbol{\nabla}^2 \boldsymbol{u}, \tag{2.5}$$

$$\operatorname{div} \boldsymbol{u} = 0, \tag{2.6}$$

where the gravitational force $\boldsymbol{g}$ will be dropped at this point,as it could be lumped together with the pressure term, obtaining an averaged form of the Stokes equations:

$$0 = -\langle\boldsymbol{\nabla} p\rangle_{\mathrm{s}} + \left\langle\mu \boldsymbol{\nabla}^2 \boldsymbol{u}\right\rangle_{\mathrm{s}}, \tag{2.7}$$

$$\langle\operatorname{div} \boldsymbol{u}\rangle_{\mathrm{s}} = 0. \tag{2.8}$$

Note that two important assumptions has been applied to help further derive the averaged Stokes equations, which are the length constraint and the relation between the average of a gradient and the gradient of an average. The former (Whitaker, 1986) is defined as

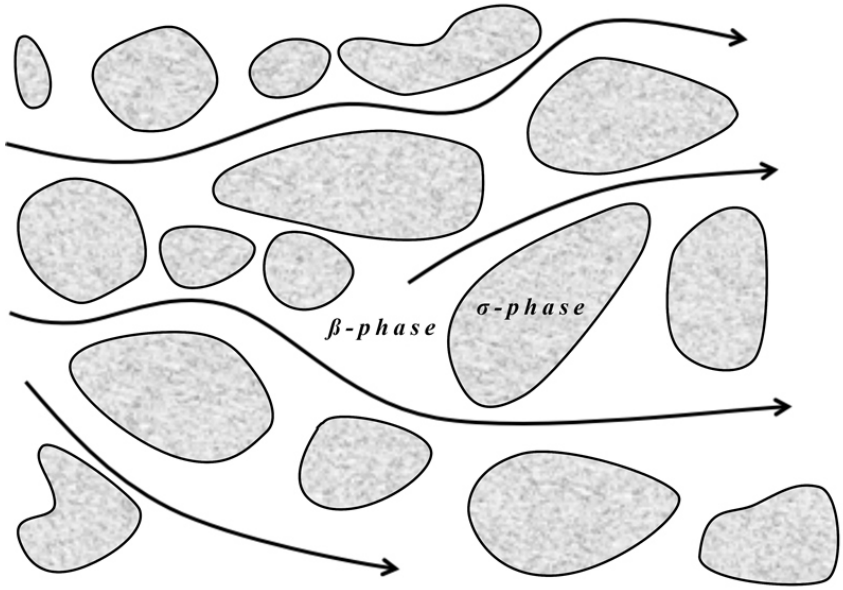

Figure 2.1: Illustration of flow through a rigid porous medium

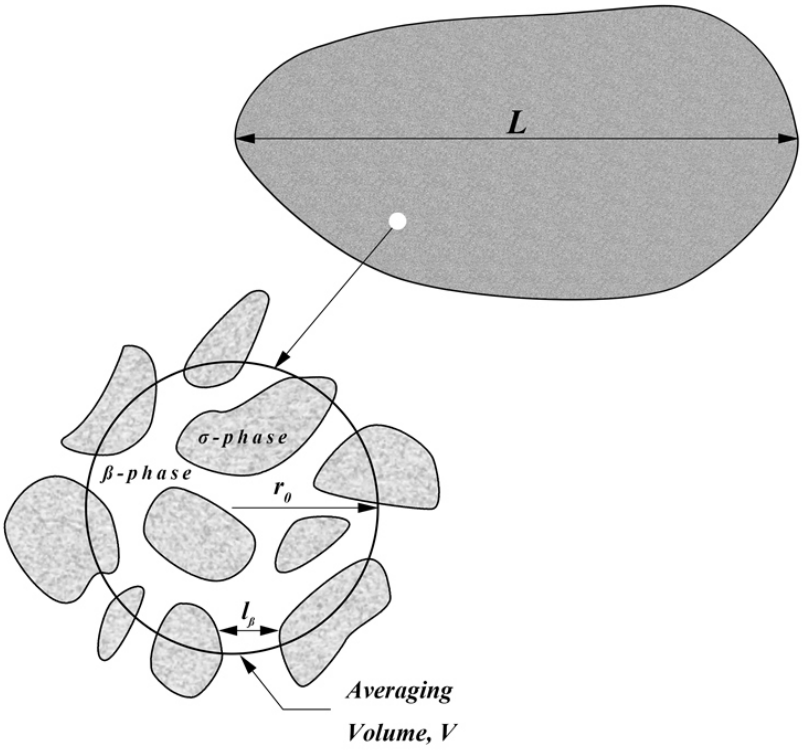

Figure 2.2: Illustration of macroscopic porous medium and local volume for averaging

$$l \ll r_0 \ll L, \tag{2.9}$$

where r_0 is the radius of the averaging volume, l is the pore scale and L is the macroscopic scale, while the latter (Anderson and Jackson, 1967; Marle, 1967; Slattery, 1967; Whitaker, 1967) is defined as

$$\langle \boldsymbol{\nabla}\varphi \rangle_{\mathrm{s}} = \boldsymbol{\nabla}\langle \varphi \rangle_{\mathrm{s}} + \frac{1}{|V|}\int_{A_{\beta\sigma}} \boldsymbol{n}_{\beta\sigma}\varphi \, \mathrm{d}A, \tag{2.10}$$

where $A_{\beta\sigma}$ represents the interfacial area between fluid and solid contained within the averaging volume and $\boldsymbol{n}_{\beta\sigma}$ represents the unit outwardly directed normal vector for the fluid phase.
These assumptions (2.9) and (2.10) can be used to derive the final volume-averaged Stokes equation from equation (2.7):

$$0 = -\boldsymbol{\nabla}\langle p \rangle_{\mathrm{i}} + \underbrace{\frac{1}{|V_\beta|}\int_{A_{\beta\sigma}} \boldsymbol{n}_{\beta\sigma} \cdot (-\tilde{p}\boldsymbol{I} + \mu\boldsymbol{\nabla}\tilde{\boldsymbol{u}}) \; dA}_{\text{surface filter}}. \tag{2.11}$$

The second term on the right side of equations (2.11) is named later by Whitaker (1996) as a *surface filter*, which represents the drag due to surface forces at the fluid-solid interface. It is identical to what Rajagopal (2007) referred to as an *interaction term*. The surface filter consists of spatial deviation terms $\tilde{p}$ and $\tilde{\boldsymbol{u}}$, and the result is that the number of unknowns is greater than the number of equations in the system, and thus the system cannot be solved without a *closure* term. To close the system, spatial deviations must be converted to averaged quantities. Whitaker (1986) proposed that for steady flow with very small pore Reynolds number, the *steady-state closure* for the surface filter consists the superficial velocity $\langle \boldsymbol{u} \rangle_{\mathrm{s}}$ and the *permeability tensor* $\boldsymbol{K}$, where $\boldsymbol{K}$ can be determined by solving some boundary value problems in a *Representative Elementary Volume (REV)*, which would be treated as a unit cell in a spatially periodic porous medium, and is far away from the macroscopic boundaries, i.e., inlet and outlet of the fluid that is contained within the porous medium. Inserting this closure back to equation (2.11) would eventually lead to the Darcy's law. Whitaker (1986) noted that the solution of $\boldsymbol{K}$ by means of the boundary value problems represents a formidable computational problem, and that a unit cell in a spatially periodic porous medium will be used to determine $\boldsymbol{K}$. This procedure can be easily applied and solved in simple systems with spatially periodic unit cells, such as a bundle of capillary tubes (Whitaker, 1986).
A more developed procedure is provided by Whitaker (1996) to represent steady flow in greater pore Reynolds numbers. In this case the Forchheimer effects due to inertia of fluids must be counted (For more details, see section 2.2.2).
Applying the volume-averaging to the Navier-Stokes equations (2.1) and using the length constraints (2.9) and equation (2.10), Whitaker (1996) eventually derived the following form

of the Volume-Averaged Navier-Stokes

$$\begin{aligned}\rho\partial_t\langle\boldsymbol{u}\rangle_{\mathrm{i}} + \rho\langle\boldsymbol{u}\rangle_{\mathrm{i}}\operatorname{div}\langle\boldsymbol{u}\rangle_{\mathrm{i}} + \underbrace{\rho\epsilon^{-1}\operatorname{div}\langle\tilde{\boldsymbol{u}}\tilde{\boldsymbol{u}}\rangle_{\mathrm{s}}}_{\text{volume filter}} \\ = -\boldsymbol{\nabla}\langle p\rangle_{\mathrm{i}} + \underbrace{\mu\boldsymbol{\nabla}^2\langle\boldsymbol{u}\rangle_{\mathrm{i}}}_{\text{Brinkman correction}} + \underbrace{\frac{1}{|V_\beta|}\int_{A_{\beta\sigma}}\boldsymbol{n}_{\beta\sigma}\cdot\left(-\tilde{p}\boldsymbol{I}+\mu\boldsymbol{\nabla}\tilde{\boldsymbol{u}}\right)\,dA}_{\text{surface filter}}.\end{aligned} \tag{2.12}$$

Whitaker (1996) considered quasi-steady flow and ignored the time derivative term on the left hand side. He also argued that for non-linear flow the second and third terms on the left hand side are small compared to the surface filter, using order-of-magnitude arguments, the length constraints (2.9) and the concept of *inertial length* (Whitaker, 1982). The Brinkmann term on the right hand side can also be ignored under the length constraints (2.9). For non-linear flow, the surface filter is closed by a steady-state closure which consists of a permeability term linear to the superficial velocity $\langle\boldsymbol{u}\rangle_{\mathrm{s}}$ and a Forchheimer term quadratic to $\langle\boldsymbol{u}\rangle_{\mathrm{s}}$. The permeability tensor $\boldsymbol{K}$ and the Forchheimer tensor $\boldsymbol{F}$ can both be solved in some boundary value problems, in a unit cell identical to the one as aforementioned. Whitaker (1996) stated that solving these boundary value problems is essentially identical to solving the Navier-Stokes equations for steady incompressible flows in a spatially periodic system, and any Navier-Stokes code can be applied to solve these boundary value problems.
Whitaker theoretically derived the Forchheimer equation by inserting the steady-state closure for the surface filter containing $\boldsymbol{K}$ and $\boldsymbol{F}$ back to equation (2.12). This procedure is mainly practical in homogeneous media. Up to this point, the famous procedure of the *volume-averaged Navier Stokes equations (VANS)* is restricted in steady-state problems only, as Whitaker (1996) simply neglected the time derivative term in the Navier-Stokes.

2.2 Steady porous media flow

Before we dig into unsteady porous media flow, the state of art in steady porous media flow will be discussed in this section. It is necessary to discuss it here because although the unsteady porous media flows are more complex than the steady flows, the theories behind them are similar to each other. In the next following sections, we mainly introduce the classical Darcy's law (Darcy, 1856), the Forchheimer equation (Forchheimer, 1901) and different regimes concerning the flow state.

2.2.1 The Darcy's law

In *steady* porous media flows, the space-averaged/macroscopic velocity is dependent on the pressure/hydraulic gradient which causes the motion. This dependency varies with the pore

Reynolds number which is defined as follows:

$$Re_{\text{pore}} = \frac{|\langle \boldsymbol{u} \rangle_{\text{s}}| d}{\nu} \tag{2.13}$$

where $|\langle \boldsymbol{u} \rangle_{\text{s}}|$ is the magnitude of the superficial/macroscopic velocity, d is the pore/grain size and ν is the kinematic viscosity. For very small pore Reynolds numbers ($Re_{\text{pore}} \ll 1$) viscous forces dominate the flow and the inertia effects (forces) may be neglected. It is well established in this case that the classical Darcy's law describes the proportional dependency of the averaged velocity on the pressure gradient:

$$\boldsymbol{\nabla} \langle p \rangle_{\text{i}} = a \cdot \langle \boldsymbol{u} \rangle_{\text{s}}, \tag{2.14}$$

where $\boldsymbol{\nabla} \langle p \rangle_{\text{i}}$ and $\langle \boldsymbol{u} \rangle_{\text{s}}$ represent the macroscopic pressure gradient and the macroscopic steady, superficial velocity. The proportionality constant a is dependent on the Darcy permeability K_D of the porous medium and the dynamic viscosity μ of the fluid as $a = -\mu / K_D$. Note that K_D is intrinsic to the geometry of the porous medium studied and it can be measured from experiments using Darcy's law. K_D is a scalar in 1-D flows. In three dimensional cases, K_D becomes a tensor.
Darcy's law implies that the driving force is entirely balanced by the resistive force. This relation was first discovered by Darcy (1856) on experimental basis. It gives a governing equation for one dimensional steady-state porous-media flow at very small pore Reynolds number. Yet it does not provide any formidable computational problem directly. Up-scaling methods on the computational basis, such as those by Whitaker (1986) and Sanchez-Palencia (1980), theoretically substantiated Darcy's law.

2.2.2 The Forchheimer equation and non-linear regimes

Strong inertia regime and the Forchheimer equation

The regime in which the Darcy's law is valid is referred to as the *linear regime*. The linear regime represents a state in which the pore Reynolds number is very small and the inertia effects are weak.
As velocities increase in magnitude, however, the inertial effects become stronger. When the pore Reynolds number becomes comparable to unity, the linear relation between pressure gradient and volume averaged velocity may not hold. Starting from the original publication of Forchheimer (1901), various formulations of a correction to the the linear relation (2.14) using polynomials have been proposed in literature, and they all have the same form:

$$\boldsymbol{\nabla} \langle p \rangle_{\text{i}} = a \langle \boldsymbol{u} \rangle_{\text{s}} + b \langle \boldsymbol{u} \rangle_{\text{s}}^{m}, \tag{2.15}$$

where b is a constant intrinsic to the porous medium and the density of the fluid, being a

negative value; and m is a constant.

In early studies, m is found to be a number close to 2 (Green and Duwez, 1951; Cornell and Katz, 1951), e.g., in the friction factor - Reynolds number plot in experiments concerning gas flow through consolidated porous rock samples (Cornell and Katz, 1951). Many researchers denote this regime as the *strong inertia regime*, in which the quadratic correction $b\langle \boldsymbol{u} \rangle_{\mathrm{s}}^2$ is applied in equation (2.15) to fully represent the force balance in the flow. Equation (2.15) with $m = 2$ is referred to as the *Forchheimer equation*, and the term $b\langle \boldsymbol{u} \rangle_{\mathrm{s}}^2$ is referred to as the *Forchheimer correction*.

Many other experimental results also supported this quadratic correction. In a series of experiments by Ergun (1952) to determine the friction factor of various materials in a packed bed fashion, this quadratic formulation can be observed. Dullien and Azzam (1973) measured the pressure drop with respect to the flow rate in capillary tubes in a wide range of the Reynolds number, and found that the Darcy's law is only valid up to $Re = 30 - 50$, and the data over that Reynolds number should then be described by the quadratic Forchheimer equation. MacDonald et al. (1979) used a large number of literature experimental data to test the Ergun equation (Ergun, 1952) and the Ahmed - Sunada equation (Ahmed and Sunada, 1969), which is a rearrangement of the Forchheimer equation (Forchheimer, 1901). The analysis proved that this quadratic term fitted all the data.

This quadratic correction is also supported on theoretical basis. By rigorous averaging of the Navier-Stokes equations over an averaging volume and solving a steady-state closure problem (Whitaker, 1996), the Darcy's permeability tensor and the Forchheimer correction tensor can be determined. This theory clearly indicates that the Forchheimer correction is quadratic for small values of the Reynolds number. Chen et al. (2001) applied the homogenization method to the steady-state Navier-Stokes equation and eventually derived this quadratic Forchheimer correction. Blick (1966) used the capillary-orifice model to predict high speed flow through porous media, which consisted of a bundle of capillary tubes with orifice plates spaced along the tubes; the distances between the orifice plates were equal to the mean tube diameter. In this mathematical model he derived the quadratic Forchheimer correction term, which compared well with his experimental data. Cvetkovic (1986) averaged the general form of the linear momentum balance of the Navier-Stokes equations and derived a macroscopic equation which has the same form as equation (2.15) plus a time derivative of the superficial velocity. In his macroscopic equation $m = 2$. Hassanizadeh and Gray (1987) adopted the continuum approach to derive a general macroscopic equation of fluid motion. In their theoretical derivations this quadratic correction is present. Ruth and Ma (1992) applied the averaging theorem to the microscopic momentum equation to obtain the macroscopic flow equation. They also studied some simple tube models of flow in porous media. However, Ruth and Ma (1992) did not suggest a quadratic correction. They stated that a polynomial of any order greater than one will apply. (Giorgi, 1997) used matched asymptotics to derive a Forchheimer law for a rigid porous medium, and obtained the Forchheimer law by series expansion for anisotropic materials. Their derivations also supported the quadratic Forchheimer correction.

This quadratic Forchheimer correction was not only concluded from experiments and theoretical derivations, but also from computational results. Coulaud et al. (1988) conducted pore scale simulations for 2-D cylinder arrays, with cylinders of either equal or non-equal diameters, arranged in a regular pattern. The Navier-Stokes equations are discretized by the mixed

finite-element method. Their results have fully supported the Forchheimer equation starting from the pore Reynolds number being over 1. Ma and Ruth (1993) solved the full Navier-Stokes equations describing flow through a diverging-converging unit cell by the vorticity-stream function method for a wide range of flow Reynolds numbers. Their numerical results have supported their theoretical derivations, which is considered as a further development of the quadratic Forchheimer equation. Papathanasiou et al. (2001) simulated flow through square and hexagonal arrays of uniform fibers, with the pore Reynolds number ranging from 0 to 160. The Navier-Stokes equations are solved on the pore scale using Finite Element Methods. Their results have shown that when $Re_{\text{pore}} < 1$, the quadratic Forchheimer equation describes the computational results very well. At high pore Reynolds number they have used a modified form of the Forchheimer equation, with the Forchheimer term expressed as a function of porosity, to better fit the simulation results. Fourar et al. (2004) presented simulation results of flows at high velocities through periodic 2-D staggered cylinder arrays and 3-D hexagonal close packed spheres at various Reynolds numbers. They have observed the quadratic correction at high Reynolds numbers and concluded that the non-linear 3D porous-media flow can be correctly modeled by the Forchheimer's equation. Mazaheri et al. (2005) solved the Navier-Stokes equations on the pore scale in flow through a network model of a porous medium, in which a network of cylindrical pores and parallelepiped connecting throats was constructed. Their simulation results were compared with experimental results using micro-particle imaging velocimetry (PIV) measurements and matched well. Their results have indicated that when the pore Reynolds number is large, the quadratic correction must be applied to model macroscopic flow behaviours.

Weak inertia regime and turbulence regime

Since the 1990s, starting from the numerical results of Barrère (1990), new careful work have supported researchers to question the quadratic correction to the Darcy's law over the entire Reynolds number range. At the onset of the deviation from the Darcy's law, observations have shown that m is not necessarily 2 in equation (2.15).

This can be found in literature concerning theoretical derivations, mostly using the homogenization method. Mei and Auriault (1991) used the theory of homogenization to examine the non-linear effects due to weak convective inertia of the fluid inside the porous medium. They have found that when the fluid inertia is small but finite, the correction term for isotropic and homogeneous media is cubic in the macroscopic mean velocity. They also did a study in the case of anisotropic 1D model of parallel corrugated tubes, and the correction term is also cubic in this case. Skjetne and Auriault (1999) used multiple scale homogenization technique and analysis of fluid mechanical effects to model non-linear effects in porous-media flows. They derived the general momentum and energy dissipation theorems for flow in periodic media. They have found that when the pore Reynolds number is in the order of $\boldsymbol{O}(\delta^{-1})$, where $\delta = l/L$ denotes the ratio between the microscopic length l and the macroscopic length L, the pressure gradient is proportional to the power of 3/2 in the macroscopic mean velocity. For turbulence, however, a quadratic Forchheimer correction term should be applied. Balhoff et al. (2010) also used the homogenization to model non-linear effects in porous-media flows on a macroscopic level, and ran numerical simulations that solved the full Navier-Stokes equations in a periodic sinusoidal geometry (constricted tube). Both their derivations and simulation results have supported that for isotropic media,

particularly at $Re_{\text{pore}} < 1$, the correction term is cubic in macroscopic mean velocity rather than quadratic.

On the computational basis, many numerical results have also supported this discovery. Firdaouss et al. (1997) performed numerical simulations on 2D periodic porous media with different geometry configurations, including anisotropic staggered cylinder arrays with and without central symmetry, periodic sawtooth model and a periodic irregular geometry. All these simulations have demonstrated that for small Reynolds numbers, the nonlinear correction to Darcy's law is cubic with respect to the superficial velocity. They also reinterpreted some well-known filtration experiments by Darcy (1856), Hazen (1895) and Chauveteau (1965), and conducted a mathematical proof to support this claim. Koch and Ladd (1997) applied Numerical simulations using a lattice-Boltzmann formulation to investigate flow through periodic and random arrays of aligned cylinders. They have found that when $Re_{\text{pore}} \ll 1$, the correction to Darcy's law is cubic with respect to the superficial velocity. Souto and Moyne (1997) used the finite volume method to solve the Navier-Stokes equations in 2D spatially periodic porous mediums consisting of rectangulars. They investigated ordered medium such as in-line or staggered square cylinders, zigzag medium, and disordered medium such as randomly distributed square cylinders. They have found that, for isotropic media, when $1 < Re_{\text{pore}} < 20$, the correction term for moderate Reynolds number is cubic in superficial velocity. Rojas and Koplik (1998) conducted numerical computations based on a spectral element method to investigate flow through an array of cuboids of square cross section. They have found that the correction term to Darcy's law is cubic at low Reynolds numbers, and quadratic when the Reynolds number is comparable to unity. Skjetne et al. (1999) numerically solved the Navier-Stokes equations for flow in a self-affine channel with a constant perpendicular opening (twisted channel), and verified the existence of a so-called *weak inertia regime*, where the cubic correction term to the Darcy's law is valid. Jacono et al. (2005) ran 3D direct numerical simulations to complement the analysis of the "Oseen-Poiseuille" equations, which are developed from an asymptotic formulation of the Navier-Stokes equations to study the influence of weak inertia. Their simulation results also supported the existence of the weak inertia regime, where the cubic correction is present.

This cubic correction turns out to be more accurate than the quadratic one in the so-called *weak inertia regime*, which is activated when the pore Reynolds number is in the range of $[\delta^{1/2}, 1]$, where δ represents the ratio between the microscopic and the macroscopic length scales (Lasseux et al., 2011). However, when the Reynolds number increases beyond the upper limit, the flow then enters the *strong inertia regime*, with the pore Reynolds number typically ranging from about one to ten. In this regime, the Forchheimer correction is valid, i.e., a correction to the classical Darcy's law with quadratic dependency on the velocity can be applied.

The recent computational results of Lasseux et al. (2011) using upscaling method has shown that for ordered and disordered structure of porous media, the behavior of theses regimes can be very different. In disordered structures, the Reynolds number interval corresponding to weak inertia, that is always present, is strongly reduced in comparison to ordered structures. This explains the reason why in most of the previous experimental results the weak inertia regime is not observed.

Above the *strong inertia regime*, the flow can eventually enter the *turbulence regime*, when

the pore Reynolds number is in the order of 100. This has been observed in experiments and numerical simulations (Dybbs and Edwards; Ghaddar, 1995; Koch and Ladd, 1997).
In summary, the non-linear deviation from Darcy's law can be classified into three different regimes: (a) the *weak inertia regime* with the pore Reynolds number ranging within $[\delta^{1/2}, 1]$, where the non-linear correction is taken as a cubic function of the superficial velocity; (b) the *strong inertia regime* with the pore Reynolds ranging in [1, 10], where the velocity correction to the classical Darcy's law is taken as a quadratic function, and the Forchheimer equation is valid; and (c) the *turbulence regime* with a pore Reynolds number greater than approximately 100.

2.2.3 Onset of the non-linear effects in steady porous media flow

In early studies, the presence of the non-linear effects in porous-media flows has been attributed to the occurance of turbulence (e.g. Tek et al., 1962), as in some specific flows such as rough pipe flow, it is well known that in turbulence the driving force is quadratic to the flow rate Cvetkovic (1986). It was discovered in later studies that much before the onset of turbulence, the non-linear effects already set in (e.g. Scheidegger, 1960; Bear, 1972; Dybbs and Edwards). Some researchers (e.g. Bear, 1972; MacDonald et al., 1979; Cvetkovic, 1986) believed that it is the microscopic inertial forces that give rise to the non-linear effects; while some others believed that it is the increased microscopic drag forces that caused the non-linear effects, e.g., in the theoretical derivation of Hassanizadeh and Gray (1987), based on order-of-magnitude analysis, they argued that when $Re_{\text{pore}} \approx 10$, at the onset of non-linear effects, macroscopic viscous and inertial forces are much smaller than microscopic viscous forces, and the non-linear effects are then caused by the growth of microscopic viscous forces. In the study of Ruth and Ma (1992), they demonstrated that the microscopic inertial term does not cause the non-linear effects. It is the changes in the values of the surface integral terms, which result from microscopic inertial effects distorting the velocity and pressure fields, that leads to the non-linear effects. Hence the non-linear effects must be modelled in the surface integral terms resulting from the averaging procedure, not by the averaged microscopic inertial terms. This is in consistency with the derivations of Whitaker (1996).
Despite of different arguments explaining the reason that caused the non-linear effects in porous-media flows, the pore Reynolds number is widely accepted as the dominant variable that determines the onset of the non-linear effects in steady flows (e.g. Dullien and Azzam, 1973; Whitaker, 1996; Blick, 1966; Hassanizadeh and Gray, 1987; Coulaud et al., 1988; Papathanasiou et al., 2001; Fourar et al., 2004; Mazaheri et al., 2005; Mei and Auriault, 1991; Firdaouss et al., 1997; Koch and Ladd, 1997; Souto and Moyne, 1997; Rojas and Koplik, 1998; Jacono et al., 2005; Lasseux et al., 2011). One example is that in the order-of-magnitude analysis of Whitaker (1996), the Forchheimer tensor $\boldsymbol{F}$, which is used to define the quadratic correction term, is related to $\boldsymbol{O}(Re_{\text{pore}})$, which is the oder of the magnitude

of Re_{pore} by

$$\boldsymbol{F} = \left\{ \boldsymbol{O}(Re_{\text{pore}}) + \boldsymbol{O}\left(\frac{(\delta/d) Re_{\text{pore}}^2}{1 + \boldsymbol{O}[(\delta/d) Re_{\text{pore}}]} \right) \right\}, \tag{2.16}$$

where δ is the boundary-layer thickness and d is the pore scale. A further derivation gives:

$$\begin{cases} \boldsymbol{F} = \boldsymbol{O}(Re_{pore}), & Re \ll 1, \\ \boldsymbol{F} = \boldsymbol{O}(Re_{pore}) + \boldsymbol{O}(Re_{pore}), & Re \gg 1 \end{cases} \tag{2.17}$$

This indicates that when $\boldsymbol{O}(Re_{\text{pore}})$ is very small, $\boldsymbol{F}$ can be neglected; when $\boldsymbol{O}(Re_{\text{pore}})$ gets larger, $\boldsymbol{F}$ is large. It means that the onset of the non-linear (Forchheimer) behaviours in steady porous-media flows is highly dependent on the pore Reynolds number.
While most of the researchers took the pore Reynolds number as reference, there were exceptions as a minority. In the theoretical derivation of the Forchheimer equation by applying the averaging theorem to the microscopic momentum equation, Ruth and Ma (1992) examined simple tube models of flow in porous media. In these models, flow in straight and bend tubes are investigated. They argued that a Forchheimer number based on macroscopic scales defined as

$$F_0 = \frac{-bK_D |\langle \boldsymbol{u} \rangle_{\text{s}}|}{\mu} \tag{2.18}$$

should be used rather than the pore Reynolds number to examine the onset of the non-linear effects in steady-state porous-media flows. Here b is from equation (2.15) and K_D is the Darcy permeability.
They argued that because the macroscopic inertial effects do not necessarily scale with the micro scale, such as the pore size, and because the microscopic inertial effects do not directly lead to macroscopic inertial effects, it is not proper to predict the macroscopic non-linear effects by the microscopic pore Reynolds number.
We recall the Forchheimer equation (2.15) in the strong inertia regime and reformulate it in the following

$$-\boldsymbol{\nabla} \langle p \rangle_{\text{i}} = \frac{\mu}{K_D} \langle \boldsymbol{u} \rangle_{\text{s}} - b \langle \boldsymbol{u} \rangle_{\text{s}}^2, \tag{2.19}$$

Ruth and Ma (1992) suggested that the constant Darcy permeability K_D can be replaced by a dynamic permeability K and equation (2.19) becomes

$$\boldsymbol{\nabla} \langle p \rangle_{\text{i}} = \frac{\mu}{K} \langle \boldsymbol{u} \rangle_{\text{s}}, \tag{2.20}$$

where

$$\frac{1}{K} = \frac{1}{K_D}\left(1 + \frac{-bK_D|\langle \boldsymbol{u} \rangle_{\mathrm{s}}|}{\mu}\right) \tag{2.21}$$

Ruth and Ma (1992) argued that when the Forchheimer number $F_0 = \frac{-bK_D|\langle \boldsymbol{u} \rangle_{\mathrm{s}}|}{\mu}$ becomes comparable to unity, it indicates when the microscopic inertial effects lead to the macroscopic inertial effects, and this number can be used to determine the onset of the non-linear effects.

2.3 Unsteady porous media flow

Note that in all of the aforementioned regimes, the discussions considering the velocity and the pressure gradient are constraint to a *steady-state* of the macro-scale velocity. If there are unsteady boundary conditions or an unsteady pressure gradient, the macroscopic flow becomes unsteady and – unless the variations are very slow – equations (2.14) or (2.15) can not be applied in this form.

2.3.1 Unsteady Darcy and unsteady Forchheimer equations

For unsteady porous media flow, a number of studies have shown that a phase shift between pressure drop and superficial velocity can exist. It results from the inertia of the accelerated fluid, and must be represented by an unsteady term. Laushey and Popat (1968) conducted experiments in a closed circular tube filled with sand, which was always maintained fully of water, to simulate a confined aquifer. They measured the piezometric head in the sand to represent the pressure gradient. They investigated both steady and unsteady flows. For steady flows, they have verified Darcy's law, while for unsteady flows, they suggested that corrections in terms of the time derivatives of the pressure gradient must be added in Darcy's law. Burcharth and Andersen (1995) used a cylinder analogy to theoretically investigate one-dimensional unsteady porous-media flow equations. They stated that for unsteady porous-media flow, macroscopic convective accelerations, which shall be represented by a time derivative of the superficial velocity, are present in addition to the local acceleration. Hall et al. (1995) conducted experiments in an oscillatory water tunnel to investigate how temporal inertia affects the resistance of flow in porous media. The flows were driven with low frequencies, and both uniformly packed spheres of equal diameter and randomly placed stone were investigated. They not only used the time derivative of the superficial velocity as a correction term to the Forchheimer equation to represent the phase shift between pressure drop and superficial velocity, but also measured the coefficients in the terms. Gu and Wang (1991) investigated water wave interactions with porous sea beds by means of theoretical derivation and numerical computation. They explicitly noted that Darcy's law cannot be applied in such problems. In their model for the flows inside porous media, they also considered this time derivative term.

The resulting equation can be written as

$$\boldsymbol{\nabla}\langle p\rangle_{\mathrm{i}} = a\langle \boldsymbol{u}\rangle_{\mathrm{s}} + b\langle \boldsymbol{u}\rangle_{\mathrm{s}}^{m} + c\frac{\partial\langle \boldsymbol{u}\rangle_{\mathrm{s}}}{\partial t}, \tag{2.22}$$

where the coefficients a, b and c represent the linear and quadratic parts of the interaction force and the inertia term due to flow acceleration. If $b = 0$, the expression reduces to what is called *unsteady Darcy equation*. If $a \neq 0$, $b \neq 0$, $c \neq 0$ and $m = 2$, the expression is called *unsteady Forchheimer equation*.

Attempts have been made to determine the coefficients a, b, and c from experiments. In the cylinder analogy of Burcharth and Andersen (1995), which was used to investigate equation (2.22), it was stated that a, b and c are not constants and shall be treated as instantaneous values. However, in engineering practice, the coefficients are simply taken as constants dependent on characteristic Reynolds and Keulegan-Carpenter (KC) numbers, $KC = V_m T/d$, where V_m is the maximum velocity in oscillatory flows, T is the oscillating period and d is the particle diameter. In the experiment of Hall et al. (1995) in an oscillatory water tunnel driven with low frequencies, a, b and c were measured and compared to the coefficients in steady-state cases, a_s, b_s and c_s. They claimed that c does seem to be a constant for a given medium and independent of the acceleration. They also claimed that a_s, measured from steady-state cases, differ from a, which is generally for oscillatory cases. Other researchers such as Gu and Wang (1991) and Lowe et al. (2005) used the so-called *virtual mass* term to investigate these coefficients in problems such as water wave interactions with sea beds and oscillatory flow inside benthic organisms.

However, a full agreement between experimental results and behavior predicted by equation (2.22) with fitted coefficients has not yet been achieved. Experimental results even suggest that the coefficients in equation (2.22) can not be taken as constant during oscillatory flow. Moreover, it seems that a generally accepted theoretical framework of how to find the coefficients in equation (2.22) does not exist.

2.3.2 Deriving the coefficients from VANS approach

One way to derive equation (2.22) is by using the *Volume-Averaged Navier-Stokes (VANS)*. By volume-averaging the momentum equation over a representative control volume, Whitaker (1996) derived a superficial averaged form of the Navier-Stokes equations (2.12). He also derived a steady-state closure for the interaction term based on assumptions such as the length constraint (2.9) and order-of-magnitude analysis. Inserting this steady-state closure back into the averaged momentum equation (2.12) and neglecting several terms, one could get an equation in the same form as the unsteady Forchheimer equation (2.22). Under the condition of unidirectional flow through isotropic, homogeneous material and low Reynolds number, this equation can be written with a structure identical to that of the unsteady Darcy equation, and the general mathematical expression of the time scale $\tau = c/a$ can be explicitly obtained.

This approach has been adopted by several authors because it offers a mathematically sound framework for applications, in which strong changes in material properties such as porosity

and permeability are present. Breugem et al. (2006) investigated turbulent flow in a channel, which has a solid top wall and a permeable bottom wall. In the channel region, they performed DNS, while in the homogeneous porous region, they directly applied the VANS approach and the steady-state closure from Whitaker (1996), with the permeability and Forchheimer tensors determined from the modified Ergun equation (Bird et al., 2002). Hill and Straughan (2008) studied instabilities in Poiseuille flow over a porous layer. In his study, a Newtonian fluid overlies a Brinkmann transition layer, which in turn overlies a porous layer. The governing equations in the Brinkmann layer and the porous layer are the Brinkmann equation and the unsteady Darcy equation, respectively, with the time constants derived from the VANS approach. In the stability analysis of a channel flow bounded by two porous regions by (Tilton and Cortelezzi, 2008), the channel region was modelled by the Navier-Stokes equations, while the porous regions were modelled by the Volume-Averaged Navier-Stokes equations. In analysis of bioheat transport, (Fan and Wang, 2011) applied the volume-averaging procedure to the Navier-Stokes equations and an energy conservation equation concerning temperature in the blood phase. They suggested to directly use the steady-state closure from Whitaker (1996) to close the averaged momentum equations, while the problem there is unsteady blood flow.
A similar formulation was used by Kuznetsov and Nield (2006), Wang (2008) and Habibi et al. (2011) to directly derive an analytical solution for unsteady flow in a porous channel. It has to be noted, however, that the VANS approach does not offer a theoretical approach how to model the aforementioned coefficients for the unsteady term and the interaction force.

2.3.3 Deriving the coefficients from the virtual mass approach

Another way to derive an unsteady Darcy equation in the form of (2.22) was presented by Rajagopal (2007) within the context of mixture theory. He also discussed possible implications of the unsteadiness of the flow field, suggesting consideration of a *virtual mass* term if inertial nonlinearities cannot be neglected. This term was proposed by Sollitt and Cross (1972) to account for the inhomogeneity of the flow field surrounding individual structures in the porous material during transient flow.
This approach was also adopted by many authors. In the cylinder analogy of Burcharth and Andersen (1995), they theoretically derived the coefficients a, b and c in equation (2.22), using associated virtual mass coefficients. Right after it, they then presented some existing experimental data (Hannoura and McCorquodale, 1978; Smith, 1991; Andersen et al., 1993) to support their derivations. Gu and Wang (1991) directly applied the virtual mass concept in their model for flows inside porous media, when investigating water wave interactions with porous sea beds. They stated that a, b and c are all constants; a is related to Darcy's law; b is frequency-dependent for oscillatory flow; and c is only dependent on K_D, ν, ϵ and a virtual mass coefficient which should be determined from experiments for different medium. (Lowe et al., 2005) presented a theoretical model to estimate oscillatory flow inside benthic organisms which are described as submerged canopies. In their model, they applied the virtual mass approach, and replaced the pressure gradient by a time derivative of the free stream velocity above the porous media - free flow interaction face. Their model essentially has the

same form as equation (2.22), with $m = 2$ and c determined by the virtual mass approach. Note that this approach results in a larger time scale in unsteady porous media flow, compared to the VANS approach with the steady-state closure.
To the author's best knowledge, a systematic comparison and assessment of the different formulations of the unsteady Darcy equation has not been done so far.

3 Problem Statement

The rest of this PhD thesis mainly consists of three parts, and each part answers several questions concerning *unsteady*, *linear* and *non-linear* flows. In each part, theoretical derivations and results of Direct Numerical Simulations for verification will be presented.
The first part mainly answers the following questions:

- For *unsteady* and *linear* flows, is the unsteady Darcy equation (1.3) together with constant coefficients accurate, and can it be used to describe these flows on the macroscopic scale?
- Is there a general mathematical expression for the coefficient c in unsteady Darcy equation (1.3)? If yes, what is it?

In this part, the time scale $\tau = \frac{c}{a}$ in the unsteady Darcy equation (1.3) is investigated. First, the unsteady Darcy equation in the form of equation (1.3) will be derived using the VANS and the virtual mass approaches, respectively. Then an alternative derivation of the unsteady Darcy equation (1.3) by volume-averaging the equation of the kinetic energy will be proposed. The mathematical expressions of the time scales $\tau = \frac{c}{a}$ resulting from these three methods are completely different. The time scales from the virtual mass and the energy approaches is larger than the time scale from the VANS approach. Finally, fully resolved *direct numerical simulation (DNS)* of the flow in the pore space will be used to verify the expressions of these time scales. By keeping the Reynolds number small, the flow remains linear, and the non-linear Forchheimer term can be neglected. The time scales obtained from the simulation results are compared to those obtained by the VANS, the *virtual mass* and our new kinetic energy approaches. The investigation of the time scales also verifies the applicability of the unsteady Darcy equation (1.3).

The second part mainly answers the following questions:

- For *oscillatory* and *linear* flows, is the unsteady Darcy equation (1.3) together with constant coefficients applicable and accurate, in all frequency ranges?
- Are the time scales derived from the aforementioned methods accurate in all frequency ranges?

In this part, first, an analytical solution of the unsteady Darcy equation (1.3) is derived. Then the analytical solutions of (Womersley, 1955) and (Loudon and Tordesillas, 1998) for oscillatory pipe and channel flows are analyzed to compare with the analytical solutions of the unsteady Darcy equation (1.3) with different time scales derived from the aforementioned methods. Finally, fully resolved *direct numerical simulation (DNS)* of the flow in the pore space will be used to verify the applicability of the unsteady Darcy equation (1.3) with these time scales. The pressure gradient is prescribed by sinusoidal functions with respect to time in order to get oscillatory flow.

The third part mainly answers the following questions:

- For *unsteady* flows, which physical variable determines the onset of the non-linear effects?
- For *unsteady* and *non-linear* flows, is the unsteady Forchheimer equation (1.4) together with constant coefficients accurate, and can it be used to describe these flows on the macroscopic scale?

In this part, we set up a series of direct numerical simulations in different simulation cases with different geometries. We look for which physical variable determines the onset of the non-linear effects. Moreover, equation (1.4) is solved in Matlab numerically with different options of the time scale $\tau = \frac{c}{a}$. The numerical solutions from Matlab are compared with DNS results to investigate the applicability of the unsteady Forchheimer equation (1.4) and the suitability of the time scale for unsteady flow in the non-linear regime.

4 Part1: Unsteady Darcy Equation for Unsteady and Linear Flows

Note: most of this part is taken from Zhu et al. (2014).
In this part, we focus on *unsteady* and *linear* porous-media flows. We investigate whether the unsteady Darcy equation (1.3) with constant coefficients a and c is accurate in describing unsteady and linear flows. We assume the value of the coefficient a remains the same as that in the Darcy's law (1.1), and later verify it via *Direct Numerical Simulations (DNS)*. For the coefficient c (or the time scale $\tau = c/a$), we derive it with different methods. First, we summarize the resulting forms of the unsteady Darcy equation from the VANS and the virtual mass approaches (section 4.1). Then, we propose an alternative expression for the time scale in unsteady porous media flow by volume-averaging the equation of the kinetic energy (section 4.1.4). Finally, we use fully resolved *direct numerical simulation (DNS)* of the flow in the pore space to verify this expression (section 4.2). By keeping the Reynolds number small, the flow remains linear, and the non-linear Forchheimer term can be neglected. The time scales obtained from the simulation results are compared to those obtained by the VANS, the *virtual mass* and our new kinetic energy approaches.

4.1 Theory

4.1.1 Steady and unsteady form of the Darcy equation

Using the notations from volume-averaging (Whitaker, 1996), we recall the Darcy's law here, writting it as the proportional relation between the *superficial velocity* $\langle \boldsymbol{u} \rangle_{\mathrm{s}}$ and the applied *intrinsic pressure gradient* $\boldsymbol{\nabla} \langle p \rangle_{\mathrm{i}}$. In vectorial form, this relation reads as

$$\langle \boldsymbol{u} \rangle_{\mathrm{s}} = -\frac{K_D}{\mu} \boldsymbol{\nabla} \langle p \rangle_{\mathrm{i}}, \tag{4.1}$$

where K_D denotes *Darcy's permeability*, which can be experimentally determined by applying a constant pressure gradient and measuring the flow rate $Q = A_Q \cdot \langle \boldsymbol{u} \rangle_{\mathrm{s}}$ through a given cross-sectional area A_Q. Therefore, K_D is commonly identified as the permeability obtained under steady flow conditions. K_D needs to be formulated as a tensor in the general case. However, we restrict ourselves here to uniform flow in a homogeneous, isotropic material and, hence, use a scalar permeability K_D.
When investigating unsteady porous-media flow at low Reynolds numbers, the situation is less clear. In the general unsteady case, the permeability, if defined as above, is not

necessarily constant over time. A common model for this type of flow is given in the form of the unsteady Darcy equation

$$\tau \partial_t \langle \boldsymbol{u} \rangle_{\mathrm{s}} + \langle \boldsymbol{u} \rangle_{\mathrm{s}} = -\frac{K}{\mu} \boldsymbol{\nabla} \langle p \rangle_{\mathrm{i}}, \tag{4.2}$$

where τ represents a time-scale and K a permeability (e.g. Burcharth and Andersen, 1995; Kuznetsov and Nield, 2006; Rajagopal, 2007; Sollitt and Cross, 1972).
The aim of this part is to assess the validity of the unsteady Darcy equation (4.2) with constant coefficients. This can be transformed into the question of whether the permeability and the time constant can be treated as time-independent in the general unsteady case. Furthermore, we address the question of how these values can be determined. To achieve this aim, we first discuss two well-known approaches for deriving the unsteady Darcy equation, which are based on the volume-averaging of the Navier-Stokes equations (2.1). In section 4.1.4, we shall derive and discuss an alternative way based on the volume-averaging of the kinetic energy equation. In our discussion, we consider that we have a control volume V with periodic boundary conditions on ∂V. This assumption is reasonable for homogeneous porous media in regions far from the boundaries, where the control volume V ideally repeats itself. Furthermore, we restrict ourselves to unidirectional flow through this representative elementary volume (REV). Finally, we assume a small Reynolds number and uniform macroscopic flow.

4.1.2 Volume-averaging of the momentum equation

Whitaker (1996) developed the following formulation by volume-averaging the Navier-Stokes equation (2.1):

$$\begin{aligned} &\rho \partial_t \langle \boldsymbol{u} \rangle_{\mathrm{i}} + \rho \langle \boldsymbol{u} \rangle_{\mathrm{i}} \operatorname{div} \langle \boldsymbol{u} \rangle_{\mathrm{i}} + \underbrace{\rho \epsilon^{-1} \operatorname{div} \langle \tilde{\boldsymbol{u}} \tilde{\boldsymbol{u}} \rangle_{\mathrm{s}}}_{\text{volume filter}} \\ &\quad = -\boldsymbol{\nabla} \langle p \rangle_{\mathrm{i}} + \underbrace{\mu \boldsymbol{\nabla}^2 \langle \boldsymbol{u} \rangle_{\mathrm{i}}}_{\text{Brinkman correction}} + \underbrace{\frac{1}{|V_\beta|} \int_{A_{\beta\sigma}} \boldsymbol{n}_{\beta\sigma} \cdot (-\tilde{p} \boldsymbol{I} + \mu \boldsymbol{\nabla} \tilde{\boldsymbol{u}}) \; dA}_{\text{surface filter}} . \end{aligned} \tag{4.3}$$

The surface filter represents the drag due to surface forces at the fluid-solid interface. It is identical to what Rajagopal (2007) referred to as an *interaction term*.
For a homogeneous and periodic REV, the second and third terms on the left-hand side vanish, as does the Brinkman correction. The equation then reduces to

$$\rho \partial_t \langle \boldsymbol{u} \rangle_{\mathrm{i}} = -\boldsymbol{\nabla} \langle p \rangle_{\mathrm{i}} + \underbrace{\frac{1}{|V_\beta|} \int_{A_{\beta\sigma}} \boldsymbol{n}_{\beta\sigma} \cdot (-\tilde{p} \boldsymbol{I} + \mu \boldsymbol{\nabla} \tilde{\boldsymbol{u}}) \; dA}_{\text{surface filter}} . \tag{4.4}$$

In the steady state, the surface filter can be replaced by the Forchheimer approximation

$$\frac{1}{|V_\beta|}\int_{A_{\beta\sigma}} \boldsymbol{n}_{\beta\sigma}\cdot\left(-\tilde{p}\boldsymbol{I}+\mu\boldsymbol{\nabla}\tilde{\boldsymbol{u}}\right)\,dA = -\frac{\mu}{K_D}(1+F|\langle\boldsymbol{u}\rangle_{\mathrm{i}}|)\langle\boldsymbol{u}\rangle_{\mathrm{s}}, \tag{4.5}$$

cf. Whitaker (1996). Additionally, if the Reynolds number is sufficiently small, the term $F|\langle\boldsymbol{u}\rangle_{\mathrm{i}}|$ vanishes and the steady Darcy equation (4.1) is obtained.
For unsteady flow it has been proposed by several authors to use closure (4.5) with constant coefficients for the interaction term although its possible time dependence has been discussed (Rajagopal, 2007). Inserted in equation (4.4) we arrive at the following expression:

$$\frac{K_{\mathrm{D}}}{\nu\epsilon}\partial_t\langle\boldsymbol{u}\rangle_{\mathrm{s}} + \langle\boldsymbol{u}\rangle_{\mathrm{s}} = -\frac{K_{\mathrm{D}}}{\mu}\boldsymbol{\nabla}\langle p\rangle_{\mathrm{i}}, \tag{4.6}$$

where $\mu=\rho\nu$. By comparing it with the unsteady Darcy equation (4.2), we can identify the time constant obtained by this approach as

$$\tau_{\mathrm{vans}} = \frac{K_{\mathrm{D}}}{\nu\epsilon}. \tag{4.7}$$

The above form of the unsteady Darcy equation relies on the assumption that the steady-state approximation (4.5) can be used in the unsteady case (here denoted as VANS with steady-state closure). The time dependence of the interaction term and its closure (4.5) is being examined in the following sections of this part. The next section describes a method that is intended to take this time dependence into account, the virtual mass approach. In addition, we shall demonstrate by DNS in section 4.2.5, that the steady-state closure can not be used in the considered unsteady flow situations.

4.1.3 Virtual mass approach

It has been emphasized in the literature (e.g., Laushey and Popat, 1968; Burcharth and Andersen, 1995; Hall et al., 1995; Gu and Wang, 1991) that, due to inertial effects, the time constant in equation (4.2) needs special attention. Using the analogy to unsteady flow around a single obstacle, a *virtual mass* coefficient was introduced by, e.g., Sollitt and Cross (1972) to compensate for the volume of fluid to be accelerated in the vicinity of the obstacle. To take these effects into account, a virtual mass force per unit volume can be added to the closure of the interaction term in equation (4.5). For small Reynolds numbers – neglecting the Forchheimer term – this results in

$$\frac{1}{|V_\beta|}\int_{A_{\beta\sigma}} \boldsymbol{n}_{\beta\sigma}\cdot\left(-\tilde{p}\boldsymbol{I}+\mu\boldsymbol{\nabla}\tilde{\boldsymbol{u}}\right)\,dA = -\frac{\mu}{K_D}\langle\boldsymbol{u}\rangle_{\mathrm{s}} - \rho\, C_{\mathrm{vm}}\frac{1-\epsilon}{\epsilon}\partial_t\langle\boldsymbol{u}\rangle_{\mathrm{i}}. \tag{4.8}$$

Here, C_{vm} is the virtual mass coefficient, yet to be determined. In this way, we obtain

$$\frac{K_D}{\nu\epsilon}\left[1+C_{\mathrm{vm}}\frac{1-\epsilon}{\epsilon}\right]\partial_t\langle\boldsymbol{u}\rangle_{\mathrm{s}} + \langle\boldsymbol{u}\rangle_{\mathrm{s}} = -\frac{K_D}{\mu}\boldsymbol{\nabla}\langle p\rangle_{\mathrm{i}}. \tag{4.9}$$

Thus, the time constant derived by this approach is given by:

$$\tau_{\mathrm{vm}} = \frac{K_D}{\nu\epsilon}\left[1 + C_{\mathrm{vm}}\frac{1-\epsilon}{\epsilon}\right], \tag{4.10}$$

where C_{vm} is an empirical coefficient. Lowe et al. (2008) determined C_{vm} by fitting measured data for the phase and amplitude of the flow in a canopy (porous media) with the model equation. They also compared estimates for C_{vm} from the literature, which are in the range of $0.5 \leq C_{\mathrm{vm}} \leq 2.0$.
One interpretation of the constant C_{vm} is that it models flow inhomogeneities on the pore scale. Hence, the success of the virtual mass approach relies on the knowledge of C_{vm} for a certain flow situation, which needs to be determined in experiments. In section 4.2.8, we numerically investigate the influence of the choice of C_{vm} and compare the results for different values of C_{vm} with DNS.

4.1.4 A new approach to determine the time constant in unsteady porous-media flow

To understand the nature of the virtual mass term, we now derive an alternative possibility to define a time constant for the unsteady Darcy model (4.2), which is based on the conservation of kinetic energy. The resulting form of the unsteady Darcy equation is in agreement with the virtual mass approach in the sense that we correct the time constant by a factor greater than one, which depends only on the pore-structure and the microscale-velocity. In our derivation, we need to make a number of assumptions and approximations, which we support by our DNS from section 4.2.

Volume-averaging of the energy equation

We start deriving an equation of the form of equation (4.2) by the use of the kinetic energy equation. Keeping in mind that $\partial_t(\boldsymbol{u}\cdot\boldsymbol{u}) = 2\boldsymbol{u}\cdot\partial_t\boldsymbol{u}$, we can multiply the momentum part of the incompressible Navier-Stokes equations (2.1) by the velocity $\boldsymbol{u}$ to obtain an equation for the kinetic energy of the flow (without a gravity term):

$$\frac{\rho}{2}\partial_t(\boldsymbol{u}\cdot\boldsymbol{u}) + \rho\boldsymbol{u}\cdot(\boldsymbol{u}\cdot\boldsymbol{\nabla}\boldsymbol{u}) - \mu\boldsymbol{u}\cdot\boldsymbol{\nabla}^2\boldsymbol{u} = -\boldsymbol{u}\cdot\boldsymbol{\nabla}p. \tag{4.11}$$

Volume-averaging the equation now yields

$$\frac{\rho}{2}\partial_t\langle\boldsymbol{u}\cdot\boldsymbol{u}\rangle_{\mathrm{s}} + \rho\langle\boldsymbol{u}\cdot(\boldsymbol{u}\cdot\boldsymbol{\nabla}\boldsymbol{u})\rangle_{\mathrm{s}} - \mu\big\langle\boldsymbol{u}\cdot\boldsymbol{\nabla}^2\boldsymbol{u}\big\rangle_{\mathrm{s}} = -\langle\boldsymbol{u}\cdot\boldsymbol{\nabla}p\rangle_{\mathrm{s}}, \tag{4.12}$$

which can be regarded as the energy equation analogon to equation (4.3). Let us again consider an REV with periodic boundary conditions on ∂V in uniform flow conditions. We will first demonstrate that the second term on the left-hand side (advective term) vanishes and then reformulate the other terms. After applying the Gauß theorem to the advective

term, we find that

$$\langle \boldsymbol{u} \cdot (\boldsymbol{u} \cdot \boldsymbol{\nabla} \boldsymbol{u}) \rangle_{\mathrm{s}} = \frac{1}{2|V|} \int_{\partial V} \boldsymbol{u} \cdot \boldsymbol{n} |\boldsymbol{u}|^2 \, ds - \frac{1}{2} \big\langle \mathrm{div}(\boldsymbol{u}) |\boldsymbol{u}|^2 \big\rangle_{\mathrm{s}}. \tag{4.13}$$

The surface integral vanishes under periodic boundary conditions, and, due to incompressibility, we have $\mathrm{div}(\boldsymbol{u}) = 0$. Hence, the advective term does *not* contribute to the kinetic energy balance.

Let us proceed by considering the term $\langle \boldsymbol{u} \cdot \boldsymbol{\nabla} p \rangle_{\mathrm{s}}$. We can decompose $p = \langle p \rangle_{\mathrm{i}} + \tilde{p}$ into a mean part $\langle p \rangle_{\mathrm{i}}$ and a fluctuation $\tilde{p}$. Here, $\langle p \rangle_{\mathrm{i}}$ is the averaged pressure over the fluid phase of the averaging volume, and $\boldsymbol{\nabla} \langle p \rangle_{\mathrm{i}}$ is the pressure gradient driving the flow. In our case, the pressure gradient is taken as constant over the whole averaging volume, so we get

$$\langle \boldsymbol{u} \cdot \boldsymbol{\nabla} p \rangle_{\mathrm{s}} = \langle \boldsymbol{u} \cdot \boldsymbol{\nabla} \langle p \rangle_{\mathrm{i}} \rangle_{\mathrm{s}} + \langle \boldsymbol{u} \cdot \boldsymbol{\nabla} \tilde{p} \rangle_{\mathrm{s}} \tag{4.14}$$

$$= \langle \boldsymbol{u} \rangle_{\mathrm{s}} \cdot \boldsymbol{\nabla} \langle p \rangle_{\mathrm{i}} + \frac{1}{|V|} \int_{\partial V} \boldsymbol{u} \cdot \boldsymbol{n} \, \tilde{p} \, ds - \langle \mathrm{div}(\boldsymbol{u}) \cdot \boldsymbol{\nabla} \tilde{p} \rangle_{\mathrm{s}}. \tag{4.15}$$

The last term is zero due to incompressibility. Since we assume periodicity, the surface integral also vanishes.

Let us now consider the viscous term in (4.12). Via integration by parts, it can be decomposed into two contributions, representing the diffusion and the pseudo-dissipation of the kinetic energy, respectively (e.g., Pope, 2000):

$$\mu \big\langle \boldsymbol{u} \cdot \boldsymbol{\nabla}^2 \boldsymbol{u} \big\rangle_{\mathrm{s}} = \frac{\mu}{2} \big\langle \boldsymbol{\nabla}^2 (\boldsymbol{u} \cdot \boldsymbol{u}) \big\rangle_{\mathrm{s}} - \mu \langle \boldsymbol{\nabla} \boldsymbol{u} : \boldsymbol{\nabla} \boldsymbol{u} \rangle_{\mathrm{s}}, \tag{4.16}$$

where $\mathbf{A} : \mathbf{B} := \sum_{i,j} A_{ij} B_{ij}$ denotes the Frobenius inner product. The volume integral of the diffusion of kinetic energy $\frac{\mu}{2} \big\langle \boldsymbol{\nabla}^2 (\boldsymbol{u} \cdot \boldsymbol{u}) \big\rangle_{\mathrm{s}}$ vanishes in the case of a periodic domain. Moreover, it can be shown that for incompressible flow in periodic domains, the pseudo-dissipation $\mu \langle \boldsymbol{\nabla} \boldsymbol{u} : \boldsymbol{\nabla} \boldsymbol{u} \rangle_{\mathrm{s}}$ equals the dissipation of kinetic energy $2\mu \langle \boldsymbol{s} : \boldsymbol{s} \rangle_{\mathrm{s}}$, where $\boldsymbol{s} := \frac{1}{2}(\boldsymbol{\nabla} \boldsymbol{u} + (\boldsymbol{\nabla} \boldsymbol{u})^T)$ is the symmetric part of the velocity gradient. Altogether, we can write (4.12) as

$$\frac{\rho}{2} \partial_t \langle \boldsymbol{u} \cdot \boldsymbol{u} \rangle_{\mathrm{s}} + 2\mu \langle \boldsymbol{s} : \boldsymbol{s} \rangle_{\mathrm{s}} = - \langle \boldsymbol{u} \rangle_{\mathrm{s}} \cdot \boldsymbol{\nabla} \langle p \rangle_{\mathrm{i}}. \tag{4.17}$$

This is the balance of the pore scale kinetic energy for a homogeneous and periodic REV under uniform macroscopic flow conditions. The rate of change of kinetic energy on the pore scale (first term) is obtained by the balance of its dissipation (second term) and the power input by the pressure gradient (right hand side). If the unsteady Darcy equation with constant coefficients (4.2) was a good model for unsteady flow in porous media, it should be possible to bring both into a comparable form. In order to do so, we need to introduce some approximations.

First, we show that, for the steady state, the volume-integrated dissipation of kinetic energy is related to the permeability and viscosity. This is done by rewriting the unsteady Darcy

equation (4.2) in the energy form by multiplying it by $\langle \boldsymbol{u} \rangle_\mathrm{s}$:

$$\frac{\tau}{2}\,\partial_t(\langle \boldsymbol{u} \rangle_\mathrm{s} \cdot \langle \boldsymbol{u} \rangle_\mathrm{s}) + \langle \boldsymbol{u} \rangle_\mathrm{s} \cdot \langle \boldsymbol{u} \rangle_\mathrm{s} = -\frac{K}{\mu}\langle \boldsymbol{u} \rangle_\mathrm{s} \cdot \boldsymbol{\nabla}\langle p \rangle_\mathrm{i}. \tag{4.18}$$

Note that τ and K do not necessarily have to be constant in the unsteady case. However, for the *steady* state, i.e., $\partial_t(\,\cdot\,) = 0$, we find by comparing equation (4.17) with equation (4.18) that

$$2\mu\langle \boldsymbol{s} : \boldsymbol{s} \rangle_\mathrm{s} = \mu\langle \boldsymbol{\nabla u} : \boldsymbol{\nabla u} \rangle_\mathrm{s} = \frac{\mu}{K}\langle \boldsymbol{u} \rangle_\mathrm{s} \cdot \langle \boldsymbol{u} \rangle_\mathrm{s}. \tag{4.19}$$

This shows that the steady-state dissipation of the kinetic energy on the pore scale can be expressed by the viscosity, the classical Darcy permeability ($K = K_D$) and the square of the superficial velocity. In order to use equation (4.19) as a closure for the unsteady case, we have to assume that $K = (\langle \boldsymbol{u} \rangle_\mathrm{s} \cdot \langle \boldsymbol{u} \rangle_\mathrm{s})/2\langle \boldsymbol{s} : \boldsymbol{s} \rangle_\mathrm{s}$ does not depart much from its steady-state value. We investigate this question using DNS in section 4.2.5.
Second, to determine whether equation (4.18) can be taken as a good approximation of equation (4.17), we approximate the unsteady term of the latter by

$$\frac{\rho}{2}\partial_t\langle \boldsymbol{u} \cdot \boldsymbol{u} \rangle_\mathrm{s} = \frac{\rho}{2}\partial_t\left(\frac{\langle \boldsymbol{u} \cdot \boldsymbol{u} \rangle_\mathrm{s}}{\langle \boldsymbol{u} \rangle_\mathrm{s} \cdot \langle \boldsymbol{u} \rangle_\mathrm{s}}\langle \boldsymbol{u} \rangle_\mathrm{s} \cdot \langle \boldsymbol{u} \rangle_\mathrm{s}\right) \approx \frac{\rho}{2}\frac{\langle \boldsymbol{u} \cdot \boldsymbol{u} \rangle_\mathrm{s}}{\langle \boldsymbol{u} \rangle_\mathrm{s} \cdot \langle \boldsymbol{u} \rangle_\mathrm{s}}\partial_t\left(\langle \boldsymbol{u} \rangle_\mathrm{s} \cdot \langle \boldsymbol{u} \rangle_\mathrm{s}\right). \tag{4.20}$$

Here, we point out that we neglect the fact that $\frac{\langle \boldsymbol{u} \cdot \boldsymbol{u} \rangle_\mathrm{s}}{\langle \boldsymbol{u} \rangle_\mathrm{s} \cdot \langle \boldsymbol{u} \rangle_\mathrm{s}}$ is, in general, time-dependent. However, as we see from our DNS results in section 4.2.7, this assumption is reasonable, since it does not substantially depart from its steady state, even if sudden changes in the flow occur. The following form of the energy equation is now obtained by substituting equations (4.19) and (4.20) in equation (4.17):

$$\frac{\rho}{2}\frac{\langle \boldsymbol{u} \cdot \boldsymbol{u} \rangle_\mathrm{s}}{\langle \boldsymbol{u} \rangle_\mathrm{s} \cdot \langle \boldsymbol{u} \rangle_\mathrm{s}}\partial_t\left(\langle \boldsymbol{u} \rangle_\mathrm{s} \cdot \langle \boldsymbol{u} \rangle_\mathrm{s}\right) + \frac{\mu}{K_\mathrm{D}}\langle \boldsymbol{u} \rangle_\mathrm{s} \cdot \langle \boldsymbol{u} \rangle_\mathrm{s} = -\langle \boldsymbol{u} \rangle_\mathrm{s} \cdot \boldsymbol{\nabla}\langle p \rangle_\mathrm{i}. \tag{4.21}$$

In the case of a homogeneous and isotropic medium, $\langle \boldsymbol{u} \rangle_\mathrm{s}$ and $\boldsymbol{\nabla}\langle p \rangle_\mathrm{i}$ are parallel, which implies that equation (4.21) can be divided by $|\langle \boldsymbol{u} \rangle_\mathrm{s}|$ and brought into a form corresponding to equation (4.2):

$$\tau_\mathrm{en}\partial_t\langle \boldsymbol{u} \rangle_\mathrm{s} + \langle \boldsymbol{u} \rangle_\mathrm{s} = -\frac{K_\mathrm{D}}{\mu}\boldsymbol{\nabla}\langle p \rangle_\mathrm{i}, \tag{4.22}$$

with the coefficient τ_en being proportional to the ratio of the intrinsic averaged kinetic energy in the pore space versus the kinetic energy of the intrinsic velocity. This leads us to our main result, which is an explicit representation of the time-scale in unsteady porous-media flow:

$$\tau_\mathrm{en} = \frac{K_\mathrm{D}}{\nu}\frac{\langle \boldsymbol{u} \cdot \boldsymbol{u} \rangle_\mathrm{s}}{\langle \boldsymbol{u} \rangle_\mathrm{s} \cdot \langle \boldsymbol{u} \rangle_\mathrm{s}} = \frac{K_\mathrm{D}}{\epsilon\,\nu}\frac{\langle \boldsymbol{u} \cdot \boldsymbol{u} \rangle_\mathrm{i}}{\langle \boldsymbol{u} \rangle_\mathrm{i} \cdot \langle \boldsymbol{u} \rangle_\mathrm{i}}. \tag{4.23}$$

Note that equation (4.22) with (4.23) can be used only if both approximations (4.19) and (4.20) are accurate enough and do not depart too much from their limits in steady flow. We

will address this question by DNS in section 4.2.
The time-coefficient τ_{en} given by equation (4.23) has an interesting property, which we would like to comment on: as a consequence of the Cauchy-Schwarz inequality, it holds that $\langle \boldsymbol{u} \cdot \boldsymbol{u} \rangle_{\mathrm{i}} \geq \langle \boldsymbol{u} \rangle_{\mathrm{i}} \cdot \langle \boldsymbol{u} \rangle_{\mathrm{i}}$, which readily implies that

$$\tau_{\mathrm{en}} \geq \tau_{\mathrm{vans}}. \tag{4.24}$$

Hence, the VANS approach with steady-state closure is the lower limit for our time-coefficient, which is in line with the observations that led to the virtual mass approach. In particular, if the intrinsic averaged kinetic energy in the pore space is in balance with the kinetic energy of the intrinsic velocity, then the pore-scale effects are negligible, and the VANS approach with steady-state closure leads to a reasonable approximation for unsteady porous-media flow.
Note that in the work of Hill et al. (2001), a very similar formulation to the time scale in equation (4.23) was derived. However, there are many differences between their approach and our approach. First, the studying object is different. They mainly focused on flow through sphere packs, and in their model the permeability is replaced by the drag force of the fluid acting on the spheres. Thus this model is not applicable for a general porous medium. While in our approach, we derived a general mathematical expression for all homogeneous and isotropic porous mediums, and applied the permeability explicitly. Thus our model can describe not only spheres, but also cylinders, cubics, etc. More importantly, the way of deriving the time scale is different. Hill et al. (2001) started from the expression of the time-dependent force on each sphere in terms of the virtual mass coefficient, derived by (Sangani et al., 1991), and expressed the time scale in terms of a virtual mass term. They then considered a frame of reference moving with the average velocity, and argued that the rate of change of the kinetic energy is balanced by the dissipation of the kinetic energy and the work done by the drag force. Based on that, they explicitly wrote the energy balance in terms of the spatial deviation of the velocity, which would lead to a similar formulation as the time scale in equation (4.23). However, in our approach, we directly applied the volume-average operator to the energy form of the Navier-Stokes equations, and neglected several terms based on the properties of the fluid and the medium. We also made assumptions which are supported by our DNS results. Our way of deriving the time scale in equation (4.23) is different from that of Hill et al. (2001).

4.1.5 Summary of the different approaches

The coefficients derived by the kinetic energy approach differ from those derived by the VANS approach with steady-state closure or the virtual mass correction. In each derivation, several assumptions have to be made to obtain the unsteady form of Darcy's equation. All approaches are exact in the steady-state limit and $K = K_D$ is the permeability.
In the VANS approach, the interaction term is replaced by the steady-state approximation $\frac{\mu}{K_D}\langle \boldsymbol{u} \rangle_{\mathrm{s}}$, and a constant permeability is being assumed. In the virtual mass approach, an additional virtual mass force is added rendering the interaction term time depending. This virtual mass force can be absorbed into the coefficient in front of the time derivative giving a modified time constant.

In contrast, our approach incorporates permeability by approximating the interaction term $2\mu\langle \boldsymbol{s} : \boldsymbol{s}\rangle_{\mathrm{s}}$ with $\frac{\mu}{K}\langle \boldsymbol{u}\rangle_{\mathrm{s}} \cdot \langle \boldsymbol{u}\rangle_{\mathrm{s}}$. In the steady limit we then find, by comparison with the Darcy equation, that the expression

$$K = \frac{\langle \boldsymbol{u}\rangle_{\mathrm{s}} \cdot \langle \boldsymbol{u}\rangle_{\mathrm{s}}}{2\langle \boldsymbol{s} : \boldsymbol{s}\rangle_{\mathrm{s}}} = \frac{\langle \boldsymbol{u}\rangle_{\mathrm{s}} \cdot \langle \boldsymbol{u}\rangle_{\mathrm{s}}}{\langle \boldsymbol{\nabla u} : \boldsymbol{\nabla u}\rangle_{\mathrm{s}}}, \tag{4.25}$$

which relates the superficial velocity to the volume averaged dissipation of kinetic energy, can indeed be identified with the classical Darcy permeability K_{D}. In order to arrive at the unsteady Darcy equation we have to assume that K as defined by equation (4.25) does not depart much from its steady state.

We summarize in table 4.1 the time-scales resulting from the different approaches.

The time scales obtained from the different derivations represent different physical quantities. All time scales have been derived under the assumptions described in the previous sections. The main assumption, which is common to all approaches, is the one that the coefficients in the unsteady Darcy equation remain constant w.r.t. time in unsteady flow. This is equivalent with assuming self-similar velocity profiles during flow acceleration.

We present here a simple argument that self-similar velocity profiles cannot be expected during flow acceleration. The argument results from the fact that it takes a certain time for the effect of the viscosity to propagate from the solid surface to the core of the flow. This time can be estimated by the viscous time scale in the pore space $\tau_{\mathrm{visc}} = D^2/\nu$, D being a grain diameter. If this time is much smaller than the time scale of the flow acceleration, e.g. τ_{vans}, then self-similar profiles can be expected during flow acceleration. However, if the viscous time scale is much larger than τ_{vans}, then self-similar velocity profiles can not be expected. The flow acceleration is effectuated by the pressure gradient which is irrotational. The unsteady velocity profile shapes therefore depart from the steady-state ones by the viscous effect. To compare τ_{vans} with τ_{visc}, we use the Kozeny-Carman equation (Kozeny, 1927) to estimate the permeability $K = D^2\epsilon^3/(180(1-\epsilon)^2)$. For $\epsilon < 0.5$, we have $K < D^2/180$ and find $\tau_{\mathrm{vans}} \ll \tau_{\mathrm{visc}}$. This renders self-similar velocity profiles very unlikely during flow acceleration.

Concluding, the accuracy of equation (4.2) and its applicability to unsteady flow in porous media depends on how far the individual terms deviate from their steady-state approximations during flow acceleration. We will investigate this issue in the next section using highly resolved numerical simulations of unsteady low-Reynolds number flow in various porous media.

Table 4.1: Different choices for the time-scale in equation (4.2). For practical computations, we propose using the steady-state value τ_{en} of the time-scale of the energy-approach.

VANS	**Virtual mass**	**Volume-averaged energy equation**
$\frac{K_D}{\nu\epsilon}$	$\frac{K_D}{\nu\epsilon}\left[1 + C_{\mathrm{vm}}\frac{1-\epsilon}{\epsilon}\right]$	$\frac{K_{\mathrm{D}}}{\nu\epsilon}\frac{\langle \boldsymbol{u}\cdot\boldsymbol{u}\rangle_{\mathrm{i}}}{\langle \boldsymbol{u}\rangle_{\mathrm{i}}\cdot\langle \boldsymbol{u}\rangle_{\mathrm{i}}}$

4.2 Numerical Results

In the following, we present numerical studies to support the assumptions we made in the derivation of the unsteady Darcy equation (4.22) and its coefficients. Therefore, we compute highly resolved solutions of the full Navier-Stokes equations (2.1) through different configurations of porous media with increasing complexity. In all simulations, the Reynolds numbers, based on pore velocity and pore length scale, are kept on the order of 10^{-3}, which is small enough to ensure that the Forchheimer terms can be neglected.
Before we describe the setup of the simulations, and discuss their results, let us first describe the benchmark problem used throughout this section.

4.2.1 Benchmark problem

For all three test cases, heavy side functions are applied to the x-component of the pressure gradient to drive the flow:

$$\boldsymbol{\nabla}\langle p(t)\rangle_{\mathrm{i}} = p_x \mathbf{e}_x \cdot \begin{cases} 0 & t < 0, \\ 1 & 0 \leq t \leq t_1, \\ 2 & t > t_1, \end{cases} \tag{4.26}$$

Here, $\mathbf{e}_x$ denotes the unit vector in x-direction, p_x is the constant pressure gradient and t_1 is chosen in such a way that the flow first reaches its steady state and then develops again once p_x is doubled.
The analytical solution of the unsteady Darcy equation (4.2) is given by

$$\langle \mathbf{u}(t)\rangle_{\mathrm{s}} = p_x \mathbf{e}_x \cdot \frac{K}{\mu} \cdot \begin{cases} 0 & t < 0, \\ \exp(-t/\tau) - 1 & 0 \leq t < t_1, \\ \exp(-(t-t_1)/\tau) - 2 & t > t_1. \end{cases} \tag{4.27}$$

In this equation, the permeability K is measured from the steady state of the DNS results, which is reached after a sufficient time. The only unknown in this solution is now the time constant τ, which gives us a quality measure to determine the accuracy of the different approaches for this benchmark problem. Let us point out that, in the case of the energy approach, we take τ as the steady-state value τ_{en}.

4.2.2 Simulation setup

The full Navier-Stokes equations (2.1) for an incompressible Newtonian fluid are solved by a finite volume method on a Cartesian grid (Manhart, 2004), where the pore space is represented by an immersed boundary method (Peller et al., 2006; Peller, 2010). For the spatial discretization we use a second-order central scheme, and we advance in time by a low-storage third-order Runge-Kutta method (Williamson, 1980). The solver code is well-validated in various flow configurations, including laminar and turbulent flows; cf., e.g. Breuer et al. (2009); Hokpunna and Manhart (2010); Peller (2010). To ensure accurate and reliable results, we conduct a refinement study for each simulation.

In the following, we denote by D the cylinder diameter and sphere diameter in the two- and three-dimensional cases, respectively, and the channel height in the one-dimensional case. The Reynolds number is then, in all cases, computed by $Re = \langle \boldsymbol{u} \rangle_{\mathrm{s}} \cdot \mathbf{e}_x D/\nu$. We furthermore introduce the pore spacing as H, and we define the blockage ratio as $B = D/H$.

A channel flow at a low Reynolds number can be understood as a prototype for a porous-media flow, with $\epsilon = 1$. Thus, we start with a straight one-dimensional channel with solid walls. In our DNS of the channel flow, we consider a Reynolds number of $Re = 3.35 \times 10^{-3}$. Periodic boundary conditions are applied in stream- and span-wise directions, such that the flow repeats itself periodically.

To increase flow complexity, we consider a two-dimensional flow through an array of regularly placed cylinders. Although, we use this as an idealized configuration to assess our theoretical findings, one could imagine real configurations in which such a geometry could serve as a good model, e.g. a tube bundle in a heat exchanger or an array of plants or a forest. We simulate a box containing one cylinder as indicated in figure 4.1. By using periodic boundary conditions in the directions perpendicular to the cylinder axes, we actually simulate an infinite array of cylinders.

The Reynolds number in the two-dimensional case has been adjusted to $Re = 1.55 \times 10^{-4}$. The grid has a resolution of 480 cells per cylinder diameter D. The blockage ratio is $B = 0.75$, and the porosity can be computed as $\epsilon = 0.5582$. In figure 4.1 (b), streamlines of the steady-state flow are plotted. In the lateral gaps between the cylinders, high steady-state velocities can be observed. Upstream and downstream of the cylinder, the flow reverses and forms a backflow region. The flow field is symmetrical about the two symmetry planes of the cylinder, which is a result of the geometry and the low Reynolds number.

Our three-dimensional simulations are performed on two different configurations.

The first one is a sphere-pack in which the spheres are arranged on a uniform grid with a porosity of $\epsilon = 0.73$, and the blockage ratio is given by $B = 0.8$. The simulation domain is the three-dimensional extension of the one shown in figure 4.1 (a). The Reynolds number is set to $Re = 8.45 \times 10^{-5}$, and we resolve one sphere diameter with 192 grid cells.

The second configuration is the flow through a dense sphere-pack in hexagonal close packing (cf. figure 4.2, a), which results in a porosity of $\epsilon = 0.26$. Periodic boundary conditions are applied in all directions, such that the flow and geometry repeat themselves in space. The Reynolds number is 1.25×10^{-6}, where we resolve one sphere diameter with 400 grid cells. These resolutions are required to compute the dissipation rate with reasonable accuracy during postprocessing since no effort has been made to specially treat the cells cut by the sphere surface, where the maximum dissipation occurs. In Figure 4.2 we plot streamlines for the steady flow field. Unlike in the two-dimensional case, in which the cylinders are arranged on a regular lattice, we can not see any backflow regions.

We assessed the proper grid resolution by a systematic grid study. For the different cases, we simulated the flows with different resolutions. We measured the values of superficial velocity $\langle u \rangle_{\mathrm{s}}$, dissipation $2\mu \langle \boldsymbol{s} : \boldsymbol{s} \rangle_{\mathrm{s}}$ and the factor $\frac{\langle \boldsymbol{u} \cdot \boldsymbol{u} \rangle_{\mathrm{s}}}{\langle \boldsymbol{u} \rangle_{\mathrm{s}} \cdot \langle \boldsymbol{u} \rangle_{\mathrm{s}}}$ at fixed times in steady-state, and we took the results from the finest resolutions as references to calculate the relative errors. Figure 4.3 illustrates the changes of the relative errors with respect to the number of grid points

per D (in channel case $2H$) in log-log plots. We can see that the superficial velocity $\langle u \rangle_{\mathrm{s}}$ and the factor $\frac{\langle \boldsymbol{u} \cdot \boldsymbol{u} \rangle_{\mathrm{s}}}{\langle \boldsymbol{u} \rangle_{\mathrm{s}} \cdot \langle \boldsymbol{u} \rangle_{\mathrm{s}}}$ have a second order convergence with respect to grid spacing. The dissipation has only first order convergence. This can be explained by the post-processing from which we computed the dissipation. We did not pay special attention to treating the velocity gradients at the surface of the spheres/cylinders in the calculation of the dissipation. In the channel flow, not using the Immersed Boundary Method, the dissipation converges with second order as well. In the reference solutions, we used 800 grid cells along the channel hight for the channel case, 480 grid cells per diameter for the cylinder case and 192 grid cells per diameter for the sphere array case. Note that the difference between the second finest grids and reference solutions in the superficial velocity is less than 0.1% in all cases and that the one in the dissipation is around 1%, which essentially implies that the errors in the reference solutions are even smaller.

4.2.3 Velocity profiles during flow acceleration

In this section, we examine velocity profiles during flow acceleration. In figure 4.4 we show velocity profiles at different instances in time for the channel flow (a) and for the flow in the cylinder array (b). The latter is positioned in the smallest gap between two cylinders where the velocity is largest. Note that the profiles are normalized by their instantaneous maximum values. The plots clearly show the deformation of the profile shapes w.r.t. time. In the channel flow, a parabolic profile is obtained at late times. However, at very short times, the flow is essentially a constant profile from which a parabolic profile slowly develops. The change in the profile shape can be interpreted as the interaction of pressure gradient and viscosity. While pressure gradient accelerates the flow uniformly over the channel width, the viscosity slows down the flow from the wall. As both processes act with different time scales, a deformation of the profile is being obtained during the flow acceleration.

The deformation of the velocity profile in the flow through the cylinder array is even more pronounced. Two peaks at the cylinders' walls develop at short times that disappear at late times. At short times the flow is accelerated by the pressure field while the viscosity acts more slowly. Therefore, the flow field tends to be irrotational at very short times[1] which explains the two peaks. At late times the profiles tend towards a profile similar to a parabola due to the influence of the viscosity.

The change in the shape of the velocity profiles let us speculate that flow quantities such as interaction term or dissipation might hardly be linearly dependent on superficial velocity during flow acceleration. We will have a closer look on the relation between superficial velocity and interaction term or dissipation, respectively, in sections 4.2.5 and 4.2.6.

4.2.4 Superficial velocity

In this numerical experiment, we study the development of the superficial velocity in the x-direction, $\langle u(t) \rangle_{\mathrm{s}} := \langle \mathbf{u}(t) \rangle_{\mathrm{s}} \cdot \mathbf{e}_x$, after applying the pressure gradient jumps. In particular, we compare the exact solutions obtained for the time constants from the VANS and energy

[1] (The gradient of the pressure field is irrotational.)

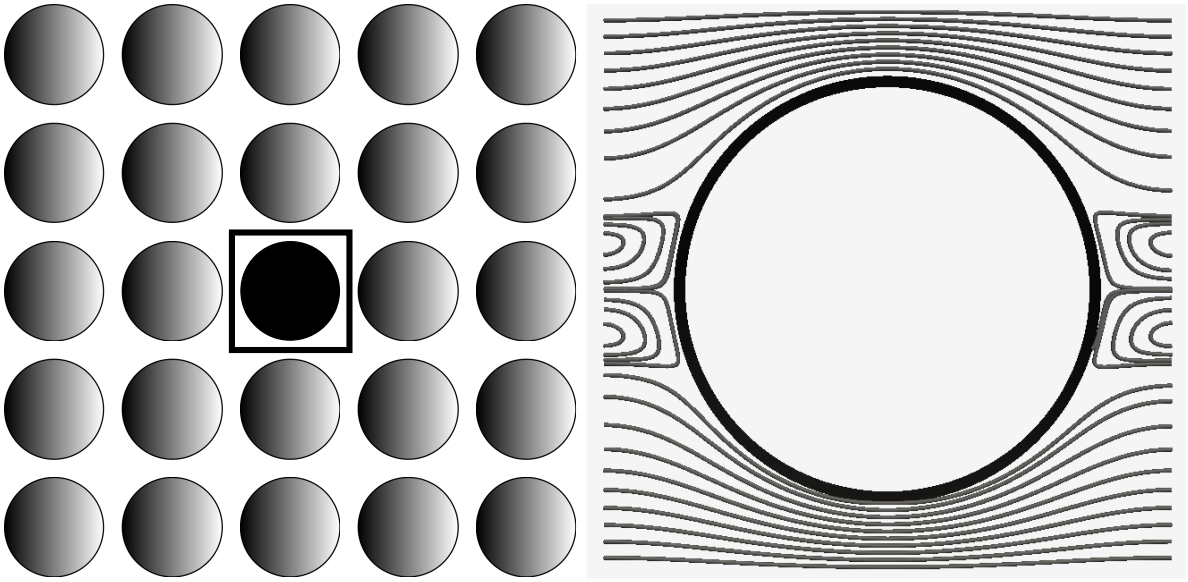

a: illustration **b:** streamlines

Figure 4.1: Two-dimensional simulation. Arrangement of cylinders (2D) and computational box containing one cylinder (a) and streamline plot of flow at low Reynolds number (b).

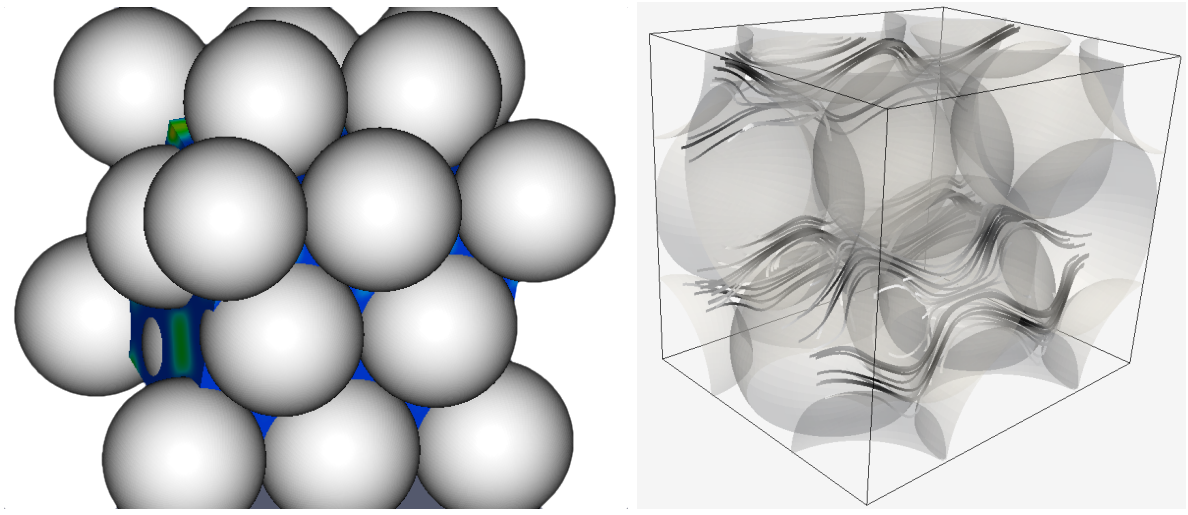

a: illustration **b:** streamlines

Figure 4.2: Three-dimensional simulation of a dense sphere pack. Arrangement of spheres (3D) (a) and streamlines (b).

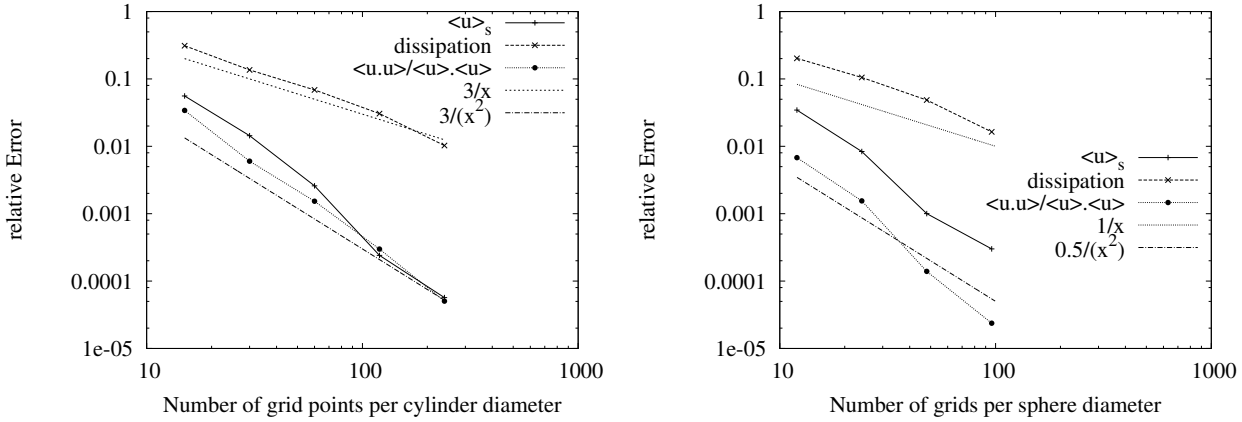

a: cylinder array **b:** sphere array

Figure 4.3: Relative error of superficial velocity, dissipation and ratio between integrated kinetic energy in the pore space and that of the superficial velocity.

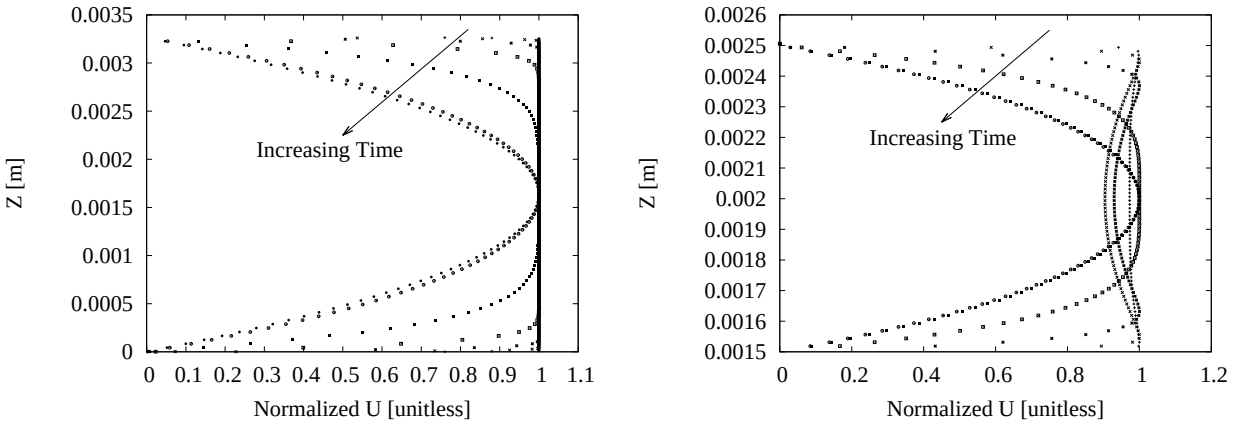

a: channel flow **b:** cylinder array

Figure 4.4: Velocity profiles at different times during flow acceleration. Channel flow (a) and flow in a cylinder array between two cylinders (b).

approaches with the DNS results. We do not include the virtual mass approach here since, in the two- and three-dimensional cases, it would yield the same results as the energy approach for a properly tuned constant C_{vm}.
For the different configurations, we measure the permeability K from the steady-state DNS results. We compute τ_{vans} by equation (4.7) and τ_{en} as defined in equation (4.23), and compare the analytic solutions obtained with the respective time constants to the DNS results.
In figure 4.5, we plot the solutions $\langle u(t)\rangle_{\mathrm{s}}$ obtained by the different approaches as a function of time. The time constant τ_{vans} is, in all cases, smaller than τ_{en}, and does not represent the unsteadiness correctly for this particular example. For the two- and three-dimensional arrangements, the discrepancy is even larger. In the case of a hexagonal sphere-pack with lower porosity $\epsilon = 0.26$, we observe the most significant deviation of the VANS approach with steady-state closure from the DNS results. However, in all experiments, we see that the analytical solution (4.27) of the unsteady Darcy equation closely follows the DNS solution, if the time constant is determined by the energy approach, equation (4.23).

4.2.5 Interaction term

If we neglect the Forchheimer terms in equation (4.5), we obtain the approximation

$$\frac{1}{|V_\beta|}\int_{A_{\beta\sigma}} \boldsymbol{n}_{\beta\sigma}\cdot\left(-\tilde{p}\boldsymbol{I}+\mu\boldsymbol{\nabla}\tilde{\boldsymbol{u}}\right)\,dA = -\frac{\mu}{K_D}\langle\boldsymbol{u}\rangle_{\mathrm{s}},$$

which is used in the derivation of the VANS model of unsteady porous-media flow. While this is undisputed in the steady state, the velocity profiles in section 4.2.3 pose a question regarding the validity of this assumption for unsteady porous-media flow. Hence, we compare the surface filter (interaction term) obtained by DNS with its steady-state approximation, equation (4.5). In all simulations, we observe that, in the steady state, the ratio between interaction term and closure approaches unity, which is consistent with the theory for steady Darcy flow. However, in the unsteady regime, we observe a large discrepancy between the actual interaction term and its closure.
For the different cases, we inspect the approximation of the interaction term by plotting it as a function of its closure (figure 4.6). Here, the diagonal represents the steady-state solution. During the transient phase, large deviations can be observed in which the interaction term is consistently larger than its approximation, thus slowing down the acceleration of the flow compared to the VANS approach with closure (4.5).
From the observations made in our experiments, we conclude that the steady-state approximation of the interaction term leads to an insufficient representation of the physics in the cases under investigation. This is in line with observations from section 4.2.3

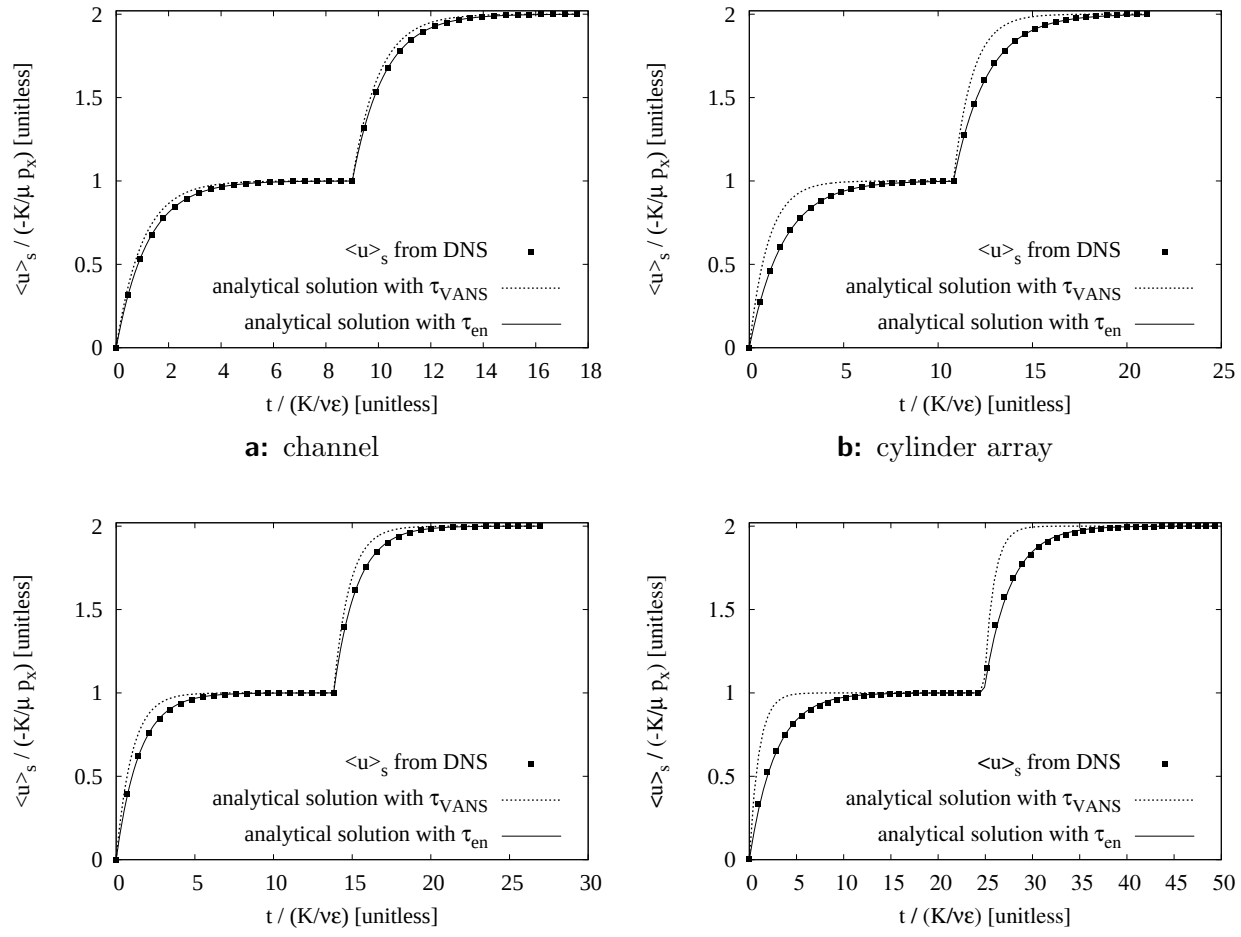

a: channel

b: cylinder array

c: sphere array

d: hexagonal dense sphere pack

Figure 4.5: Comparison of DNS results with analytical solutions using τ_{vans} and τ_{en}.

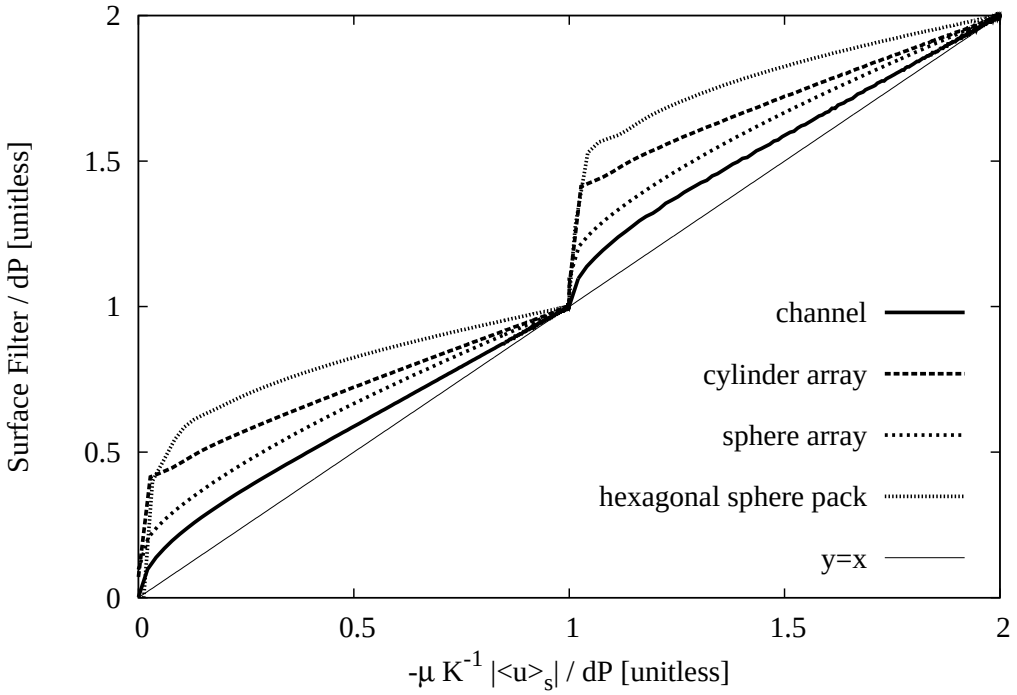

Figure 4.6: Variation of the surface filter $|\frac{1}{|V_\beta|}\int_{A_{\beta\sigma}} \boldsymbol{n}_{\beta\sigma}\cdot(-\tilde{p}\boldsymbol{I}+\mu\boldsymbol{\nabla}\tilde{\boldsymbol{u}})\ dA|$ with $\frac{\mu}{K_D}|\langle\boldsymbol{u}\rangle_{\mathrm{s}}|$.

4.2.6 Dissipation of the kinetic energy

In our derivation using the volume-averaged kinetic energy equation, we introduced the approximation

$$2\mu\langle\boldsymbol{s}:\boldsymbol{s}\rangle_{\mathrm{s}} = \frac{\mu}{K}\langle\boldsymbol{u}\rangle_{\mathrm{s}}\cdot\langle\boldsymbol{u}\rangle_{\mathrm{s}}, \tag{4.28}$$

which is accurate in the steady state. We inspect the quality of the approximation during the transient simulations. In figure 4.7 we observe that the dissipation correlates well with its approximation during flow acceleration. Obviously, the dissipation is less sensitive to the deformations of the velocity profile shapes than the interaction term (mainly wall shear stress). There is a small underprediction of the dissipation, visible as a systematic deviation of the dissipation from its approximation, which is also present for large values, i.e. for large times in the steady state. It is a result of an inconsistency in determining the dissipation by post-processing, which converges by first order, see section 4.2.2. Thus, the approximation of the dissipation of kinetic energy seems to be more reasonable than that of the surface filter by their respective steady-state counterparts.

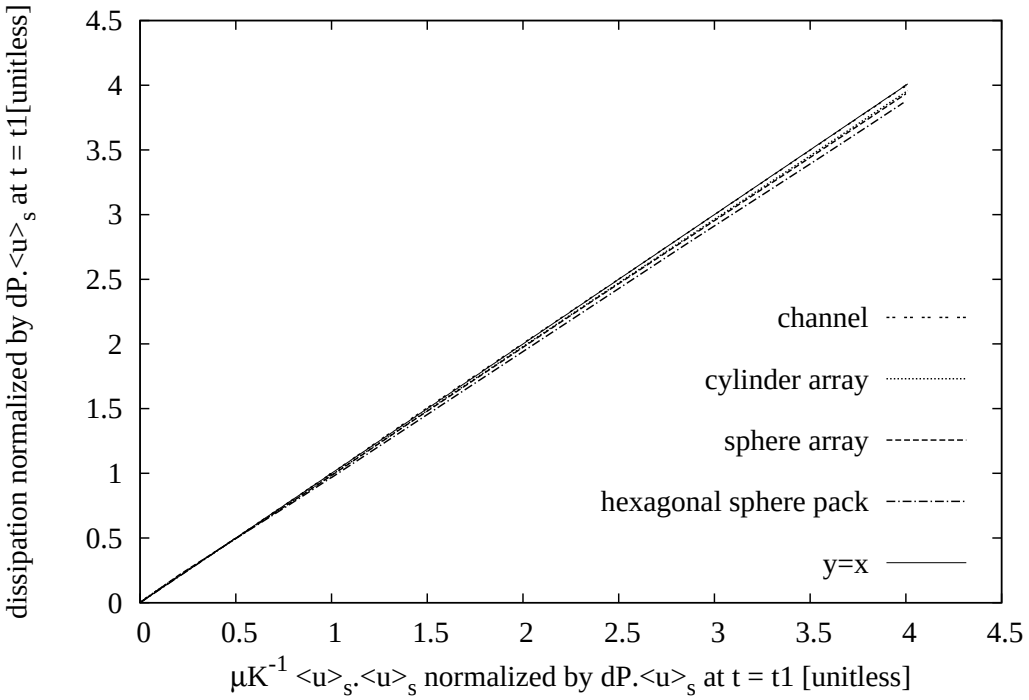

Figure 4.7: Variation of the dissipation $2\mu\langle \boldsymbol{s} : \boldsymbol{s}\rangle_{\mathrm{s}}$ with $\frac{\mu}{K_D}\langle \boldsymbol{u}\rangle_{\mathrm{s}} \cdot \langle \boldsymbol{u}\rangle_{\mathrm{s}}$.

4.2.7 Time-scale

In the derivation of the unsteady Darcy equation, we made a second approximation by assuming in equation (4.20) that

$$\partial_t \frac{\langle \boldsymbol{u} \cdot \boldsymbol{u}\rangle_{\mathrm{i}}}{\langle \boldsymbol{u}\rangle_{\mathrm{i}} \cdot \langle \boldsymbol{u}\rangle_{\mathrm{i}}} \approx 0. \tag{4.29}$$

The purpose of this section is to assess whether this assumption is justified or not.
In figure 4.8, we plot the time dependence of the factor $\frac{\langle \boldsymbol{u} \cdot \boldsymbol{u}\rangle_{\mathrm{i}}}{\langle \boldsymbol{u}\rangle_{\mathrm{i}} \cdot \langle \boldsymbol{u}\rangle_{\mathrm{i}}}$. When the flow starts from rest, we assume the lower limit $\tau = \tau_{\mathrm{vans}}$. However, as the flow develops, our time scale quickly relaxes towards its steady-state value $\tau \to \tau_{\mathrm{en}}$.
At the second step change in pressure, the departure from its steady-state value remains, in all cases, below 10% and then rapidly readjusts to its steady-state value. Hence, in the case of developed flow through porous media, our examples support the assumption that the time scale can be taken as a constant value.
As we can see in figure 4.8, the steady state obtained in the DNS results for the channel flow is at around $\tau_{\mathrm{en}} = 1.2\,\tau_{\mathrm{vans}}$. The analytical solution for steady flow in a channel is a parabolic velocity profile (Batchelor, 1967). From this, we obtain $\tau_{\mathrm{en}} = 1.2\,\tau_{\mathrm{vans}}$. This value is in perfect agreement with our numerical results.
For the two-dimensional cylinder array, the steady state is at about $\tau_{\mathrm{en}} = 1.787\,\tau_{\mathrm{vans}}$ which is even larger than for the channel flow. The largest time scale ratio of our experiments is reached for the hexagonal sphere-pack at a value of 2.747. As shown in section 4.2.4, the

VANS approach with steady-state closure leads to a significant deviation from the actual flow dynamics in this case, whereas the energy approach can accurately represent the unsteadiness of the flow.

4.2.8 Comparison with the virtual mass approach

To assess the dependency of the time constant on the porosity, we conducted several runs with different porosities for the two-dimensional configuration. Here, the size of the cylinder is kept the same, and the domain size (i.e., the distance between the cylinders) is adjusted such that different porosities are obtained. A resolution of 120 grid cells per diameter is maintained by this procedure.

For each porosity, we determined an empirical time constant τ_{dns} by fitting the analytical solution of the unsteady Darcy equation (4.27) to the DNS data of $\langle u(t)\rangle_{\mathrm{s}}$. Those values compare well with those obtained by the energy approach τ_{en}. Both are, however, larger than the time scales obtained by the VANS approach with steady-state closure τ_{vans}. The form of the virtual mass time constant (4.10) implies that

$$\frac{\tau_{\mathrm{vm}}}{\tau_{\mathrm{vans}}} = 1 + \frac{C_{\mathrm{vm}}(1-\epsilon)}{\epsilon} \geq 1. \tag{4.30}$$

We compare the obtained DNS values with $\tau_{\mathrm{vm}}/\tau_{\mathrm{vans}}$ in figure 4.9 for different coefficients C_{vm}. The tendency of the virtual mass term is correct in the sense that it increases with decreasing porosity. However, its slope differs from the slope of the values obtained by DNS. It is not possible to match all the DNS values with one single virtual mass coefficient. From equation (4.30), it can be inferred that the limiting behavior toward $\epsilon \to 1$ is not accurately captured if C_{vm} is taken independently of the porosity ϵ. We included τ_{en} in figure 4.9 for completeness, as it shows good agreement with τ_{dns}.

4.3 Conlusions

To investigate unsteady and linear flow in porous media, we focused on the applicability of the unsteady form of Darcy's equation and its time scale. Our direct numerical simulations of transient flow in the pore space support the use of the unsteady form of Darcy's equation with constant coefficients, although velocity profile shapes have been found not to be self-similar during flow acceleration. The simulations, however, show that the volume-averaged Navier-Stokes system with a steady-state closure for the interaction term underpredicts the time scale in the unsteady Darcy equation. Motivated by these observations, we reviewed existing approaches and presented an alternative way to define a time scale.

We derived the unsteady form of Darcy's equation by starting with the equation of the kinetic energy of the flow in the pore space. The interaction term here represents the dissipation of kinetic energy, which was approximated by its steady-state value using the classical permeability. We demonstrated that this assumption is well-suited in all of our simulations of various configurations, as the dissipation remains very closely proportional to

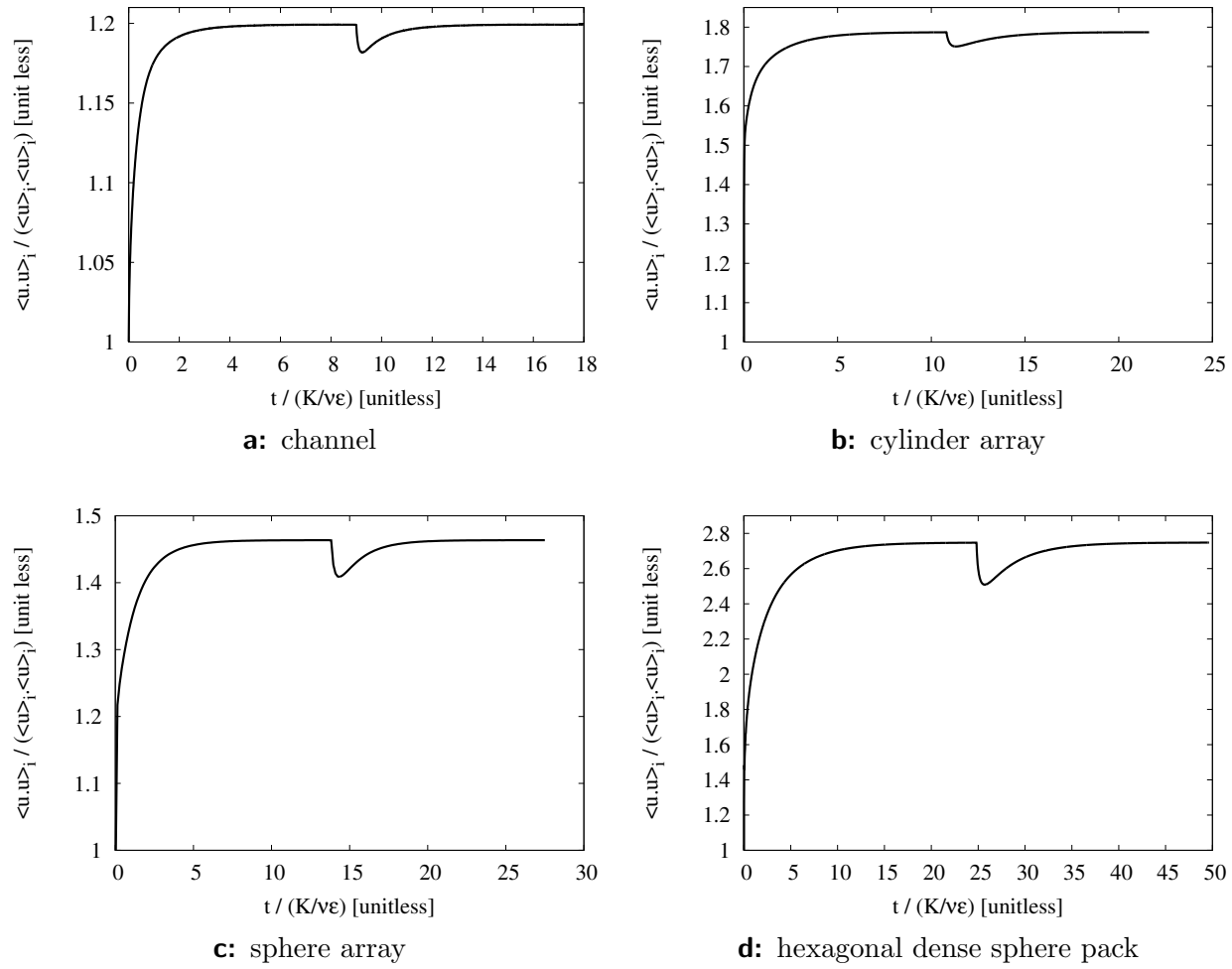

a: channel

b: cylinder array

c: sphere array

d: hexagonal dense sphere pack

Figure 4.8: Temporal variation of $\frac{\langle \boldsymbol{u} \cdot \boldsymbol{u} \rangle_{\mathrm{s}}}{\langle \boldsymbol{u} \rangle_{\mathrm{s}} \cdot \langle \boldsymbol{u} \rangle_{\mathrm{s}}}$ from DNS.

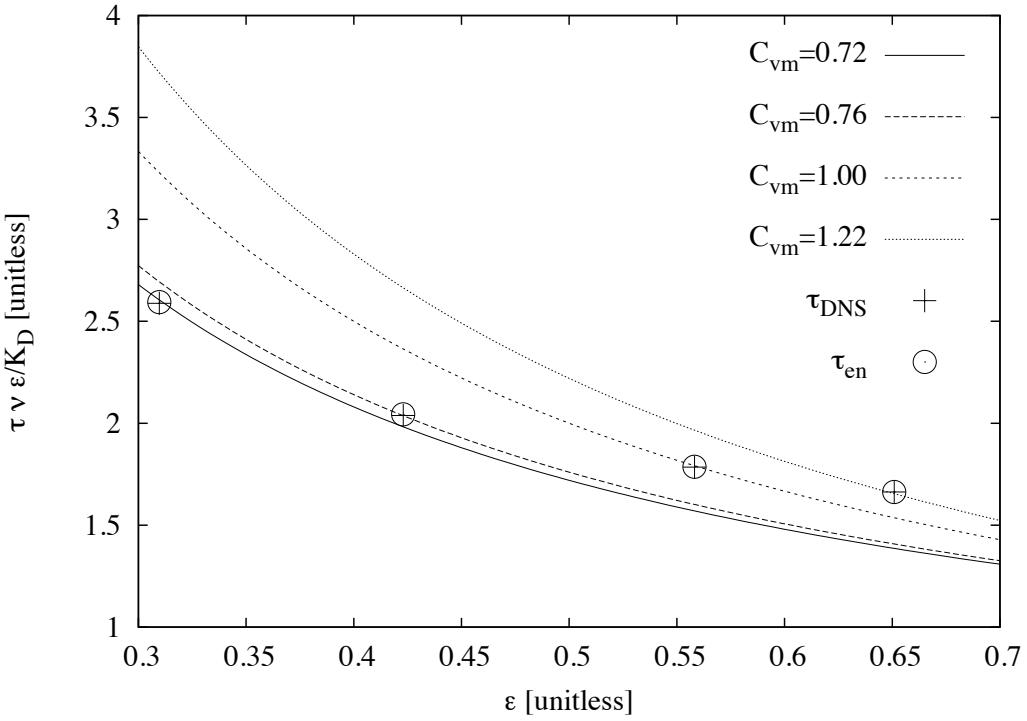

Figure 4.9: Time scales from DNS $\tau_{\mathrm{dns}}/\tau_{\mathrm{vans}}$ compared to $\tau_{\mathrm{en}}/\tau_{\mathrm{vans}}$ and the virtual mass approach $\tau_{\mathrm{vm}}/\tau_{\mathrm{vans}}$ for different virtual mass coefficients C_{vm} as a function of porosity ϵ.

the square of the superficial velocity during the transient phase. The energy approach leads to a different time scale that is proportional to the ratio of the integrated kinetic energy in the pore space to that of the intrinsic velocity. This ratio can be rather large ranging from a value of 1.2 for plain channel flow to 2.75 for a dense sphere pack with hexagonal packing. Our time scale is well in accordance with those evaluated by direct numerical simulation of transient flow in the respective configurations.

The virtual mass approach is qualitatively in line with the findings of this study in that it increases the time scale in the unsteady Darcy equation. However, the dependence of the virtual mass term with porosity cannot be obtained with a constant virtual mass coefficient. We suggest using the time scale obtained by the energy equation approach because it establishes a well-defined quantity. The use of model reduction techniques that allow to determine this quantity without the need for direct numerical simulations is a subject of future research.

5 Part2: Unsteady Darcy Equation for Oscillatory and Linear Flows

Note: most of this part is taken from Zhu and Manhart (2015).
We recall the different time scales derived in section 4.1. The time constant obtained by the *VANS* approach is

$$\tau_{\mathrm{vans}} = \frac{K_{\mathrm{D}}}{\nu\epsilon}; \tag{5.1}$$

the time constant obtained by the *virtual mass* approach is

$$\tau_{\mathrm{vm}} = \frac{K_D}{\nu\epsilon}\left[1 + C_{\mathrm{vm}}\frac{1-\epsilon}{\epsilon}\right]; \tag{5.2}$$

the time constant obtained by the *energy* approach is

$$\tau_{\mathrm{en}} = \frac{K_{\mathrm{D}}}{\epsilon\,\nu}\frac{\langle \boldsymbol{u}\cdot\boldsymbol{u}\rangle_{\mathrm{i}}}{\langle \boldsymbol{u}\rangle_{\mathrm{i}}\cdot\langle \boldsymbol{u}\rangle_{\mathrm{i}}}. \tag{5.3}$$

We introduce the time-scale ratio between the τ_{vans} and τ_{en} as

$$\frac{\tau_{\mathrm{en}}}{\tau_{\mathrm{vans}}} = \frac{\langle \boldsymbol{u}\cdot\boldsymbol{u}\rangle_{\mathrm{i}}}{\langle \boldsymbol{u}\rangle_{\mathrm{i}}\cdot\langle \boldsymbol{u}\rangle_{\mathrm{i}}}. \tag{5.4}$$

In this part, we extend the aforementioned *unsteady* and *linear* porous-media flows to *oscillatory* flow in the *linear* regime, by assuming an oscillatory pressure gradient driving the fluid and a very low Reynolds number. We will concentrate on the following questions: (i) how accurate is an analytical solution of the unsteady Darcy equation with constant time scale and permeability in the case of an oscillatory pressure gradient; (ii) how do velocity fields change within the oscillatory cycle; and (iii) how do coefficients in the unsteady Darcy equation vary within the oscillatory cycle. We use direct numerical simulations of generic porous media geometries and compare coefficients derived by the standard VANS approach to the ones derived by the kinetic energy approach in section 4.1.4.
The part is organized so that, in the next section, the analytical solution of the unsteady Darcy equation is discussed. By comparison with direct numerical simulations of oscillatory flow through generic porous media, we assess the unsteady behaviour of the flow fields, time scale, interaction term and dissipation of kinetic energy, which constitute the coefficients of the unsteady form of the Darcy equation (section 5.2).

5.1 Theory

In this section, we discuss the analytical solution of the unsteady Darcy equation (4.2) for oscillatory flow in porous media. We compare this solution to the analytical solutions for oscillatory flows in pipes (Womersley, 1955) and between parallel plates (Loudon and Tordesillas, 1998), both of which can be regarded as highly simplified models for porous-media capillaries.
If we impose an oscillatory flow by prescribing an oscillatory pressure gradient

$$\boldsymbol{\nabla}\langle p\rangle_{\mathrm{i}}(t) = \Re(\Theta + \Psi e^{i\omega t}) \tag{5.5}$$

where Φ and Ψ are real constants, ω is the real circular frequency, and t is the time, the analytical solution of the unsteady Darcy equation (4.2) is

$$\langle u\rangle_{\mathrm{s}}(t) = \underbrace{\frac{K\Theta}{\mu}(e^{\frac{-t}{\tau}} - 1)}_{\text{transient part}} + \underbrace{\frac{K\Psi}{\mu}\frac{1}{\sqrt{\tau^2\omega^2+1}}}_{\text{amplitude}=A_m(\omega)} \cos(\omega t + \underbrace{\pi - \phi}_{\text{phase lag}=\pi-\phi(\omega)}) \tag{5.6}$$

with the amplitude

$$A_m = \frac{K\Psi}{\mu}\frac{1}{\sqrt{\tau^2\omega^2+1}} \tag{5.7}$$

and the phase lag

$$\phi = \arccos(\frac{1}{\sqrt{\tau^2\omega^2+1}}). \tag{5.8}$$

Here, τ is the time scale, which is dependent on the method used for approximation (either τ_{vans}, τ_{vm} or τ_{en}), and K is the permeability in the unsteady Darcy equation. K does not have to be a constant. However, if we implement either τ_{vans} from the VANS approach or τ_{en} from the energy approach, $K = K_D$ in both methods. The product of the time scale with the circular frequency, $\tau\omega$, can be interpreted as dimensionless frequency.
We can see that the amplitude of the flow rate induced by an oscillating pressure gradient scales like $A_m \propto \omega^{-1}$ for large dimensionless frequencies. For low frequencies, it behaves in a quasi-steady manner, i.e., the instantaneous flow rate is determined by the instantaneous pressure gradient. This can be seen from the amplification factor, i.e., the ratio of the amplitude A_m to the steady-state flow rate $A_{m,ss}$, which can be determined as

$$\frac{A_m}{A_{m,ss}} = \frac{1}{\sqrt{\tau^2\omega^2+1}} \quad . \tag{5.9}$$

This solution can be compared to the ones for oscillating flow in a circular pipe at radius R (Womersley, 1955) and for oscillating flow in a channel between two parallel plates at a channel half width h (Loudon and Tordesillas, 1998). Womersley introduced a dimensionless

frequency, nowadays referred to as the Womersley number, α.

$$\alpha^2 = \omega \frac{R^2}{\nu} \tag{5.10}$$

According to Womersley (1955), the local velocity and volume flow rate in a pipe flow, which is driven by an oscillatory pressure gradient, $\boldsymbol{\nabla}\langle p\rangle_{\mathrm{i}} = \Re(p_0 e^{i\omega t})$ are

$$u(r,t) = \Re\left(\frac{p_0}{\rho}\frac{1}{i\omega}\left[1 - \frac{J_0(\frac{r}{R}\alpha i^{\frac{3}{2}})}{J_0(\alpha i^{\frac{3}{2}})}\right]e^{i\omega t}\right), \tag{5.11}$$

$$Q(t) = \Re\left(\frac{\pi R^2}{\rho}\frac{p_0}{i\omega}\left[1 - \frac{2\alpha i^{\frac{3}{2}}}{i^3\alpha^2}\frac{J_1(\alpha i^{\frac{3}{2}})}{J_0(\alpha i^{\frac{3}{2}})}\right]e^{i\omega t}\right), \tag{5.12}$$

where r is the distance of the local position from the axis of the pipe. J_0 and J_1 are Bessel functions of order zero and one, and with complex argument $\alpha i^{\frac{3}{2}}$. Womersley (1955) further derived this solution into decomposed terms of the Bessel functions, and gave a table which provides discrete values of these terms. Our following discussions concerning Womersley's solution of the pipe flow are based on our Matlab solutions of equation (5.11), which match Womersley's tabulated values well.

According to Loudon and Tordesillas (1998), the solution of the local velocity in a channel flow under the same oscillatory pressure gradient is

$$\begin{aligned} u(y,t) =& \frac{p_0}{\omega\rho\gamma}\left[\sinh\Phi_1(y)\sin\Phi_2(y) + \sinh\Phi_2(y)\sin\Phi_1(y)\right]\cos(\omega t) \\ &+ \frac{p_0}{\omega\rho\gamma}\left[\gamma - \cosh\Phi_1(y)\cos\Phi_2(y) - \cosh\Phi_2(y)\cos\Phi_1(y)\right]\sin(\omega t), \end{aligned} \tag{5.13}$$

where y is the distance of the local position from the channel center plane, $\alpha = h\sqrt{\omega/\nu}$ is the Womersley number, and

$$\begin{aligned} \Phi_1(y) = \frac{\alpha}{\sqrt{2}}\left(1 + \frac{y}{a}\right), \Phi_2(y) = \frac{\alpha}{\sqrt{2}}\left(1 - \frac{y}{a}\right), \\ \gamma = \cosh(\sqrt{2}\alpha) + \cos(\sqrt{2}\alpha). \end{aligned} \tag{5.14}$$

The amplitude of the flow rate in a channel flow under the same oscillatory pressure gradient is

$$\begin{aligned} Q_{\max} =& \frac{2p_0h^3}{\mu\alpha^3}k, \\ k^2 =& \left(\frac{\sinh(\sqrt{2}\alpha)}{\gamma}\right)^2 + \left(\frac{\sin(\sqrt{2}\alpha)}{\gamma}\right)^2 \\ &- \frac{\sqrt{2}\alpha\left[\sinh(\sqrt{2}\alpha) + \sin(\sqrt{2}\alpha)\right]}{\gamma} + \alpha^2. \end{aligned} \tag{5.15}$$

Note that the flow rate per unit width, $Q_{\max}$, represents the integration of the local velocity along the channel height whose unit is $[\frac{m^2}{s}]$.

As both steady-state solutions, for pipe and for channel, can be derived analytically, the permeability and time-scale ratio factors determined in steady states can be computed directly, as given in Table 5.1. Inserting both values into equation (5.1) and (5.3), respectively, gives the expressions of the dimensionless frequencies $\tau_{\text{vans,ss}}\omega$ and $\tau_{\text{en,ss}}\omega$ in terms of Womersley number, where $\tau_{\text{vans,ss}}$ and $\tau_{\text{en,ss}}$ are values of τ_{vans} and τ_{en} determined in steady-state flow driven by a constant pressure gradient.

Table 5.1: Permeability and time-scale ratio factors for pipe flow (Womersley, 1955) and channel flow (Loudon and Tordesillas, 1998).

	permeabiliy	steady-state time-scale ratio	Womersley number	dimensionless frequencies	
	$K = \frac{\mu\langle \boldsymbol{u}\rangle_{\text{s}}}{-\boldsymbol{\nabla}\langle p\rangle_{\text{i}}}$	$\frac{\tau_{\text{en,ss}}}{\tau_{\text{vans,ss}}} = \frac{\langle \boldsymbol{u}\cdot\boldsymbol{u}\rangle_{\text{i}}}{\langle \boldsymbol{u}\rangle_{\text{i}}\cdot\langle \boldsymbol{u}\rangle_{\text{i}}}$		$\tau_{\text{vans,ss}}\omega$	$\tau_{\text{en,ss}}\omega$
pipe flow	$R^2/8$	$\frac{4}{3}$	$\alpha = R\sqrt{\frac{\omega}{\nu}}$	$\frac{1}{8}\alpha^2$	$\frac{1}{6}\alpha^2$
channel flow	$h^2/3$	$\frac{6}{5}$	$\alpha = h\sqrt{\frac{\omega}{\nu}}$	$\frac{1}{3}\alpha^2$	$\frac{2}{5}\alpha^2$

We now compare the amplification factors A/A_{ss}, equation (5.9), with those for channel and pipe flow obtained by equations (5.12) and (5.15). In Figure 5.1 low Womersley numbers and in Figure 5.2 high Womersley numbers are plotted.

One can see that at low frequencies, the amplitude ratios are 1.0, which means a quasi steady-state behaviour for all solutions. We also conclude that all solutions follow the asymptotic behaviour $A_m \propto \alpha^{-2} \propto \omega^{-1}$.

For small Womersley numbers (or lower frequencies) up to $\alpha \lesssim 5$, the analytical solutions by Womersley (1955) and Loudon and Tordesillas (1998) for pipe and channel plotted in Figure 5.1 can be represented by the analytical solutions of the unsteady Darcy equation (4.2), which are obtained using the steady-state time scales, $\tau_{\text{en,ss}}$. While for larger Womersley numbers (or higher frequencies), the analytical solutions by Womersley (1955) and Loudon and Tordesillas (1998) plotted in Figure 5.2 deviate from the analytical solutions of the unsteady Darcy equation (4.2) using $\tau_{\text{en,ss}}$ and approach to the ones using $\tau_{\text{vans,ss}}$. To explain this effect, we discuss the change of the velocity fields with increasing frequency (Womersley, 1955; Loudon and Tordesillas, 1998).

At low frequencies, or quasi-steady states, the profiles form similar shapes as the profiles in the steady-states, which are, for instance, parabolic functions in a channel flow. As frequency increases, the profiles asymptotically approach to a uniform profile due to a decreasing viscous layer depth $\delta^\nu \propto \sqrt{\nu/\omega}$. For channel and pipe flow, the viscous layer depth is given by

$$\frac{\delta^\nu}{R} = \sqrt{\frac{2}{\tau\omega}}. \tag{5.16}$$

We now recall that $\tau_{\text{en}} = \frac{K_{\text{D}}}{\epsilon\,\nu}\frac{\langle \boldsymbol{u}\cdot\boldsymbol{u}\rangle_{\text{i}}}{\langle \boldsymbol{u}\rangle_{\text{i}}\cdot\langle \boldsymbol{u}\rangle_{\text{i}}}$. The term $\frac{K_{\text{D}}}{\epsilon\,\nu}$ obviously remains constant over the whole frequency range, while the time-scale ratio $\frac{\langle \boldsymbol{u}\cdot\boldsymbol{u}\rangle_{\text{i}}}{\langle \boldsymbol{u}\rangle_{\text{i}}\cdot\langle \boldsymbol{u}\rangle_{\text{i}}}$ varies with varying profile shapes,

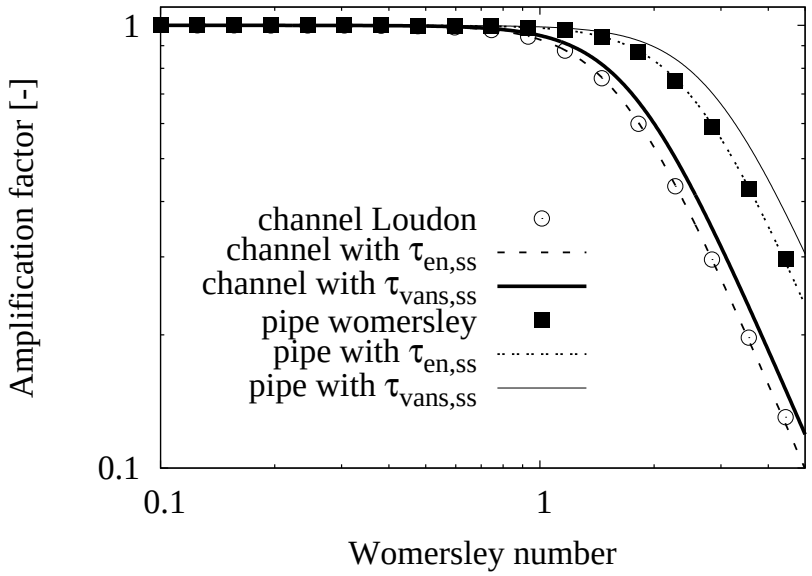

Figure 5.1: Amplification factors of oscillatory superficial velocities for channel and pipe flow. Compared are analytical solutions by Womersley (1955) and Loudon and Tordesillas (1998) with analytical solutions of the unsteady Darcy equation (4.2) using $\tau_{\text{en,ss}}$ and $\tau_{\text{vans,ss}}$, at low Womersley numbers

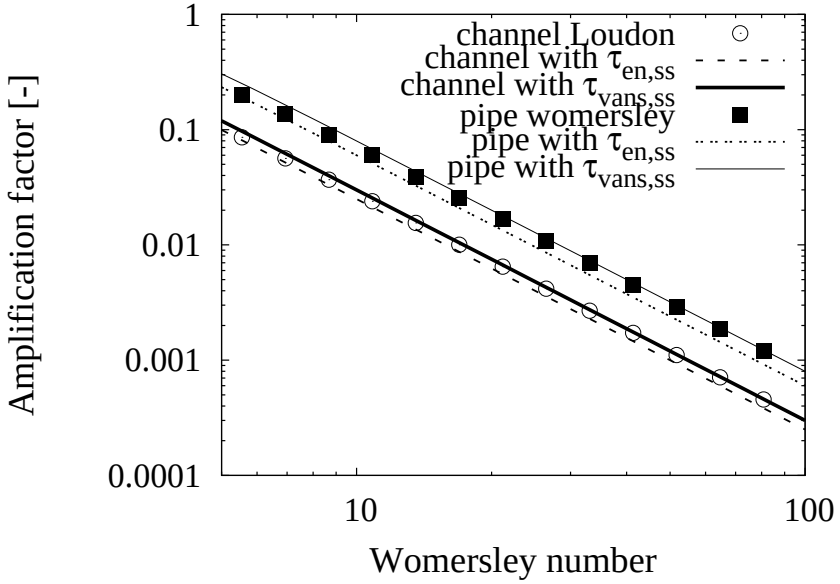

Figure 5.2: Amplification factors of oscillatory superficial velocities for channel and pipe flow. Compared are analytical solutions by Womersley (1955) and Loudon and Tordesillas (1998) with analytical solutions of the unsteady Darcy equation (4.2) using $\tau_{\text{en,ss}}$ and $\tau_{\text{vans,ss}}$, at high Womersley numbers.

as frequency changes. At low frequencies, or quasi-steady states, because the profile shapes remain similar to those in steady-state flows, the values of $\frac{\langle \boldsymbol{u} \cdot \boldsymbol{u} \rangle_\mathrm{i}}{\langle \boldsymbol{u} \rangle_\mathrm{i} \cdot \langle \boldsymbol{u} \rangle_\mathrm{i}}$ remain the same as those in steady-state flows. Thus the value of τ_en at low frequencies, which we call $\tau_\mathrm{en,lf}$, equals the steady-state time scale, $\tau_\mathrm{en,ss}$. At high frequencies, however, as profiles approach uniform profiles, the time scale ratio $\frac{\langle \boldsymbol{u} \cdot \boldsymbol{u} \rangle_\mathrm{i}}{\langle \boldsymbol{u} \rangle_\mathrm{i} \cdot \langle \boldsymbol{u} \rangle_\mathrm{i}}$ approaches 1.0. Thus the value of τ_en at high frequencies, $\tau_\mathrm{en,hf} = \tau_\mathrm{vans,ss}$. This means that the amplitudes at high frequencies are underestimated when using the $\tau_\mathrm{en,ss}$, as $\tau_\mathrm{en,hf}$ is obviously smaller than $\tau_\mathrm{en,ss}$ (Zhu et al., 2014), and the amplitude of asymptotic solution of the unsteady Darcy equation (4.2) at high frequencies is given as

$$A_m / A_{m,ss} = (\tau\omega)^{-1}. \tag{5.17}$$

Using $\tau_\mathrm{en,ss}$ to estimate the amplitude at high frequencies, the amplitude of oscillating pipe flow is underestimated by a factor of 3/4, and the amplitude of oscillating channel flow is underestimated by a factor of 5/6.

The conclusion from this analysis is that the unsteady Darcy equation, together with the constant steady-state time scale, $\tau_\mathrm{en,ss}$, cannot be used over the complete range of frequencies for oscillatory flow in pipes and channels. For low frequencies, it represents a good model, provided the time scale is adjusted to $\tau_\mathrm{en,ss}$ for quasi-steady flow. For high frequencies, the values of τ_en change due to the change of the velocity profiles and asymptotically reaches $\tau_\mathrm{vans,ss}$ as the time-scale ratio reaches unity. The amplitude error is given by the ratio of the respective time scales. Displayed in Figure 5.1 and 5.2, $\tau_\mathrm{en,ss}$ gives the most accurate solutions at low frequencies and so do $\tau_\mathrm{vans,ss}$ at high frequencies. However, the essential point is that at both low and high frequencies, only the frequency-dependent values of τ_en, which are $\tau_\mathrm{en,lf}$ (and it equals to $\tau_\mathrm{en,ss}$) and $\tau_\mathrm{en,hf}$ (and it equals to $\tau_\mathrm{vans,ss}$), respectively, give accurate analytical solutions to the unsteady Darcy equation (4.2).

The question arises: How does the unsteady Darcy equation predict the amplitude ratios for oscillating flow in more complex porous media, and how can time scales and permeabilities be described as function of dimensionless frequency? This question will be addressed in the next section, using numerical simulations of oscillating flow through various porous configurations as a reference.

5.2 Numerical Results

We examine the questions raised in the previous section with Direct Numerical Simulations (DNS). For various geometries, which will be introduced in the following sections, we computed highly resolved solutions of the full Navier-Stokes equations. We ran a series of DNS with different frequencies, ω, prescribing Θ and Ψ in the oscillatory pressure gradient. In all simulations, the Reynolds numbers, based on pore velocity and pore length scale, were kept on the order of 10^{-3}, which is small enough to ensure that non-linear effects can be neglected. We measured the amplitude A_m and phase lag α of the oscillating superficial velocity as a function of frequency, and compared those with solutions of the unsteady Darcy equation. We examined flow fields, interaction terms and dissipation of kinetic energy for various cases, which allowed us to explain the effects observed.

5.2.1 Simulation setup

The full Navier-Stokes equations for an incompressible Newtonian fluid were solved by a finite volume method on a Cartesian grid (Manhart, 2004), where the pore space was represented by an immersed boundary method (Peller et al., 2006; Peller, 2010). For the spatial approximations, we used second-order central schemes, and we advanced time by a low-storage, third-order Runge-Kutta method (Williamson, 1980). The solver code is well-validated in various flow configurations, including laminar and turbulent flows (e.g., Breuer et al., 2009; Hokpunna and Manhart, 2010; Peller, 2010), and for flow in porous media (Zhu et al., 2014). In all cases, the flow was driven by a pressure gradient that has been implemented as a volume force in the momentum equation. This enables one to use periodic boundary conditions for the pressure field which essentially represents the pressure deviation from the spatially averaged pressure including the driving pressure gradient.

In the following section, we denote D as the cylinder and sphere diameters in the two- and three-dimensional cases, respectively. The Reynolds number is then, in all cases, computed by $Re = |\langle \boldsymbol{u} \rangle_s| D/\nu$. Furthermore, we introduce a pore spacing as the distance between spheres or cylinders, H, and we define the blockage ratio as $B = D/H$. Unless stated otherwise, we use the 'natural' time scale $\tau = K_D/(\nu\epsilon)$ to make time or frequency dimensionless.

We started with a two-dimensional flow through an array of regularly placed cylinders. Although we used this as an idealized configuration to assess our theoretical findings, one could imagine real configurations in which such a geometry could serve as a good model, e.g., a tube bundle in a heat exchanger or an array of plants or a forest. We simulated a box containing one cylinder, as indicated in Fig. 5.3 (a). By using periodic boundary conditions in pressure and velocity fields in the directions perpendicular to the cylinder axes, we actually simulated an infinite array of cylinders.

The Reynolds number in the two-dimensional case was adjusted to be below $Re = 3.40 \times 10^{-4}$. The grid had a resolution of 240 cells per cylinder diameter D. According to Eq. (5.16), a dimensionless frequency of $\tau\omega = 10^3$ would still give about ten computational points in the viscous layer δ^ν. The blockage ratio is $B = 0.75$, and the porosity can be computed as $\epsilon = 0.5582$. The time-scale ratios according to equation (5.4), as they have been computed for low and high frequencies are given in table 5.2.

Our three-dimensional configuration consisted of flow through a dense sphere-pack in hexagonal close packing (see Fig. 5.3, b), which resulted in a porosity of $\epsilon = 0.26$. Periodic boundary conditions in pressure and velocity fields were applied in all directions, such that the flow and geometry repeated themselves in space. The Reynolds number was set to be below $Re = 1.23 \times 10^{-6}$, where we resolved one sphere diameter with 160 grid cells. The time-scale ratios obtained at low and high frequencies according to equation (5.4) are given in table 5.2.

We assessed the proper grid resolution by a systematic grid study. For the different cases, we simulated the flows with different resolutions. We measured the values of the amplitude, A_m, and the phase lag, ϕ, at highest frequencies for both cylinder array and sphere pack, and we took the results from the finest resolutions as references to calculate the relative errors. Figure 5.4 illustrates the changes of the relative errors with respect to the number of grid points per D in log-log plots. We can see that the amplitude, A_m, has a second order convergence with respect to grid spacing, while the phase lag, ϕ, generally converges

Table 5.2: Time-scale ratios for the 2D flow through an array of cylinders and the 3D flow through a dense sphere pack at low and high frequencies.

	cylinder	sphere pack
low frequency	1.787	2.657
high frequency	1.499	1.837

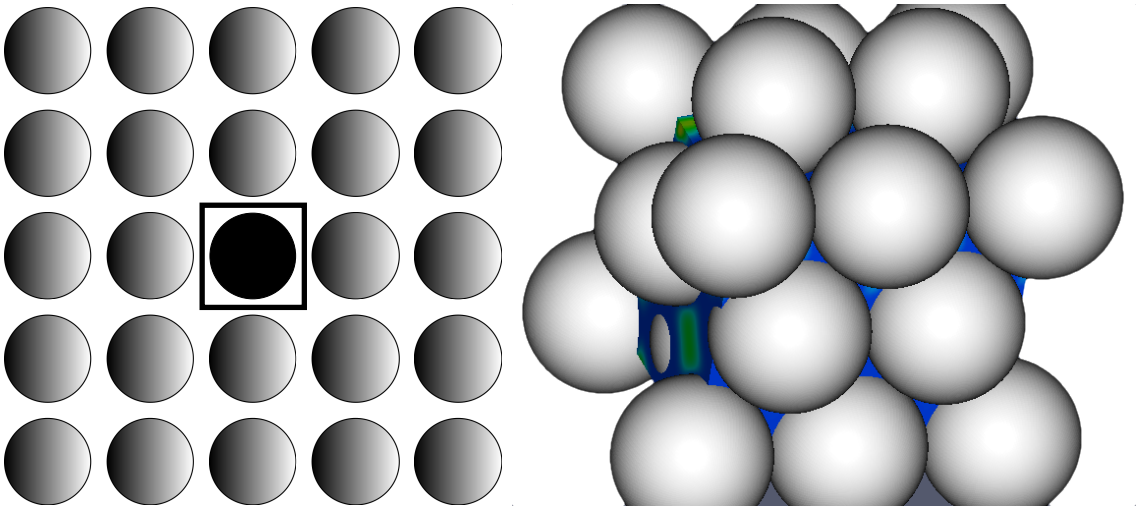

Figure 5.3: Geometries of the simulations performed. Arrangement of cylinders (2D) and computational box containing one cylinder (a), and arrangement of spheres in a dense sphere pack (b).

by a first order. In the reference solutions, we used 240 grid cells per cylinder diameter, and 160 grid cells per sphere diameter. In the cylinder array, the differences between the second finest grids and reference solutions in both the amplitude and phase lag are less than 0.072%. In the sphere pack, these numbers are 2.68% in amplitude and 0.61% in phase lag. Note that the errors in the reference solutions are even smaller. Moreover, these grid studies are conducted at the highest frequencies, where the viscous layer depth, equation (5.16), obtains the smallest values. At lower frequencies, as the viscous layer depth increases significantly, the same resolutions obtain much more accuracy.

5.2.2 Superficial velocity

The superficial velocities were measured in each case. In the cylinder array, the time development of the superficial velocities during flow acceleration, with frequencies $\omega K_D/(\nu\epsilon) = 0.462$ and $\omega K_D/(\nu\epsilon) = 4.62$, are represented in Fig. 5.5 as an example.
We observed a superposition of a transient and an oscillatory motion, as expected. For flows in the same geometry configuration but with higher frequencies, it was observed clearly that the amplitude of the oscillation was much smaller than for those with lower frequencies. This is in line with Eq. (5.7).
We measured the amplitudes, A_m, of the superficial velocity as a function of the frequency, ω, of the oscillatory pressure gradient (Eq. (5.5)) at late times after the transient, in which we observed purely oscillatory behaviour.
For both cylinder array and dense sphere pack, the values for oscillatory amplification factors, $Am/A_{m,ss}$, from DNS are represented with symbols in Fig. 5.6. The analytical solutions of Eq. (5.7), $\frac{1}{\sqrt{\tau^2\omega^2+1}}$, using $\tau = \tau_{\text{vans,ss}}$ and $\tau = \tau_{\text{en,ss}}$, are plotted in dashed and solid lines, respectively. We observe that, for both cases, the analytical solutions with $\tau = \tau_{\text{en,ss}}$ compare well with the DNS results at small and medium frequencies ($\omega K_D/(\nu\epsilon) \lesssim 2.5$), while the ones with $\tau = \tau_{\text{vans,ss}}$ considerably depart from the DNS solution.
For large frequencies, such as $\omega K_D/(\nu\epsilon) \gtrsim 5$, the amplification factors measured in the DNS are slightly larger than the ones predicted by Eq. (5.7) using $\tau_{\text{en,ss}}$. This effect resembles the one observed for pipe and channel flow. In the latter cases, the velocity profiles are dependent on the dimensionless frequency. At high frequencies, the time-scale ratio (5.4) tends towards unity. Regarding the change in the time-scale ratio leads to better predictions of the flow amplitudes at high dimensionless frequencies. In real porous domains, the time-scale ratio will always be larger than 1.0 due to the tortuous flow paths in the pore space. We computed the respective frequency dependent time-scale ratio, Eq. (5.4), at the lowest frequencies, $\tau_{\text{en,lf}}$, and at the highest frequencies, $\tau_{\text{en,hf}}$. Because at low frequencies, the velocity profiles are similar to the ones in steady states, the time-scale ratios (5.4) remain the same as the ones in steady states. Thus $\tau_{\text{en,lf}} = \tau_{\text{en,ss}}$, and we did not show $\tau_{\text{en,lf}}$ specifically in the plots. While at high frequencies, as aforementioned, the time-scale ratios (5.4) decrease, thus $\tau_{\text{en,hf}} < \tau_{\text{en,ss}}$, and the solutions of the Darcy equation using $\tau_{\text{en,hf}}$ are added in Fig. 5.7, which renders high-frequency flow amplitudes in a cylinder array and a sphere pack. It may be seen that the solutions using $\tau_{\text{en,hf}}$ fit better to the DNS results at high dimensionless frequencies. Using the steady-state time-scale ratio results in an underestimation of the flow amplitudes by factors of 1.192 in the cylinder array and 1.447 in the sphere pack.
Note that at high frequencies, the flow amplitudes remain below 1% of those of the steady-

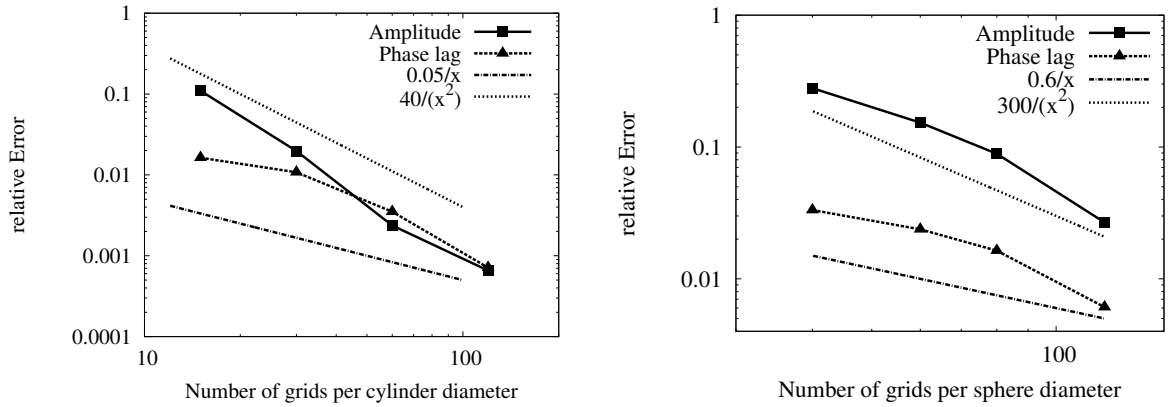

a: cylinder array **b:** sphere pack

Figure 5.4: Relative error against grid resolution in a two-dimensional cylinder array (a), and a three-dimensional dense sphere pack (b).

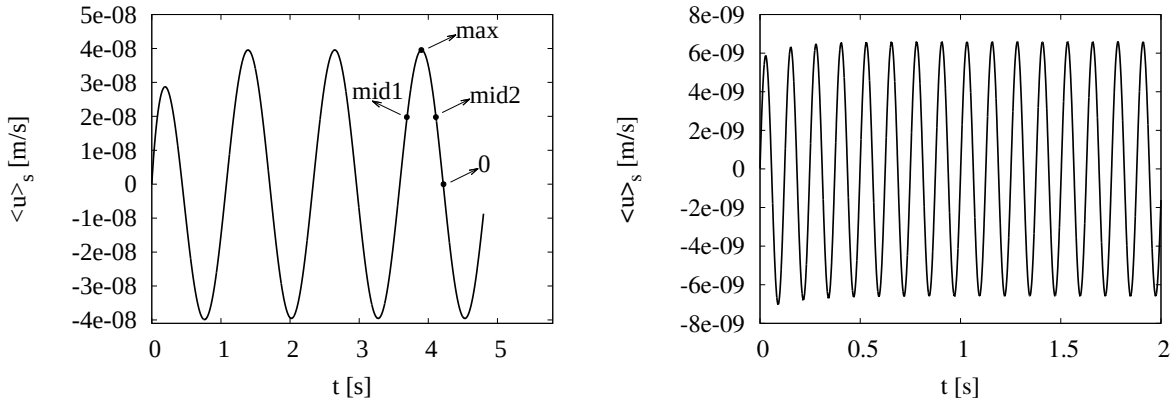

a **b**

Figure 5.5: Superficial velocity during initial phase in a cylinder array. Frequencies $\omega K_D/(\nu\epsilon) = 0.462$ (a), and $\omega K_D/(\nu\epsilon) = 4.62$ (b).

state flows, and for the analytical solutions with $\tau = \tau_{\text{vans,ss}}$, there is a much larger gap with respect to the DNS results at any frequency.

5.2.3 Phase lag

In analogy to the oscillatory amplitude, the phase lag, ϕ, between the superficial velocity and the prescribed pressure gradient was measured, and can be seen in Fig. 5.8 as a function of the frequency, ω. For both cases of the cylinder array and dense sphere pack, the analytical solutions with $\tau = \tau_{\text{en,ss}}$ compare well with the DNS results, while the solutions with $\tau = \tau_{\text{vans,ss}}$ show a much larger gap. Moreover, according to Eq. (5.8), when ω approaches infinity, the phase lag, ϕ, approaches $\pi/2$. This is consistent with the results shown in Fig. 5.8. As all solutions converge to the same value, there is no difference between the different time scales at large frequencies.

5.2.4 Velocity profiles

We have demonstrated that the time scale in the unsteady Darcy Eq. (4.2) changes at large dimensionless frequencies as a consequence of a change in the time-scale ratio, as given by Eq. (5.4). For oscillatory pipe and channel flows, this is due to the shrinking of the viscous layer depth, δ^{ν}, with increasing dimensionless frequency. This leads to a flattening of the profiles for pipe or channel flows. We inspected instantaneous velocity profiles at low and high frequencies together with their real and imaginary parts, to explore their change with frequency. Note that the instantaneous velocity profiles might have influence on heat and mass transfer in oscillatory porous-media flow.

Fig. 5.9 demonstrates the change of the velocity fields with oscillation frequency. It renders streamlines around a 2D cylinder at low (a) and high (b) frequencies, both at the instance of maximum superficial velocity. At low frequencies, the streamlines are identical to the ones in steady-state flow. Although the Reynolds number is small and the flow is in the linear regime, backflow occurs in the streamwise gap between two cylinders. This is a viscous effect. In inviscid flow as well as at large frequencies (b), the backflow disappears as the flow field follows a potential flow solution with the pressure gradient as potential.

The velocity profiles between two cylinders at different instances in the oscillatory cycle are plotted in Fig. 5.10. The instances “mid1, max, mid2, 0”, marked in Fig. 5.10, are illustrated in Fig. 5.5 (a). At medium frequencies (Fig. 5.10, a) we observed that at the instances when the superficial velocity reaches its positive oscillation peak (max) and positive mid values (mid1 and mid2), the profiles resemble a parabolic shape within the gap between the two cylinder walls. But at zero superficial velocity (0), there is forward and backward flow that cancels out the superficial velocity.

At large dimensionless frequencies, the profiles are substantially different (see Fig. 5.10, b). In the center part of the gap, the profiles remain flat throughout the whole cycle. Between the flat center part and the wall of the cylinder, a local maximum has developed. This can be taken as indication that the profiles at large frequencies resemble a potential flow solution, except in a thin layer at the wall that is affected by viscosity. As in the low-frequency case, we see positive and negative velocities in the profile at zero superficial velocity, giving rise to

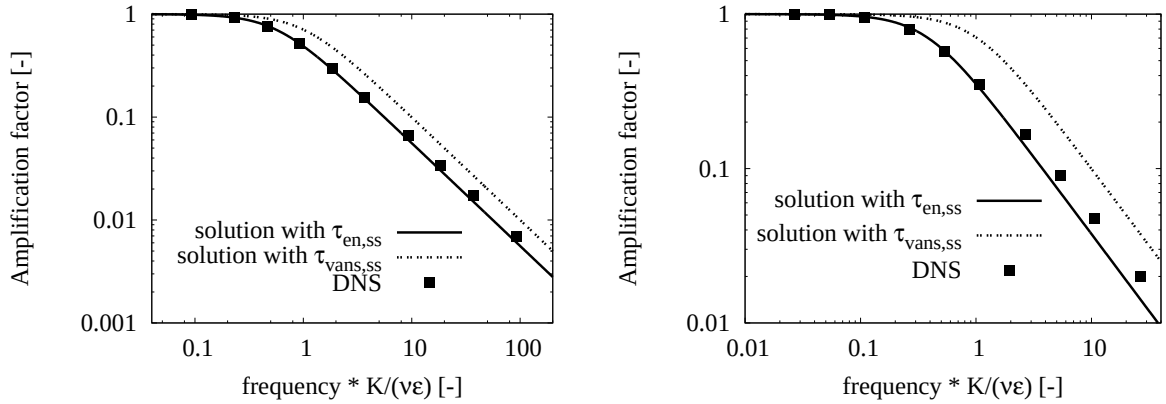

a: cylinder array **b:** sphere pack

Figure 5.6: Amplification factors of the oscillatory superficial velocity with respect to frequency normalized by $K_D/(\nu\epsilon)$. In a two-dimensional cylinder array (a), and a three-dimensional dense sphere pack (b).

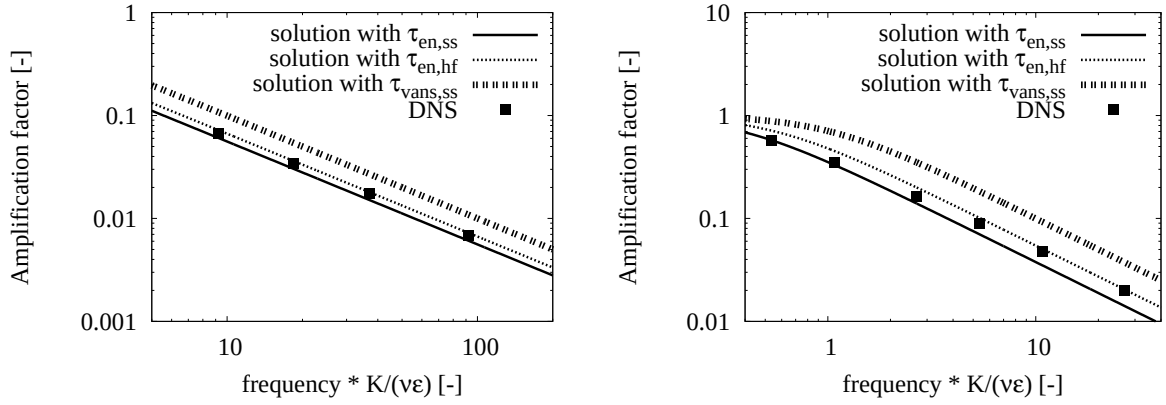

a: cylinder array high freq **b:** sphere pack high freq

Figure 5.7: Amplification factors at high frequencies, in a cylinder array (a), and in a dense sphere pack (b).

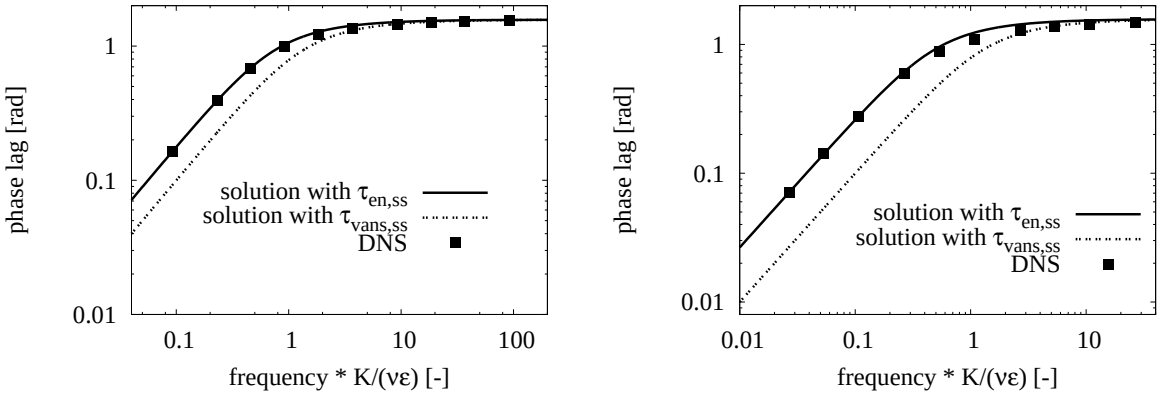

a: cylinder array **b:** sphere pack

Figure 5.8: Oscillation phase lag with respect to frequency, in a cylinder array (a), and in a dense sphere pack (b).

the conclusion that the flow will never be completely at rest.
majority of the profile shape change accurs in a very small time interval close to the zero point.
In addition to the velocity profiles taken at times adjusted to the velocity cycle, we inspected the real and imaginary parts of the velocity profiles, which were taken at the times when the pressure gradient was at its maximum (real part of the velocity) and when the pressure gradient was zero (imaginary part of the velocity profile), as shown in Fig. 5.11. All profiles are normalized by their individual maximum value. At a low dimensionless frequency, $\omega K_D/(\nu\epsilon) = 0.5$, real and imaginary profiles are close to a parabolic shape. At a medium frequency, $\omega K_D/(\nu\epsilon) = 5.0$, the real part develops a complicated shape with two inflection points, two local maxima and a local minimum. The imaginary part is still close to a parabolic shape. At the largest frequency, $\omega K_D/(\nu\epsilon) = 50$, real and imaginary parts have two inflection points and two local maxima. While the real part has positive and negative velocities, the imaginary part does not show a zero crossing.

5.2.5 Interaction term and dissipation of the kinetic energy

We have demonstrated that in all cases considered, the time scale obtained by the energy approach, $\tau_{\text{en,ss}}$, gives good agreement between solutions of the unsteady Darcy equation and analytical or DNS results. On the other hand, the steady-state closure for the interaction term does not comply to analytical or DNS results. While the latter relies on the steady-state closure for the interaction term for the volume-averaged momentum equation (VANS approach), the former relies on the volume-averaged equation for the kinetic energy in the flow. The time scale obtained by the energy approach is larger than the one obtained by the momentum equation, which explains the different solutions. Both approaches differ only in the time scale, which has different meanings. In the volume-averaged momentum equation, the instantaneous pressure force balances the instantaneous interaction force and the rate

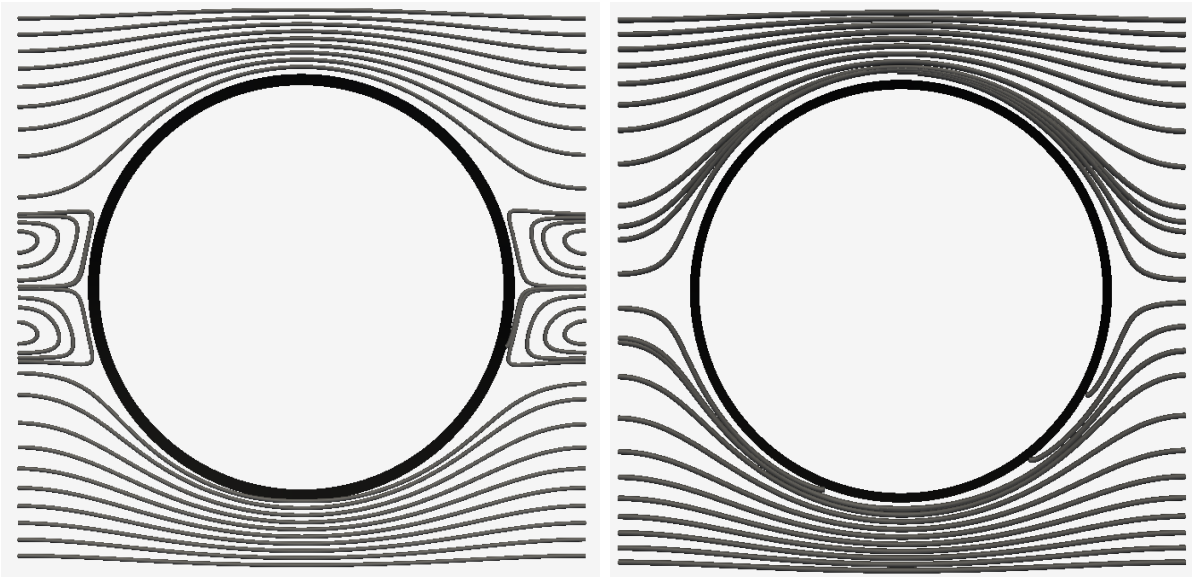

Figure 5.9: Two-dimensional simulation. Streamlines at maximum velocity amplitude for low frequencies (a), and streamlines at maximum velocity amplitude at high frequencies (b).

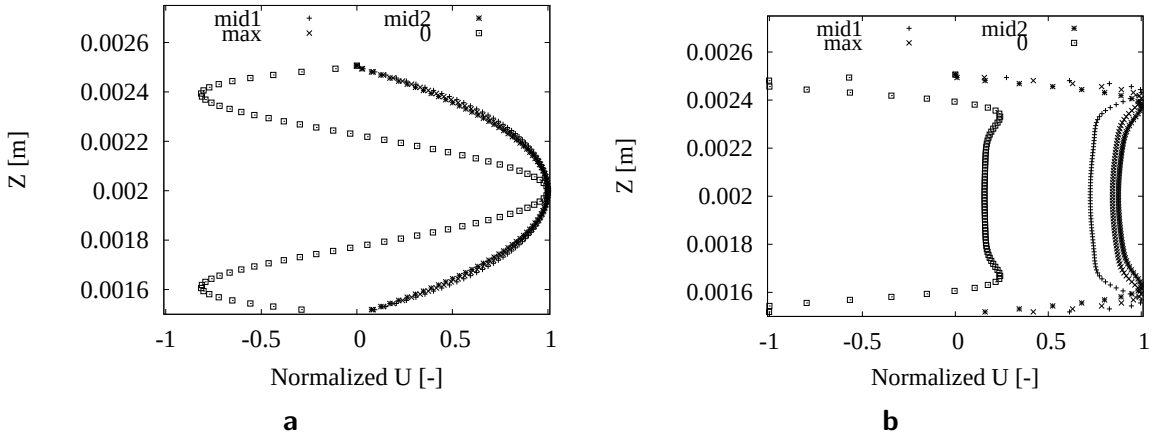

Figure 5.10: Streamwise velocity profile at different times during flow oscillation between two cylinders. All are normalized by their peak values. Oscillatory frequencies are $\omega K_D/(\nu\epsilon) = 0.462$ (a), and $\omega K_D/(\nu\epsilon) = 92.5$ (b).

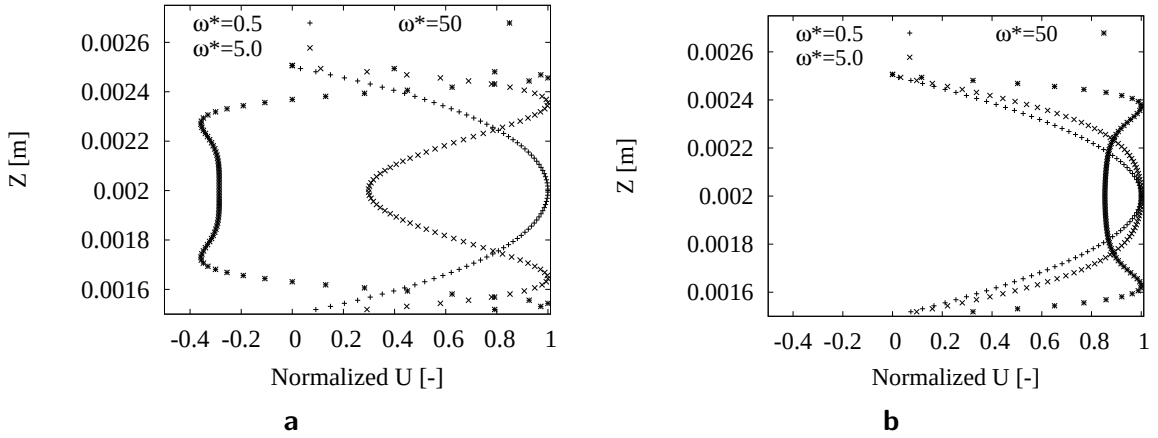

Figure 5.11: Streamwise velocity profiles between two cylinders. All are normalized by their peak values. Real (a) and imaginary (b) parts of $\widetilde{U}$ at three different dimensionless frequencies, $\omega^* = \omega K_D/(\nu\epsilon)$.

of change of momentum of the flow. In the volume-averaged kinetic energy equation, the instantaneous energy input by the pressure gradient balances the instantaneous dissipation of kinetic energy and rate of change of kinetic energy. In the momentum equation, the interaction term needs to be closed, which has been done by using the steady-state closure. In the kinetic energy approach, the ratio of kinetic energy in the pore space to the kinetic energy of the superficial velocity, i.e., the time-scale ratio given in Eq. (5.4), and the instantaneous dissipation of kinetic energy need to be modelled. We have demonstrated in the previous sections that the time-scale ratio is dependent on the oscillation frequency due to a change in the velocity fields. In what follows, we investigate the interaction term and the dissipation of kinetic energy obtained from our DNS data base.

Fig. 5.12 plots the interaction term against its steady-state closure in oscillatory flow in a cylinder array. The interaction term computed by DNS shows hysteretic behaviour for low and high dimensionless frequencies. Modeling this term by the steady-state closure leads to errors of more than 30% of the maximum at the low frequency and of more than 80% of the maximum at the high frequency. The maximum value of the closure remains below 15% of the maximum of the DNS at the high frequency. Modeling the interaction term by the steady-state closure seems inappropriate in oscillatory flow. The hysteretic behaviour is present at low frequencies and explains the observed phase differences between DNS and the unsteady Darcy equation using τ_{vans} (compare to Fig. 5.8).

The dissipation of kinetic energy behaves differently (see Fig. 5.13). At low frequencies, there is a nearly perfect match between the instantaneous dissipation and its closure, without a hysteretic behaviour. At high frequencies, the dissipation shows a hysteresis as well. The instantaneous errors made by the closure remain below 40%, which doesn't seem to be negligible, but is smaller than the errors observed in the steady-state closure of the interaction term. Moreover, the largest modelled dissipation is at about 85% of the one from DNS. These observations make modelling the dissipation of kinetic energy much easier than modelling the interaction term. This supports the better amplitude and phase-lag predictions from the kinetic energy approach and the suitability of the time-scale ra-

tio.

5.3 Conlusions

We have investigated oscillatory flow through various porous media configurations. We considered two formulations of the unsteady form of Darcy's equation, one derived by volume-averaging the momentum equation and one by volume-averaging the equation for the kinetic energy. In both formulations, steady-state closures for the interaction term and the dissipation of the kinetic energy, respectively, were used. With these closures, both approaches differed in the time scale. The time-scale ratio is given by the ratio of the kinetic energy in the pore space to the kinetic energy of the superficial velocity.

The analytic solution of the unsteady Darcy equation complies well with analytic solutions of laminar oscillatory pipe and channel flows if the proper time scale is chosen. For low frequencies up to $\omega K_D/(\nu\epsilon) \approx 2.5$, the steady-state time-scale ratio fits well, as instantaneous velocity profiles tend to assume a parabolic shape. For larger frequencies, the time-scale ratio goes towards unity as the viscous layer tends towards zero and the velocity profiles flatten. This would infer different time scales for small and large frequencies.

Direct numerical simulations of oscillatory flow through cylinder arrays and sphere packs reveal similar findings as for oscillatory channel and pipe flow. The unsteady Darcy equation is able to predict the amplitude damping and phase lag accurately if the proper time scale is chosen. At low to medium dimensionless frequencies, the time scale, $\tau_{\mathrm{en,ss}}$, computed from steady-state velocity, represents the flow dynamics considerably better than the time scale derived by volume-averaging the momentum equation together with the steady-state closure of the interaction term. At high frequencies, the time-scale ratio computed from high-frequency pore-scale velocity fields is more accurate than the one computed from the steady state. This can be explained by the transition of the pore-scale velocity fields from viscous ones to inviscid ones with diminishing viscous layer thicknesses. The amplitude and phase lag errors, however, remain small, irrespective of whether low or high frequency velocity fields are used for computing the time-scale ratio.

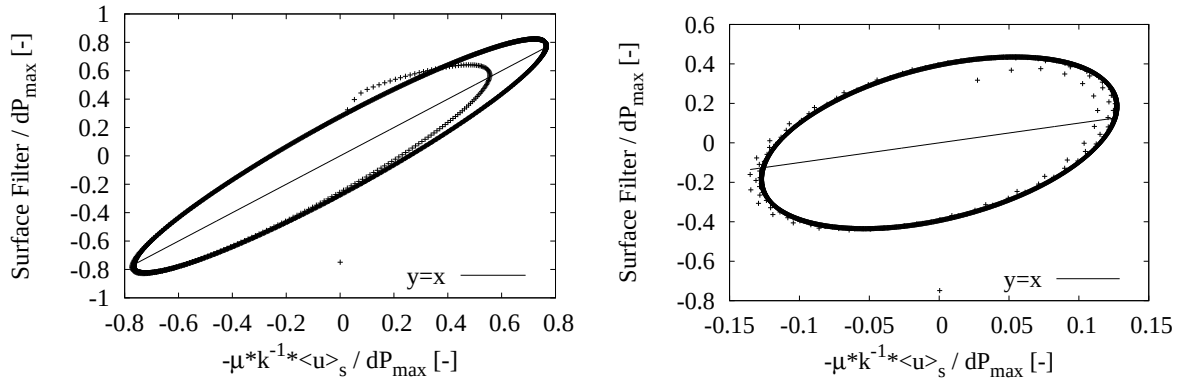

a: $\omega K_D/(\nu\epsilon) = 0.462$ **b:** $\omega K_D/(\nu\epsilon) = 4.62$

Figure 5.12: Variation of the interaction term (surface filter) $|\frac{1}{|V_\beta|}\int_{A_{\beta\sigma}} \boldsymbol{n}_{\beta\sigma}\cdot(-\tilde{p}\boldsymbol{I}+\mu\boldsymbol{\nabla}\tilde{\boldsymbol{u}})\ dA|$ with $\frac{\mu}{K_D}|\langle\boldsymbol{u}\rangle_{\mathrm{s}}|$ at $\omega K_D/(\nu\epsilon) = 0.462$ (a) and $\omega K_D/(\nu\epsilon) = 4.62$ (b) during flow oscillations.

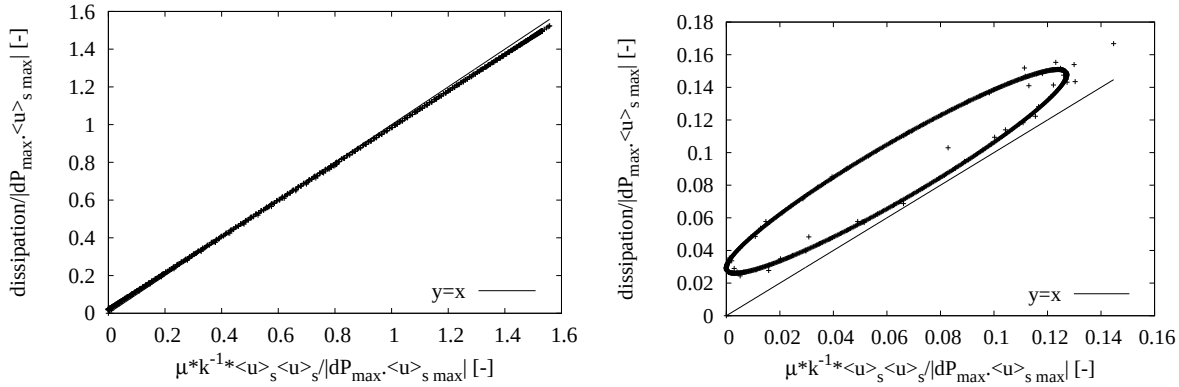

a: $\omega K_D/(\nu\epsilon) = 0.462$ **b:** $\omega K_D/(\nu\epsilon) = 4.62$

Figure 5.13: Variation of the dissipation of kinetic energy $2\mu\langle\boldsymbol{s}:\boldsymbol{s}\rangle_{\mathrm{s}}$ with $\frac{\mu}{K_D}\langle\boldsymbol{u}\rangle_{\mathrm{s}}\cdot\langle\boldsymbol{u}\rangle_{\mathrm{s}}$ at $\omega K_D/(\nu\epsilon) = 0.462$ (a) and $\omega K_D/(\nu\epsilon) = 4.62$ (b) during flow oscillations.

6 Part3: Non-linear Effects in Unsteady Flows, and the Unsteady Forchheimer Equation

In this part, we focus on *unsteady* and *non-linear* flows. We mainly investigate two problems: (I) which physical variable determines the onset of the non-linear effects in unsteady flows; (II) whether the unsteady Forchheimer equation (1.4) with constant coefficients a, b and c is accurate in describing unsteady and non-linear flows. We use fully resolved *direct numerical simulation (DNS)* of the flow in the pore space to assess these questions. We analyze the DNS results to identify the determining variable. We then compare the DNS results to the Matlab solutions of the unsteady Forchheimer equation (1.4) to assess its applicability. Let us first start with the onset of the non-linear effects.

6.1 Onset of the Non-linear Effects in Unsteady Porous-media Flows

There exist different theories concerning the reason that causes the onset of the non-linear effects in unsteady porous-media flows. It has been attributed to different concepts such as turbulence (e.g. Tek et al., 1962), the microscopic inertial forces (e.g. Bear, 1972; MacDonald et al., 1979; Cvetkovic, 1986), or the increased microscopic drag forces on the porous walls (e.g. Hassanizadeh and Gray, 1987). Despite these different theories, it is widely accepted that the steady-state pore Reynolds number is the dominant variable that determines the onset of the non-linear effects in steady flows (e.g. Dullien and Azzam, 1973; Whitaker, 1996; Blick, 1966; Hassanizadeh and Gray, 1987; Coulaud et al., 1988; Papathanasiou et al., 2001; Fourar et al., 2004; Mazaheri et al., 2005; Mei and Auriault, 1991; Firdaouss et al., 1997; Koch and Ladd, 1997; Souto and Moyne, 1997; Rojas and Koplik, 1998; Jacono et al., 2005; Lasseux et al., 2011), i.e., when the pore Reynolds number, Re_{pore}, is comparable to unity, the non-linear effects set in. In unsteady flows, however, to the author's best knowledge, no similar agreements have been made so far.

To answer this question, we conducted fully resolved *direct numerical simulation (DNS)* inside the fluid. For various geometries, which will be introduced in the following sections, we computed highly resolved solutions of the full Navier-Stokes equations. We ran a series of DNS with different constant prescribing pressure gradients, $\boldsymbol{\nabla}\langle p\rangle_{\text{i}}$, to drive the flows from still, until the fluids have reached steady state. The values of the constant prescribing pressure gradients, $\boldsymbol{\nabla}\langle p\rangle_{\text{i}}$, were assigned with values in different orders of magnitude in such a way that the steady-state pore Reynolds numbers, $Re_{\text{pore,ss}}$, range from 0 to around 200, such that we were able to compare both linear and non-linear flows.

Note that we define the steady-state pore Reynolds number as

$$Re_{\text{pore,ss}} = \frac{|\langle \boldsymbol{u}_{,\text{ss}} \rangle_{\text{s}}| d}{\nu} \tag{6.1}$$

where $|\langle \boldsymbol{u}_{,\text{ss}} \rangle_{\text{s}}|$ is the magnitude of the steady-state superficial velocity, d is the pore/grain size and ν is the kinematic viscosity.
Before we describe the setup of the simulations, and discuss their results, let us first describe the benchmark problem used throughout this section.

6.1.1 Benchmark problem

For all test cases, heavy-side functions are applied to the x-component of the pressure gradient to drive the flow:

$$\boldsymbol{\nabla} \langle p(t) \rangle_{\text{i}} = p_x \mathbf{e}_x \cdot \begin{cases} 0 & t < 0, \\ 1 & 0 \leq t \leq t_1 \end{cases} \tag{6.2}$$

Here, $\mathbf{e}_x$ denotes the unit vector in x-direction, p_x is the constant pressure gradient and the flow reaches its steady state already before t_1.
If the pressure gradient p_x is prescribed in such a way (with very small values) that the flow is always in the linear region, the unsteady Darcy equation would apply, as discussed in section 4.2.1. The analytical solution of the unsteady Darcy equation (4.2) is given by

$$\langle \mathbf{u}(t) \rangle_{\text{s}} = p_x \mathbf{e}_x \cdot \frac{K}{\mu} \cdot \begin{cases} 0 & t < 0, \\ \exp(-t/\tau) - 1 & 0 \leq t < t_1. \end{cases} \tag{6.3}$$

We normalize the superficial velocity $\langle \mathbf{u}(t) \rangle_{\text{s}}$ by $p_x \cdot \frac{K}{\mu}$, and reformulate equation (6.3) to get

$$\langle \mathbf{u}(t) \rangle_{\text{s}} / \left(p_x \cdot \frac{K}{\mu} \right) = \mathbf{e}_x \cdot \begin{cases} 0 & t < 0, \\ \exp(-t/\tau) - 1 & 0 \leq t < t_1. \end{cases} \tag{6.4}$$

From the previous studies in Chapter 4, we already know that the time scale $\tau = \tau_{\text{en}} = \frac{K_{\text{D}}}{\epsilon \nu} \frac{\langle \boldsymbol{u} \cdot \boldsymbol{u} \rangle_{\text{i}}}{\langle \boldsymbol{u} \rangle_{\text{i}} \cdot \langle \boldsymbol{u} \rangle_{\text{i}}}$ is accurate for all unsteady and linear flows, and this time scale is independent of the variation of the pressure gradient, p_x. This means that, as long as the flow is in the linear regime, the normalized superficial velocity always has the identical mathematical expression. In other words, as long as the flow is linear, all normalized plots of the superficial velocities $\langle \mathbf{u}(t) \rangle_{\text{s}} / \left(p_x \cdot \frac{K}{\mu} \right)$ against the time t will be an identical linear curve, despite the variation of the pressure gradient p_x. Moreover, if a deviation from this linear curve is observed, this deviation marks the instant at which the non-linear effects set in. We expect the observation of such a deviation in flows with much larger pressure gradients, p_x.

Note that, when the geometry of the porous medium and the fluid properties are certain, $\tau = \tau_{\mathrm{en}}$ is certain, and equation (6.4) is sufficient to describe the linear curve, without the time, t, being normalized by any physical quantity. However, in our numerical simulations in the next sections, it makes no harm to normalize the time, t, by the time scale, τ_{en}, to make it dimensionless.

We further investigate which physical variable determines the onset of the non-linear effects in unsteady porous-media flows. To do so, we must first find a quantity from which we can deduce the onset of the non-linear effects. In this case, the relative deviation of the aforementioned non-linear curves from the linear curve is a good choice, and we denote this deviation $\sigma_u(t)$. To calculate $\sigma_u(t)$, we denote a very low pressure gradient, p_{x_0}, which produces a very low superficial velocity, $\langle \mathbf{u_0}(t) \rangle_{\mathrm{s}}$, and thus a linear flow. We then denote a high pressure gradient, p_{x_h}, which produces a high superficial velocity, $\langle \mathbf{u_h}(t) \rangle_{\mathrm{s}}$, and thus a non-linear flow. The relative deviation, $\sigma_u(t)$, of the aforementioned non-linear curve from the linear curve is then

$$\sigma_u(t) = 1 - \frac{\underbrace{\langle \mathbf{u_h}(t) \rangle_{\mathrm{s}} \cdot \mathbf{e}_x / \left(p_{x_h} \cdot \frac{K}{\mu} \right)}_{\text{non-linear curve}}}{\underbrace{\langle \mathbf{u_0}(t) \rangle_{\mathrm{s}} \cdot \mathbf{e}_x / \left(p_{x_0} \cdot \frac{K}{\mu} \right)}_{\text{linear curve, equation (6.4)}}}, \tag{6.5}$$

where $\langle \mathbf{u_0}(t) \rangle_{\mathrm{s}}$ and $\langle \mathbf{u_h}(t) \rangle_{\mathrm{s}}$ can both be obtained from the DNS results, and we expect that $\langle \mathbf{u_0}(t) \rangle_{\mathrm{s}}$ to be close to the analytical solution in equation (6.4).

It is obvious that only when σ_u is large enough, we can observe the onset of the non-linear effects. Plotting σ_u against any variable (e.g., the instantaneous pore Reynolds number $Re_{\mathrm{pore}}(t)$), and identifying the correlation between σ_u and that variable (e.g., $Re_{\mathrm{pore}}(t)$), would enable us to identify which variable determines the onset of the non-linear effects in unsteady porous-media flows.

In the next sections, we will use fully resolved DNS results in the pore space with various complexities to assess these derivations.

6.1.2 Simulation setup

The full Navier-Stokes Eqs. (2.1) for an incompressible Newtonian fluid were solved by a finite volume method on a Cartesian grid (Manhart, 2004), where the pore space was represented by an immersed boundary method (Peller et al., 2006; Peller, 2010). For the spatial approximations, we used second-order central schemes, and we advanced the time by a low-storage, third-order Runge-Kutta method (Williamson, 1980). The solver code is well-validated in various flow configurations, including laminar and turbulent flows (e.g., Breuer et al., 2009; Hokpunna and Manhart, 2010; Peller, 2010), and for flow in porous media (Zhu et al., 2014). In all cases, the flow was driven by a pressure gradient that has been implemented as a volume force in the momentum equation. This enables one to use periodic boundary conditions for the pressure field which essentially represents the

pressure deviation from the spatially averaged pressure including the driving pressure gradient.

In the following sections, we denote D as the cylinder and sphere diameters in the two- and three-dimensional cases, respectively. The pore Reynolds number is then, in all cases, computed by $Re_{\text{pore}} = |\langle \boldsymbol{u} \rangle_{\text{s}}| D/\nu$. Furthermore, we introduce a pore spacing as the distance between spheres or cylinders, H, and we define the blockage ratio as $B = D/H$. Unless stated otherwise, we use the time scale τ_{en} to make time dimensionless.

We started with a two-dimensional flow through an array of staggered cylinders. We simulated a box containing one cylinder at the center and four quarter cylinders at the corners, as indicated in Fig. 6.1 (a). By using periodic boundary conditions in pressure and velocity fields in the directions perpendicular to the cylinder axes, we actually simulated an infinite array of staggered cylinders. The grid had a resolution of 96 cells per cylinder diameter D. The blockage ratio is $B = 0.6$, and the porosity can be computed as $\epsilon = 0.4345$.

Our three-dimensional simulations are performed on two different configurations.

The first one is a sphere-pack in which the spheres are arranged on a uniform grid with a porosity of $\epsilon = 0.7319$, and the blockage ratio is given by $B = 0.8$. The simulation domain is the three-dimensional extension of the one shown in figure 6.1 (b). We resolve each sphere diameter with 48 grid cells.

The second configuration is the flow through a dense sphere-pack in hexagonal close packing (cf. figure 6.2, a), which results in a porosity of $\epsilon = 0.26$. Periodic boundary conditions are applied in all directions, such that the flow and geometry repeat themselves in space. We resolve each sphere diameter with 40 grid cells. In Figure 6.2 we plot streamlines for the steady-state flow field.

6.1.3 Normalized superficial velocity

In this numerical experiment, we study the development of the superficial velocity in the x-direction, $\langle u(t) \rangle_{\text{s}} := \langle \mathbf{u}(t) \rangle_{\text{s}} \cdot \mathbf{e}_x$, after applying the heavy-side pressure gradient. We plot the normalized superficial velocities, $\langle \mathbf{u}(t) \rangle_{\text{s}} / \left(p_x \cdot \frac{K}{\mu} \right)$, as discussed in equation (6.4), in figure 6.3 for all three cases. To obtain the aforementioned linear curves, the pressure gradients were selected in such a way that the steady-state pore Reynolds numbers are $Re_{\text{pore}} = 1.72 \times 10^{-5}$ for 2D cylinder array, $Re_{\text{pore}} = 8.47 \times 10^{-5}$ for 3D sphere array and $Re_{\text{pore}} = 1.23 \times 10^{-6}$ for 3D dense sphere pack. The steady-state values of the normalized superficial velocities, $\langle \mathbf{u}(t) \rangle_{\text{s}} / \left(p_x \cdot \frac{K}{\mu} \right)$, for all linear flows, will approach 1, because of the Darcy's law. Although not displayed in the figures, our simulations have shown that when $Re_{\text{pore}} \ll 1$, all plots for linear flows in each case lie on top of each other and become a linear curve, because the flows are in the linear regime and equation (6.4) simply applies. As we increase the orders of magnitude of the prescribed pressure gradients used to drive the flows, the pore Reynolds numbers Re_{pore} increase, and the non-linear effects do take place, which can be observed in figure 6.3. The steady-state values of the normalized superficial velocities, $\langle \mathbf{u}(t) \rangle_{\text{s}} / \left(p_x \cdot \frac{K}{\mu} \right)$, for all non-linear flows, will be smaller than 1, because of the non-linear effects which are usually modelled by the Forchheimer correction term. And we can see that the larger the steady-state pore Reynolds numbers, Re_{pore}, are, the smaller the

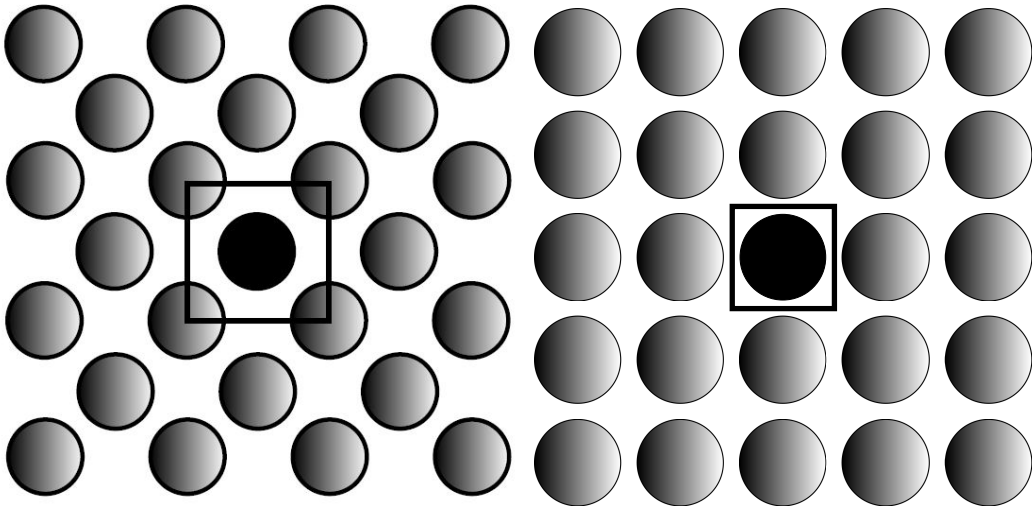

Figure 6.1: Geometries of the simulations performed. Arrangement of two-dimensional staggered cylinders and the computational box containing the cylinders (a), and arrangement of three-dimensional spheres arranged on a uniform grid (b).

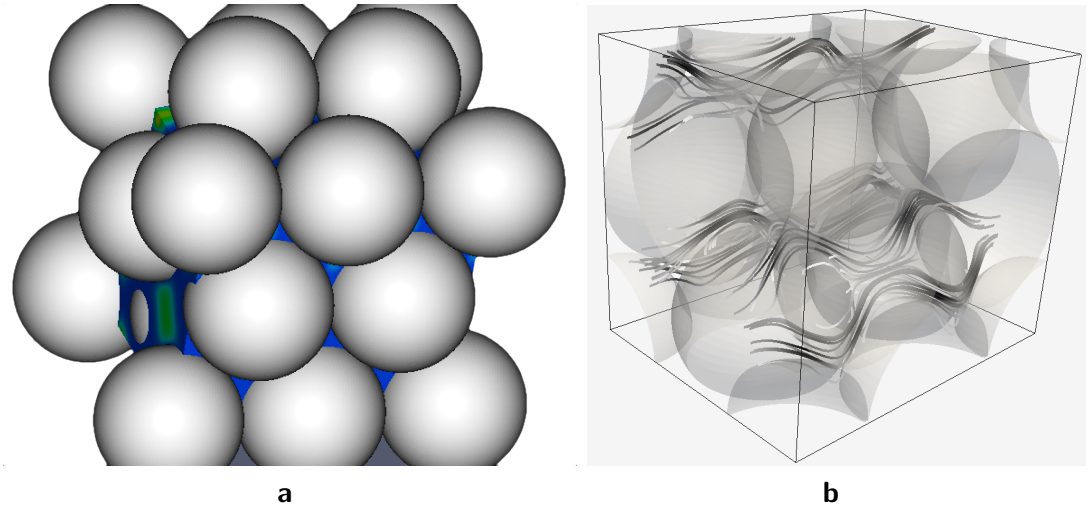

Figure 6.2: Three-dimensional simulation of a dense sphere pack. Arrangement of spheres (3D) (a) and streamlines (b).

values of the steady-state normalized superficial velocities become. In the case of 3D dense sphere pack, e.g., the steady-state normalized superficial velocity is less than 0.6, when the steady-state pore Reynolds number is larger than 60.
We further plot the gaps between the non-linear curves and the linear curves, i.e., the deviations, $\sigma_u(t)$, for each case in figure 6.4. Note that in figure 6.4 $\sigma_u(t)$ is normalized by their steady-state values, $\sigma_{u,\mathrm{ss}}$. At some instants, $\sigma_u(t)$ increases to a certain value which can no longer be ignored, and these instants can be regarded as those at which the non-linear effects set in. We further investigate this issue in the next sections.

6.1.4 The onset against the instantaneous pore Reynolds number

We first recall the expression of the pore Reynolds number in this section. We define an instantaneous pore Reynolds number

$$Re_{\mathrm{pore}}(t) = \frac{|\langle \boldsymbol{u}(t)\rangle_{\mathrm{s}}|d}{\nu} \tag{6.6}$$

where $|\langle \boldsymbol{u}(t)\rangle_{\mathrm{s}}|$ is the magnitude of the instantaneous superficial velocity, d is the pore/grain size and ν is the kinematic viscosity. Note that we have different purposes of defining the instantaneous Reynolds number and the steady-state Reynolds number. We assess the influence of the instantaneous pore Reynolds number, $Re_{\mathrm{pore}}(t)$, on the onset of the non-linear effects, and we defined the steady-state pore Reynolds number, $Re_{\mathrm{pore,ss}}$, in equation (6.1) to reflect the order of magnitude of the prescribed pressure gradient.
For steady porous-media flows, the steady-state pore Reynolds number, $Re_{\mathrm{pore,ss}}$, is taken as the dominating variable that determines the onset of the non-linear effects, i.e., when $Re_{\mathrm{pore,ss}} > 1$, the non-linear effects set in. In this section, we investigate if this is still the case in unsteady porous-media flows, with the instantaneous pore Reynolds number, $Re_{\mathrm{pore}}(t)$.
As discussed in section 6.1.3, in figure 6.3, the instants at which the non-linear curves deviate from the linear curves define the onset of the non-linear effects in unsteady porous-media flows. Such a deviation, which can also be understood as the gap between the non-linear curves and the linear curves in figure 6.3, can also be mathematically expressed by σ_u in equation (6.5). We plot $\sigma_u(t)$ with respect to the instantaneous pore Reynolds number $Re_{\mathrm{pore}}(t)$, for different steady-state pore Reynolds numbers, $Re_{\mathrm{pore,ss}}$, in figure 6.5 (a), (b) and (c).
From figure 6.5 (a), (b) and (c), we can clearly observe that, in all the three cases, for a certain value of σ_u, the corresponding values of $Re_{\mathrm{pore}}(t)$ fall in very wide ranges. To further specify this, we plotted figure 6.5 (d), in which the values of the instantaneous pore Reynolds number, $Re_{\mathrm{pore}}(t)$, which are measured in figure 6.5, (a), (b) and (c) at $\sigma_u = 5\%$, are plotted against different steady-state pore Reynolds numbers, $Re_{\mathrm{pore,ss}}$. For the 2D cylinder array and 3D dense sphere pack, one can clearly identify that $Re_{\mathrm{pore}}(t)$ at $\sigma_u = 5\%$ is almost linear to $Re_{\mathrm{pore,ss}}$. For the 3D sphere array, it is linear at small steady-state pore Reynolds numbers, and become non-linear at larger Reynolds numbers. The slopes are relatively high (0.61 for cylinder array, 0.43 for sphere array and 0.758 for dense sphere pack). This means that,

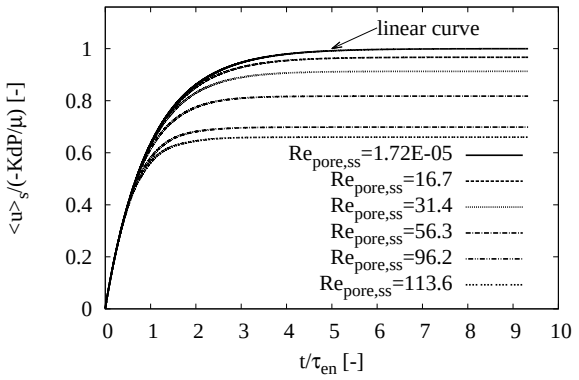

a: cylinder array

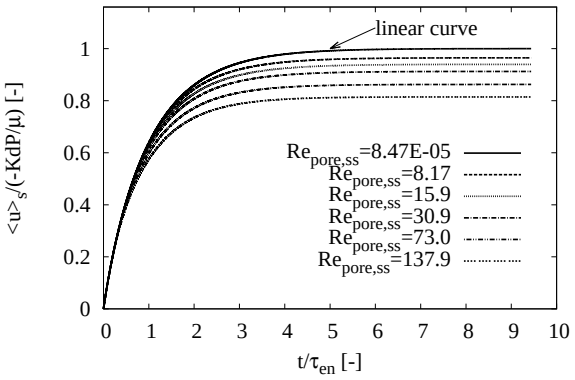

b: sphere array

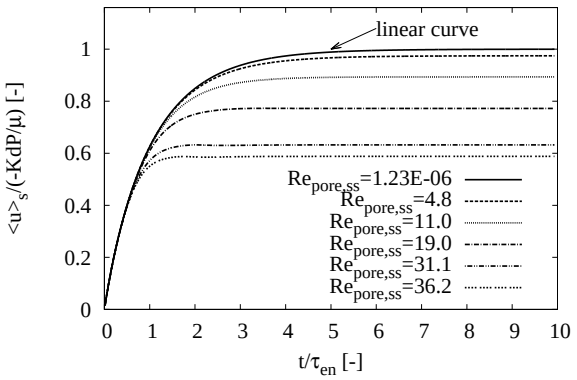

c: dense sphere pack

Figure 6.3: Development of the normalized superficial velocity with respect to time in a two-dimensional cylinder array (a), in a three-dimensional sphere array (b), and in a three-dimensional dense sphere pack (c).

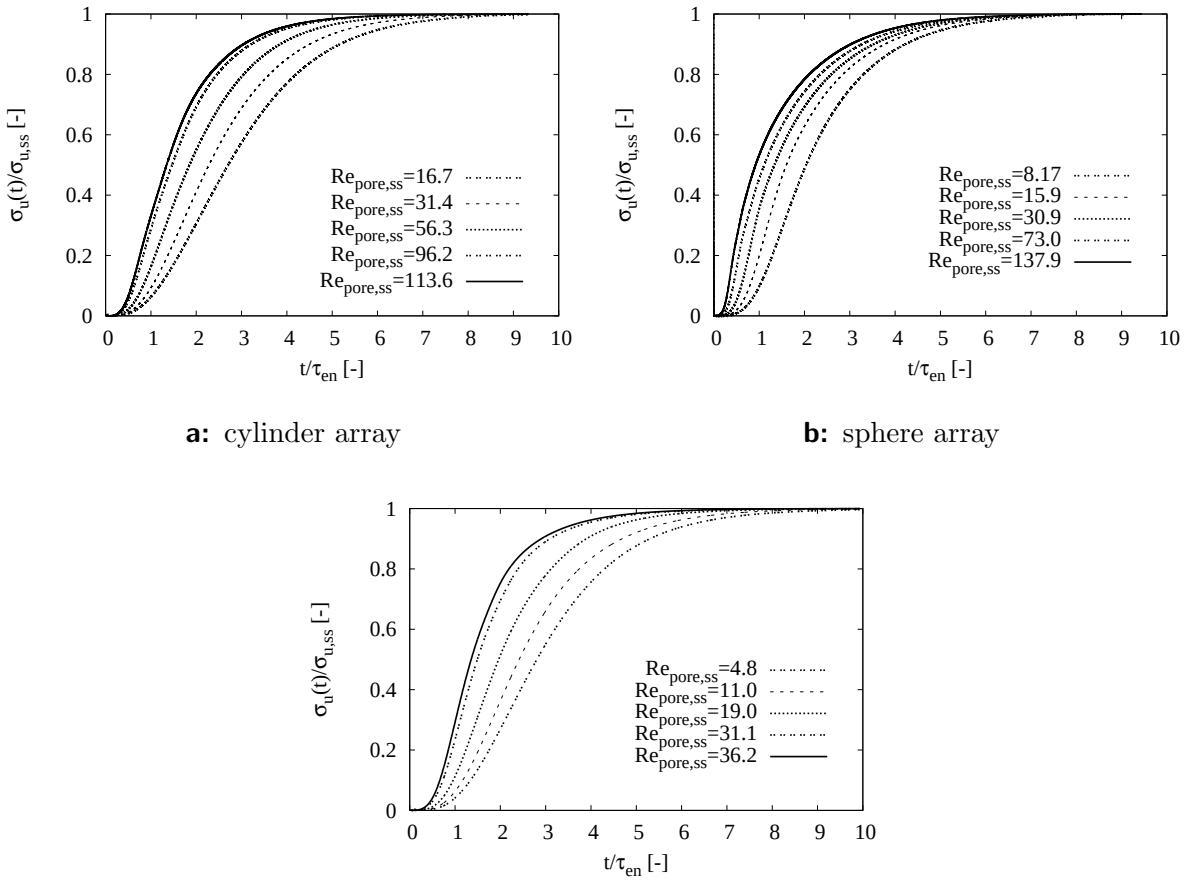

a: cylinder array

b: sphere array

c: dense sphere pack

Figure 6.4: Development of the normalized relative deviation, $\sigma_u(t)/\sigma_{u,\mathrm{ss}}$, with respect to time, in a two-dimensional cylinder array (a), in a three-dimensional sphere array (b), and in a three-dimensional dense sphere pack (c).

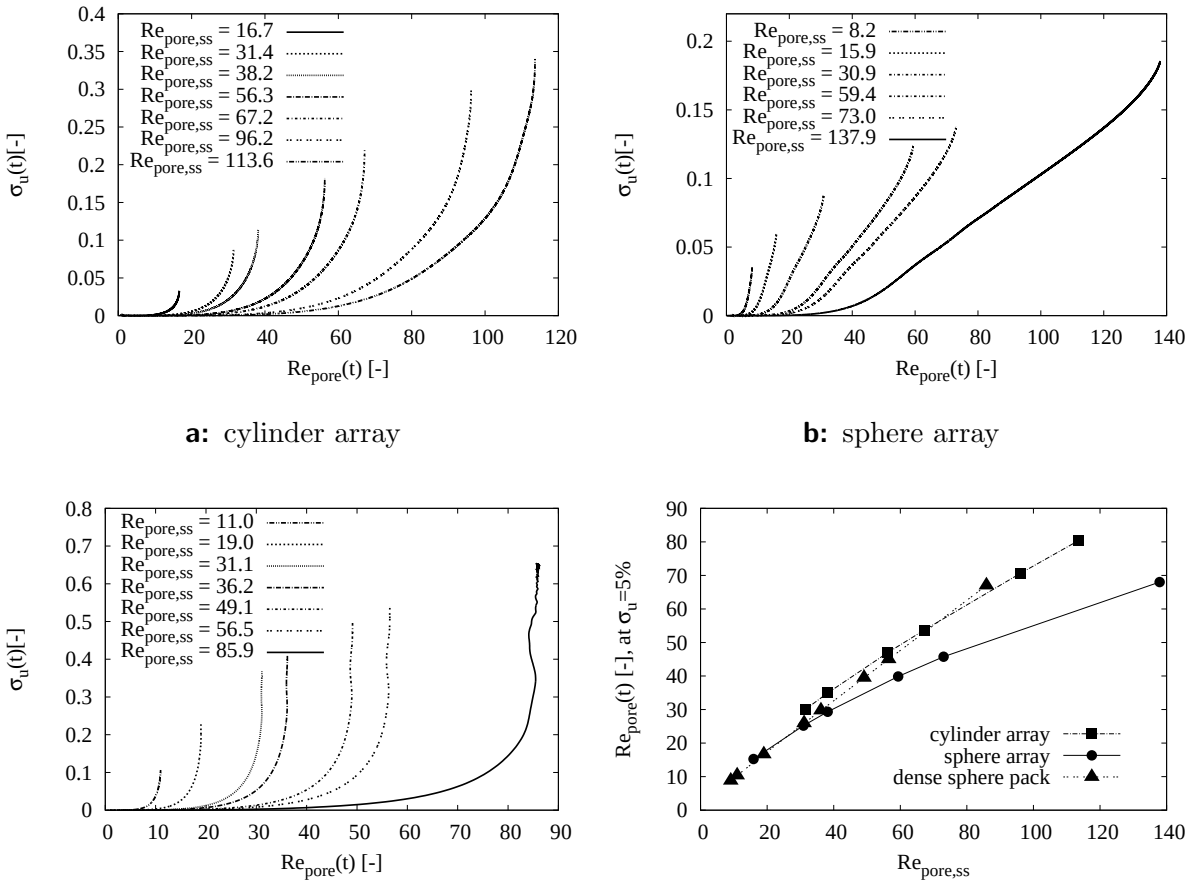

Figure 6.5: Relative deviation of the non-linear curves from the linear curves, σ_u, with respect to the instantaneous pore Reynolds number, $Re_{\mathrm{pore}}(t)$, in a two-dimensional cylinder array (a), in a three-dimensional sphere array (b), and in a three-dimensional dense sphere pack (c); and the values of the instantaneous pore Reynolds number, $Re_{\mathrm{pore}}(t)$, when the relative deviation is $\sigma_u = 5\%$, against different steady-state pore Reynolds numbers, $Re_{\mathrm{pore,ss}}$, for different flow cases (d).

when the prescribed pressure gradient, $\boldsymbol{\nabla}\langle p\rangle_{\mathrm{i}}$, (or the resulting steady-state pore Reynolds number, $Re_{\mathrm{pore,ss}}$) varies dramatically, the value of the instantaneous pore Reynolds number, $Re_{\mathrm{pore}}(t)$, at $\sigma_u = 5\%$ also varies dramatically. This essentially means that the instantaneous pore Reynolds number, $Re_{\mathrm{pore}}(t)$, cannot be used to benchmark the onset of the non-linear effects in the same way as the steady-state pore Reynolds number in steady porous-media flows.

6.1.5 The onset against the instantaneous Stokes Reynolds number

The instantaneous Stokes Reynolds number is defined as

$$Re_{\mathrm{Stokes}}(t) = \frac{|\langle \boldsymbol{u}\rangle_{\mathrm{s}}(t)|\sqrt{2\nu t}}{\nu}, \tag{6.7}$$

where $|\langle \boldsymbol{u}\rangle_{\mathrm{s}}(t)|$ is the magnitude of the instantaneous superficial velocity, ν is the kinematic viscosity, t is the time since the development of the fluid and $\sqrt{2\nu t}$ is the so-called Stokes boundary layer thickness. Note that in oscillatory channel and boundary layer flows, flow states have been found to depend on the Stokes Reynolds number. Different regimes have been identified (e.g. Hino et al., 1976; Akhavan et al., 1991), depending on the value of $Re_{\mathrm{Stokes}}(t)$. Laminar flow has been observed for $Re_{\mathrm{Stokes}}(t) < 100$. In the regime of $100 < Re_{\mathrm{Stokes}}(t) < 550$, denoted as *disturbed laminar flow*, the flow deviates from the laminar one in the acceleration phase. In our context, this would be denoted as *non-linear flow*. In this section, we assess this Reynolds number in unsteady porous-media flows.

Analogy to section 6.1.4, we plot the relative deviation of the non-linear curves from the linear curves, $\sigma_u(t)$, against the Stokes Reynolds number, $Re_{\mathrm{Stokes}}(t)$, in figure 6.6 (a), (b) and (c).

We observe that in figure 6.6 (a), (b) and (c), in all cases, for a certain value of σ_u, the variations in $Re_{\mathrm{Stokes}}(t)$ for different curves fall in much smaller ranges, compared to those in figure 6.5. We further plot figure 6.6, (d), in which the values of the instantaneous Stokes Reynolds number, $Re_{\mathrm{Stokes}}(t)$, which are measured in figure 6.6, (a), (b) and (c), at $\sigma_u = 5\%$, are plotted against different steady-state pore Reynolds numbers, $Re_{\mathrm{pore,ss}}$. For the 2D cylinder array and 3D dense sphere pack, $Re_{\mathrm{Stokes}}(t)$ at $\sigma_u = 5\%$ is almost linear to $Re_{\mathrm{pore,ss}}$; for the 3D sphere array, it is linear at smaller steady-state pore Reynolds numbers, and is non-linear at larger Reynolds numbers. The slopes are much smaller than those in figure 6.5, (d) (0.023 for cylinder array, 0.053 for sphere array and 0.018 for dense sphere pack). This means that, when the prescribed pressure gradient, $\boldsymbol{\nabla}\langle p\rangle_{\mathrm{i}}$, (or the resulting steady-state pore Reynolds number, $Re_{\mathrm{pore,ss}}$) varies dramatically, the value of the instantaneous Stokes Reynolds number, $Re_{\mathrm{Stokes}}(t)$, at $\sigma_u = 5\%$ does not vary much. This essentially means that the instantaneous pore Reynolds number, $Re_{\mathrm{pore}}(t)$, can be used to benchmark the onset of the non-linear effects in the same way as the steady-state pore Reynolds number in steady porous-media flows.

This numerical experiment clearly indicates that, compared to the pore Reynolds number, Re_{pore}, the Stokes Reynolds number, Re_{Stokes}, can be used to determine the onset of the non-

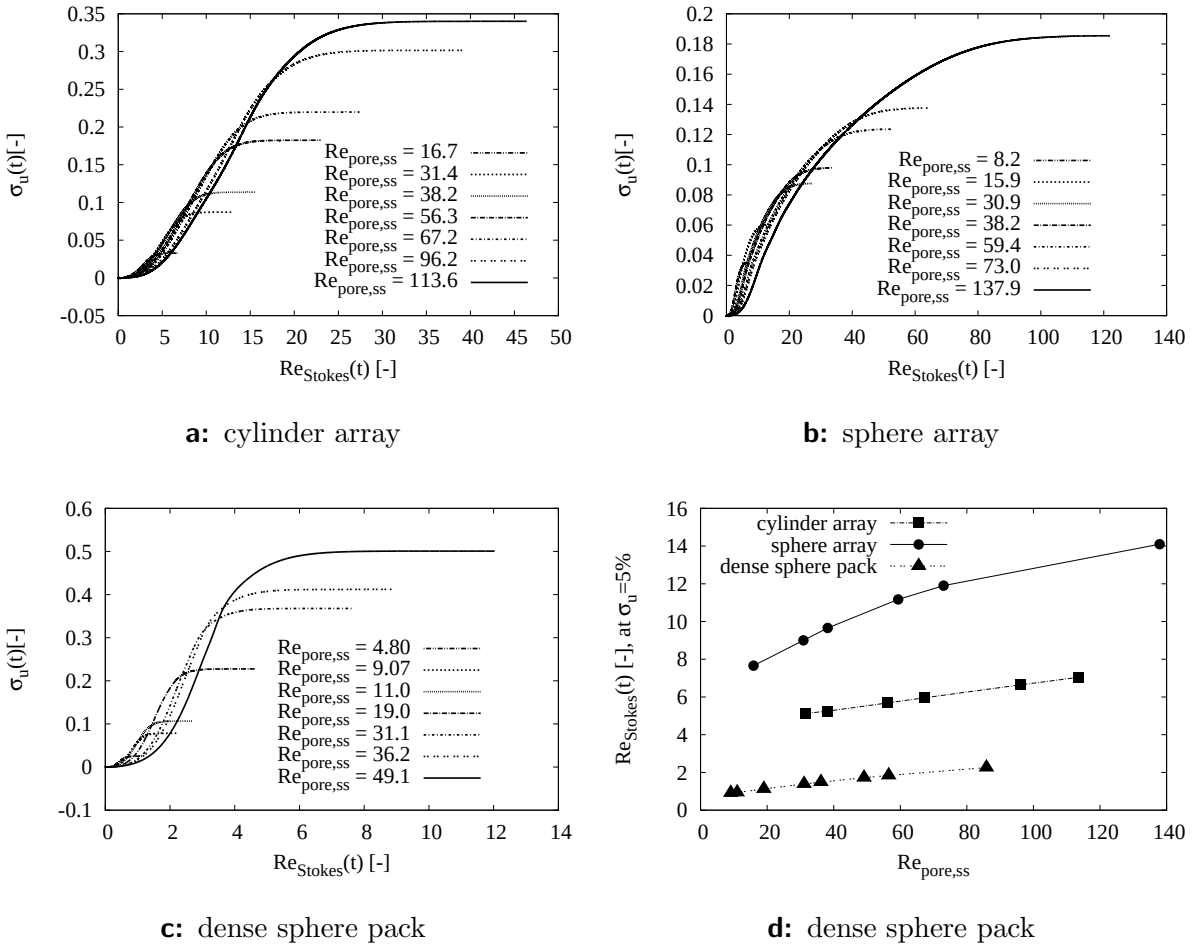

a: cylinder array

b: sphere array

c: dense sphere pack

d: dense sphere pack

Figure 6.6: Relative deviation of the non-linear curves from the linear curves, σ_u, with respect to the instantaneous Stokes Reynolds number, in a two-dimensional cylinder array (a), in a three-dimensional sphere array (b), and in a three-dimensional dense sphere pack (c); and the values of the instantaneous Stokes Reynolds number, $Re_{\mathrm{Stokes}}(t)$, when the deviation is $\sigma_u = 5\%$, against different steady-state pore Reynolds numbers, $Re_{\mathrm{pore,ss}}$, for different flow cases (d).

linear effects in unsteady porous-media flows more accurately.

6.2 The Unsteady Forchheimer Equation

We recall the unsteady Forchheimer equation:

$$\boldsymbol{\nabla}\langle p\rangle_{\mathrm{i}} = a\langle \boldsymbol{u}\rangle_{\mathrm{s}} + b\langle \boldsymbol{u}\rangle_{\mathrm{s}}^2 + c\frac{\partial\langle \boldsymbol{u}\rangle_{\mathrm{s}}}{\partial t}, \tag{6.8}$$

As already discussed in section 2.3.1, the applicability of the unsteady Forchheimer equation (6.8) with constant coefficients, a, b and c, has not yet been assessed. This means that, we do not know if the unsteady Forchheimer equation (6.8) with constant coefficients can be used to describe unsteady and non-linear porous-media flows on a macroscopic level. In this section, we aim to answer this question.

Solving equation (6.8) analytically by hand is obviously difficult, as it contains both the time derivative and a quadratic term of the superficial velocity, $\langle \boldsymbol{u}\rangle_{\mathrm{s}}$. However, when we assume constant coefficients, a, b and c, we might be able to use mathematical software tools such as Matlab to solve this equation. By comparing the Matlab solutions to the DNS results, we can easily assess the applicability of the unsteady Forchheimer equation (6.8) with constant coefficients. In this section, we consider the Direct Numerical Simulations already conducted in section 6.1, thus we only have to obtain the Matlab solutions of equation (6.8) for the benchmark problem in section 6.1.1.

In order to obtain the Matlab solutions, we must first fix the values of the parameters a, b and c, for the 2D cylinder array, the 3D sphere array and the 3D dense sphere pack. From chapters 4 and 5, we already know that, $a = -\mu/K_D$ and $c = a\tau$, where $\tau = \frac{K_{\mathrm{D}}}{\nu}\frac{\langle \boldsymbol{u}\cdot\boldsymbol{u}\rangle_{\mathrm{s}}}{\langle \boldsymbol{u}\rangle_{\mathrm{s}}\cdot\langle \boldsymbol{u}\rangle_{\mathrm{s}}}$, are accurate for unsteady and linear flows. It is reasonable to assume here that a and c have the same value in non-linear regimes as well, because of two reasons: (I) in figure 6.3, at the beginning of the flow development, all the non-linear curves lie on top of the linear curves, which means that at the beginning of the flow development, all flows are in the linear regime, and this simply means that $a = -\mu/K_D$ and $c = a\tau = \rho\frac{\langle \boldsymbol{u}\cdot\boldsymbol{u}\rangle_{\mathrm{s}}}{\langle \boldsymbol{u}\rangle_{\mathrm{s}}\cdot\langle \boldsymbol{u}\rangle_{\mathrm{s}}}$ applies at those instants. (II) we assume that a and c in equation (6.8) remain constant during the whole flow development process.

Now we only have to determine the parameter b. As we assume that b in equation (6.8) remains constant during the whole flow development process, the value of b can be easily obtained from equation (6.8) for the steady-state, where the time derivative term is zero, and the values of $\boldsymbol{\nabla}\langle p\rangle_{\mathrm{i}}$, a and $\langle \boldsymbol{u}\rangle_{\mathrm{s}}$ in the steady-state are all known from the numerical experiments. Another interesting point is whether b is dependent on the prescribed pressure gradient for a certain medium. Theoretically, b shall be a constant only depending on the density of the fluid and the geometry of the medium (e.g. Lasseux et al., 2011), and thus it is independent of the pressure gradient. We give an example here in the literature, which is the experiment conducted by Bağci et al. (2014), investigating flow through small sphere packs. Their results suggested that for steady flows, b is independent of the pressure gradient. We simply

give the values of b from the DNS simulations in table 6.1.

Table 6.1: Values of b under various $Re_{\text{pore,ss}}$, in 2D cylinder array and 3D dense sphere pack.

2D cylinder array	3D dense sphere pack
9.51 ($Re_{\text{pore,ss}} = 56.3$)	31.01 ($Re_{\text{pore,ss}} = 19.0$)
10.77 ($Re_{\text{pore,ss}} = 96.2$)	37.41 ($Re_{\text{pore,ss}} = 31.1$)
10.88 ($Re_{\text{pore,ss}} = 113.6$)	38.74 ($Re_{\text{pore,ss}} = 36.2$)

The values in table 6.1 for different cases do not vary a lot with respect to the steady-state pore Reynolds number, $Re_{\text{pore,ss}}$ (or the prescribed pressure gradient, $\boldsymbol{\nabla}\langle p\rangle_{\text{i}}$), which is basically consistent with theory.
With the parameters a, b and c all determined, it is easy to program in Matlab and solve equation (6.8) directly. We discuss the solutions and the comparison of such solutions to the DNS results in section 6.2.1.

6.2.1 Numerical Results

In the Matlab code, a Runger-Kutta third order time integration scheme has been applied, and equation (6.8) has been solved with very fine time steps, which were kept the same as in the DNS.
We plot the development of the normalized superficial velocity with respect to time in a two-dimensional cylinder array, and compare the DNS results (symbols) with the Matlab solutions (lines), in figure 6.7 (a). The linear curves solved by Matlab match the DNS results very well, and this is in line with our research results in Chapters 4 and 5, i.e., the unsteady Darcy equation with constant coefficients can describe unsteady porous-media flows accurately, within low and medium frequencies. While for the non-linear curves, the first parts of the curves (when the flows are still in the linear regime) and the steady-state parts match the DNS results. In the middle, at the instants right before the non-linear effects set in ($1 < t/\tau_{\text{en}} < 2$), the DNS results have a small amount of overshoots, and this cannot be presented by the Matlab solutions of the unsteady Forchheimer equation (6.8) with constant coefficients.
The relative error (difference) between the DNS result and Matlab solutions, which is $1 - \frac{\langle \mathbf{u}(t)\rangle_{\text{s}}/\left(p_x \cdot \frac{K}{\mu}\right)|_{\text{Matlab}}}{\langle \mathbf{u}(t)\rangle_{\text{s}}/\left(p_x \cdot \frac{K}{\mu}\right)|_{\text{DNS}}}$, for the cylinder array, is then plotted in figure 6.7 (b). It is not surprising that the errors obtain the maximum values right after the flows started to develop, as all the numerical values are very small at those moments. The errors representing the aforementioned overshoots, are all less than 5%. At steady states, the errors simply vanish.
We now plot the development of the normalized superficial velocity with respect to time in a three-dimensional dense sphere pack, and compare the DNS results (symbols) with the Matlab solutions (lines), in figure 6.8 (a). The overshoots also mostly take place at $(1 < t/\tau_{\text{en}} < 2)$, and in this case they are even larger.
The relative error (difference) between the DNS result and Matlab solutions for the dense sphere pack is then plotted in figure 6.8 (b). The errors representing the aforementioned

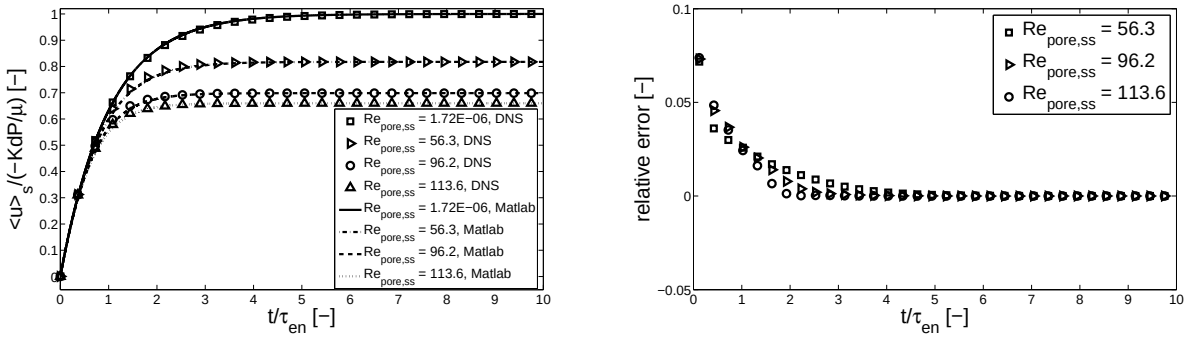

a: superficial velocity w.r.t. time **b:** relative error w.r.t. time

Figure 6.7: (a): development of the normalized superficial velocity with respect to time in a two-dimensional cylinder array, DNS results (symbols) in comparison with Matlab solutions (lines). (b): the relative error between Matlab solutions and DNS results, for the two-dimensional cylinder array.

Figure 6.8: (a): development of the normalized superficial velocity with respect to time in a three-dimensional dense sphere pack, DNS results (symbols) in comparison with Matlab solutions (lines). (b): the relative error between Matlab solutions and DNS results, for the three-dimensional dense sphere pack.

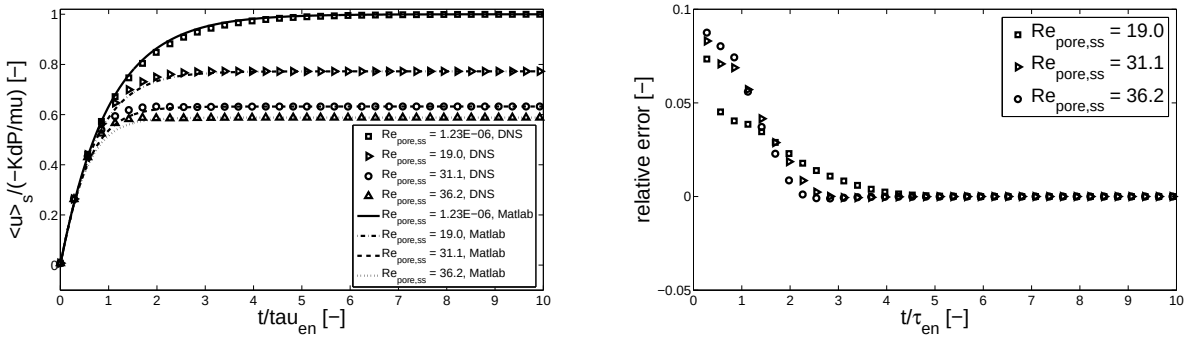

a: superficial velocity w.r.t. time **b:** relative error w.r.t. time

overshoots, are slightly larger, but they are all less than 7% (when $1 < t/\tau_{\text{en}} < 2$). At steady states, the errors also vanish.

6.3 Conlusions

In this part, we focus on unsteady and non-linear porous-media flows. We aim to investigate the physical variable that determines the onset of the non-linear effects, and assess whether the unsteady Forchheimer equation with constant coefficients can be used to describe the flow on the macro scale. We set up a benchmark problem, in which a prescribed constant pressure gradient is defined to drive the flow. We calculate the deviation of the normalized superficial velocity for non-linear flows from those for the linear flows to describe the onset. We use fully resolved *direct numerical simulation (DNS)* of the flow in the pore space to assess the aforementioned two questions. Our DNS results have shown that the Stoke Reynolds number, instead of the pore Reynolds number, can be used to determine the onset of the non-linear effects in unsteady porous-media flows more accurately.

At the instants right before the steady state, the superficial velocities obtained from DNS show certain overshooting behaviours, which is not represented by simple solutions of the unsteady Forchheimer equation. However, the relative errors between this solution and the DNS results are within 5% for the 2D cylinder array and 7% for the 3D dense sphere pack.

7 Conclusions and outlook

This PhD thesis mainly focuses on unsteady porous-media flows, which can be further classified into linear an non-linear flows.

For unsteady and linear porous-media flows, the behavior of the unsteady Darcy equation with constant coefficients was studied. Homogeneous and isotropic medium was assumed, and the time scale was derived in different ways: by consistent volume-averaging of the Navier-Stokes (VANS) equations together with a steady-state closure, or a virtual mass closure, for the interaction term; or by volume-averaging the equation for the kinetic energy, together with a closure for the kinetic energy dissipation, which was approximated by its steady-state value using the classical permeability. The time scale obtained from the energy approach is different from the one obtained from the VANS approach together with a steady-state closure, and there is a factor between them. This factor is proportional to the ratio of the integrated kinetic energy in the pore space to that of the intrinsic velocity. The direct numerical simulations have shown that the time scale obtained from the volume-averaged Navier-Stokes system with a steady-state closure for the interaction term underestimates the true value, and this is because the steady-state closure is not accurate in unsteady flows. However, the closure for the kinetic energy dissipation in the energy approach is well-suited in all of the numerical simulations, and the time scale obtained from the energy approach matches the direct numerical simulation results very well. Note that the ratio between these time scales can be very large, it is 1.2 for plain channel flow and 2.75 for a dense sphere pack. In general, our direct numerical simulations supported the use of the unsteady form of Darcy's equation with constant coefficients to describe the flows on the macroscopic scale.

This research was then extended into unsteady and linear porous-media flows driven by an oscillatory (sinusoidal) pressure gradient, and the analytical solutions of the unsteady Darcy equation were assessed, which consist of the aforementioned two different time scales. These analytical solutions were compared with the analytical solutions of laminar oscillatory pipe and channel flows, and they comply well with each other, if the proper time scale is chosen. In this analysis it was also found that, the ratio of the kinetic energy in the pore space to the kinetic energy of the superficial velocity plays a significant role when considering a large range of frequencies. At low frequencies up to $\omega K_D/(\nu\epsilon) \approx 2.5$, instantaneous velocity profiles tend to assume a parabolic shape, and the time-scale ratio remains a constant equal to that in the steady state. At larger frequencies, the time-scale ratio goes towards unity as the viscous layer tends towards zero and the velocity profiles flatten. This would infer different time scales for small and large frequencies. Direct numerical simulations of oscillatory flow through a 2D cylinder array and a 3D dense sphere pack were then conducted to assess our theory, and they revealed very similar results. In general, this study supported that the unsteady Darcy equation is able to predict the amplitude damping and phase lag accurately on the macroscopic scale, provided, the proper time scale is chosen.

For unsteady and non-linear porous-media flows, the physical variable that determines the instants at which the non-linear effects set in was looked for, and the applicability of the unsteady Forchheimer equation with constant coefficients was investigated. A benchmark problem was considered, in which a prescribed constant pressure gradient is defined to drive the flow. A mathematical expression to describe the onset of the non-linear effects was then derived, and direct numerical simulations with various complexities were conducted to assess it. The simulation results show that at the instants at which the non-linear effects set in, the values of the instantaneous pore Reynolds number based on the pore scale are in a very wide range, when the prescribed pressure gradients are with various orders of magnitude. However, for the instantaneous Stokes Reynolds number based on the Stokes boundary layer thickness, this range is much smaller, concluding, the instantaneous Stokes Reynolds number can be used to determine the onset of the non-linear effects in unsteady porous-media flows more accurately than the instantaneous pore Reynolds number. As for the solution of the unsteady Forchheimer equation, it cannot represent the overshoot of the superficial velocity, which is obtained in DNS for a 2D cylinder array and a 3D dense sphere pack when the steady-state pore Reynolds number is big enough. However, the relative errors between this solution and the DNS results are within 5% for the cylinder array and 7% for the dense sphere pack.

Note that most of the theoretical derivations in this PhD thesis, as well as all the numerical simulations, consider only homogeneous and isotropic mediums. For inhomogeneous and anisotropic, more work still needs to be done. Moreover, the main reason of the overshoot of the superficial velocity in Chapter 6 still remains a question, and a mathematical function which can model this overshoot accurately is required. A further research can be carried out to investigate the onset of the non-linear effects in oscillatory flows, and one can try to model the oscillatory and non-linear flows. With one step further, one can also investigate the onset of turbulent effects and describe REV-based flow quantities such as interaction term, dissipation and production of turbulent kinetic energy in transient and oscillatory flow through porous media.

Bibliography

N. Ahmed and D. K. Sunada. Non linear flow in porous media. *J. Hydraul. Div., Proc. ASCE*, 95:1847–1857, 1969.

R. Akhavan, R. Kamm, and A. Shapiro. An investigation of transition to turbulence in bounded oscillatory Stokes flows Part 1. Experiments. *J. Fluid Mech.*, 225:395–422, 1991.

M. R. Albert and E. F. Shultz. Snow and firn properties and air-snow transport processes at summit, greenland. *Atmospheric Environment*, 36:2789–2797, 2002.

O. Andersen, M. V. Gent, J. V. der Meer, H. Burcharth, and H. D. Adel. Non-steady oscillatory flow in coarse granular materials. In *Proceedings of Final Overall Workshop of MAST G6-S Coastal Structures*. HR Wallingford, 1993.

T. B. Anderson and R. Jackson. A fluid mechanical description of fluidized beds. *Ind. Eng. Chem. Fundam.*, 6:527–538, 1967.

M. Balhoff, A. Mikelic, and M. F. Wheeler. Polynomial filtration laws for low reynolds number flows through porous media. *Transport in Porous Media*, 81:35–60, 2010.

J. Barrère. *Modélisation des Écoulement de Stokes et de Navier-Stokes en Milieu Poreux*. PhD thesis, University of Bordeaux, 1990.

G. K. Batchelor. *An introduction to fluid dynamics*. Cambridge University Press., 1967.

Ö. Bağci, N. Dukhan, and M. Özdemir. Flow regimes in packed beds of spheres from pre-darcy to turbulent. *Transport in Porous Media*, 104(3):501–520, 2014. ISSN 0169-3913. doi: 10.1007/s11242-014-0345-0. URL `http://dx.doi.org/10.1007/s11242-014-0345-0`.

J. Bear. *Dynamics of Fluids in Porous Media*. Elsevier, 1972.

R. B. Bird, W. E. Strewart, and E. N. Lightfoot. *Transport Phenomena*. John Wiley, 2002.

E. F. Blick. Capillary orifice model for high speed flow through porous media. *I&EC, Process Design And Development*, 1:90–94, 1966.

D. R. Bowling and W. J. Massman. Persistent wind-induced enhancement of diffusive CO2 transport in a mountain forest snowpack. *J. of Geophysical Research*, 116(1):G04006, 2011. doi: 10.1029/2011JG001722.

M. Breuer, N. Peller, C. Rapp, and M. Manhart. Flow over periodic hills – numerical and experimental study over a wide range of Reynolds numbers. *Computers and Fluids*, 38(2): 433–457, February 2009.

W. P. Breugem, B. J. Boersma, and R. E. Uittenbogaard. The influence of wall permeability on turbulent channel flow. *J. Fluid Mech.*, 562:35–72, 2006. URL `http://www.knmi.nl/publications/fulltexts/jfmsept2006.pdf`.

H. F. Burcharth and O. H. Andersen. On the one-dimensional steady and unsteady porous flow equations. *Coastal Engineering*, 24:233–257, 1995.

G. Cerri, A. Giovannelli, L. Battisti, and R. Fedrizzi. Advances in effusive cooling techniques of gas turbines. *Applied Thermal Engineering*, 27:692–698, 2007.

G. Chauveteau. *Essai sur la loi de Darcy.* PhD thesis, Université de Toulouse, 1965.

Z. Chen, S. L. Lyons, and G. Qin. Derivation of the forchheimer law via homogenization. *Transport in Porous Media*, 44:325–335, 2001.

D. Cornell and L. K. Katz. Flow of gases through consolidated porous media. *Ind. Eng. Chem.*, 45, 1951.

O. Coulaud, P. Morel, and J. P. Catagirone. Numerical modelling of nonlinear effects in laminar flow through a porous medium. *Journal of Fluid Mechanics*, 190:393–407, 1988.

V. D. Cvetkovic. A continuum approach to high velocity flow in a porous medium. *Transport in Porous Media*, 1:63–97, 1986.

W. Dahmen, T. Gotzen, and S. Müller. Numerical Simulation of Transpiration Cooling through Porous Material. 2013.

H. Darcy. Recherches expérimentales relatives au mouvement de l'eau dans les tuyaux. *Mallet-Bachelier, Paris*, 1856.

G. D'Errico, G. Ferrari, and A. Onorati. Numerical Modeling of Unsteady Reacting Flows in the Exhaust System of a S.I. Engine Including the Catalytic Converter. In *Seoul 2000 FISITA World Automotive Congress*, 2000.

F. A. L. Dullien and M. I. S. Azzam. Flow rate-pressure gradient measurement in periodically nonuniform capillary tubes. *AIChE Journal*, 19:222–229, 1973.

A. Dybbs and R. V. Edwards. In J. Bear and M. Y. Corapcioglu, editors, *Fundamentals of Transport Processes in Porous Media*, pages 201–256, Nijhoff, Dordrecht.

S. Ergun. Fluid flow through packed columns. *Chemical Engineering Progress*, 48:89–94, 1952.

V. S. Ermolaev, K. O. Gryaznov, E. B. Mitberg, V. Z. Mordkovich, and V. F. Tretyakov. Laboratory and pilot plant fixed-bed reactors for fischer-tropsch synthesis: mathematical modeling an experimental investigation. *Chemical Engineering Science*, 2015. URL `http://dx.doi.org/10.1016/j.ces.2015.07.036`.

J. Fan and L. Wang. Analytical theory of bioheat transport. *Journal of Applied Physics*, 109:104702, 2011.

J. Finnigan. Turbulence in plant canopies. *Annu. Rev. Fluid Mech.*, 44(1):479–504, 2000.

M. Firdaouss, J. L. Guermond, and P. L. Quéré. Nonlinear corrections to darcy's law at low reynolds numbers. *J . Fluid Mech.*, 343:331–350, 1997.

P. Forchheimer. Wasserbewegung durch Boden. *Z. Ver. Deutsch. Ing*, 45:1782–1788, 1901.

M. Fourar, G. Radilla, R. Lenormand, and C. Moyne. On the non-linear behavior of a laminar single-phase flow through two and three-dimensional porous media mostafa. *Advances in Water Resources*, 27:669–677, 2004.

J. D. Fuentes, M. Lerdau, R. Atkinson, D. Baldocchi, J. W. Bottenheim, P. Ciccioli, B. Lamb, C. Geron, L. Gu, A. Guenther, T. D. Sharkey, and W. Stockwell. Biogenic hydrocarbons in the atmospheric boundary layer: A review. *Bull. Am. Meteorol. Soc.*, 81:1537–1575, 2000.

C. K. Ghaddar. On the permeability of unidirectional fibrous media: A parallel computational approach. *Physics of Fluids*, 7:2563–2586, 1995.

T. Giorgi. Derivation of the forchheimer law via matched asymptotic expansions. *Transport in Porous Media*, 29:191–206, 1997.

W. G. Gray and K. O'Neill. On the general equations for flow in porous media and their reduction to darcys law. *Water Resour. Res.*, 12:148–154, 1976.

L. Green and P. Duwez. Fluid flow through porous metals. *J. Appl. Mech.*, 18, 1951.

Z. Gu and H. Wang. Gravity waves over porous bottoms. *Coastal engineering*, 15(5):497–524, 1991.

A. Guenther, T. Karl, P. Harley, C. Wiedinmyer, P. I. Palmer, and C. Geron. Estimates of global terrestrial isoprene emissions using megan (model of emissions of gases and aerosols from nature). *Atmos. Chems. Phys.*, 6:3181–3210, 2006.

K. Habibi, A. Mosahebi, and H. Shokouhmand. Heat transfer characteristics of reciprocating flows in channels partially filled with porous medium. *Transport in porous media*, 89(2): 139–153, 2011.

K. R. Hall, G. M. Smith, and D. J. Turcke. Comparison of oscillatory and stationary flow through porous media. *Coastal Engineering*, 24:217–232, 1995.

A. A. Hannoura and J. A. McCorquodale. Virtual mass of coarse granular media. *J. Waterw. Port Coastal Ocean Div. ASCE*, 104:191–200, 1978.

S. M. Hassanizadeh and W. G. Gray. General conservation equations for multiphase systems: 1. averaging procedure. *Adv. Water Resour.*, 2:131–144, 1979.

S. M. Hassanizadeh and W. G. Gray. High velocity flow in porous media. *Transport in Porous Media*, 2:521–531, 1987.

A. Hazen. *The filtration of public water-supplies.* John Wiley, 1895.

A. A. Hill and B. Straughan. Poiseuille flow in a fluid overlying a porous medium. *J . Fluid Mech.*, 603:137–149, 2008.

R. J. Hill, D. L. Koch, and A. J. C. Ladd. The first effects of fluid inertia on flows in ordered and random arrays of spheres. *J. Fluid Mech.*, 448:213–241, 2001.

M. Hino, M. Sawamoto, and S. Takasu. Experiments on transition to turbulence in an oscillatory pipe flow. *J. Fluid Mech.*, 75:193–207, 1976.

A. Hokpunna and M. Manhart. Compact fourth-order finite volume method for numerical solutions of Navier-Stokes equations on staggered grids. *Journal of Computational Physics*, 229:7545–7570, 2010.

Z. Huang, Y. H. Zhu, P. X. Jiang, and Y. B. Xiong. Investigation of transpiration cooling with local thermal non-equilibrium model: Effects of different thermal boundary conditions at the porous-fluid interface. In *5th International Conference on Porous Media and its Applications in Science and Engineering*, 2014.

I. G. Hwang, C. Myung, S. Park, C. In, and G. K. Yeo. Theoretical and experimental flow analysis of exhaust manifolds for pzev. *SAE Paper 2007-01-3444*, 2007.

D. L. Jacono, F. Plouraboué, and A. Bergeon. Weak-inertial flow between two rough surfaces. *Physics of Fluids*, 17:063602, 2005.

A. R. A. Khaled and K. Vafai. The role of porous media in modeling flow and heat transfer in biological tissues. *International Journal of Heat and Mass Transfer*, 46:4989–5003, 2003.

D. L. Koch and A. J. C. Ladd. Moderate reynolds number flows through periodic and random arrays of aligned cylinders. *J . Fluid Mech.*, 349:31–66, 1997.

J. Kozeny. Über Kapillare Leitung des Wassers im Boden. *Sitzungsber Akad. Wiss., Wien*, 136(2a):271–306, 1927.

A. V. Kuznetsov and D. A. Nield. Forced convection with laminar pulsating flow in a saturated porous channel or tube. *Transport in Porous Media*, 65:505–523, 2006. ISSN 0169-3913. doi: 10.1007/s11242-006-6791-6. URL `http://dx.doi.org/10.1007/s11242-006-6791-6`.

D. Lasseux, A. A. A. Arani, and A. Ahmadi. On the stationary macroscopic inertial effects for one phase flow in ordered and disordered porous media. *Physics of Fluids*, 23, 2011.

L. M. Laushey and L. V. Popat. Darcy's law during unsteady flow. In L. J. Tison, editor, *Ground water: General assembly of Bern (Sep. 25–Oct. 7, 1967)*, volume 77, pages 284–299. International Union of Geodesy and Geophysics (IUGG) and International Association of Scientific Hydrology (IASH), 1968. URL `http://iahs.info/redbooks/a077/077028.pdf`.

K. M. Laxmi, V. R. Kumar, and Y. V. H. Rao. Modeling and simulation of gas flow velocity in catalytic converter with porous. *Engineering Research and Applications*, 3:518–522, 2013. ISSN 2248-9622.

C. Loudon and A. Tordesillas. The use of the dimensionless womersley number to characterize the unsteady nature of internal flow. *J. Theor. Biol.*, 191:63–78, 1998.

R. J. Lowe, J. R. Koseff, and S. G. Monismith. Oscillatory flow through submerged canopies: 1. velocity structure. *J. Geophys. Res*, 110:C10016, 2005.

R. J. Lowe, U. Shavit, J. L. Falter, J. R. Koseff, and M. S. G. Modeling flow in coral communities with and without waves: A synthesis of porous media and canopy flow approaches. *Limnology and Oceanography*, 53:2668–2680, 2008.

H. Ma and D. W. Ruth. The microscopic analysis of high forchheimer number flow in porous media. *Transport in Porous Media*, 13:139–160, 1993.

I. F. MacDonald, M. S. El-Sayed, K. Mow, and F. A. L. Dullien. Flow through porous media-the ergun equation revisited. *Ind. Eng. Chem.*, 18:199–208, 1979.

M. Maier, H. Schack-Kirchner, M. Aubinet, S. Goffin, B. Longdoz, and F. Parent. Turbulence effect on gas transport in three contrasting forest soils. *Soil Sci. Soc. Am. J.*, 76:1518–1528, 2011. doi: 10.2136/sssaj2011.0376.

M. Manhart. A zonal grid algorithm for DNS of turbulent boundary layers. *Computers and Fluids*, 33(3):435–461, March 2004.

C. M. Marle. Ecoulements monophasiques en milieu poreux. *Rev. Inst. Francais du Petrole*, pages 1471–1509, 1967.

S. Martínez-Martínez, R. D. Leal-Garza, F. A. Sánchez-Cruz, and E. B. Villarreal. Cfd analysis of the effect of the exhaust manifold design on the close-coupled catalytic converter performance. *Journal of KONES Powertrain and Transport*, 17:303–311, 2010.

A. Mazaheri, B. Zerai, G. Ahmadi, J. Kadambi, B. Saylor, M. Oliver, G. Bromhal, and D. Smith. Computer simulation of flow through a lattice flow-cell model. *Advances in Water Resources*, 28:1267–1279, 2005.

C. C. Mei and J.-L. Auriault. The effect of weak inertia on flow through a porous medium. *J . Fluid Mech.*, 222:647–663, 1991.

T. D. Papathanasiou, B. Markicevic, and E. D. Dendy. A computational evaluation of the ergun and forchheimer equations for fibrous porous media. *Physics of Fluids*, 13:2795–2804, 2001.

E. G. Patton and J. J. Finnigan. *Handbook of Environmental Fluid Dynamics, Volume One*. CRC Press/Taylor & Francis Group, LLC, 2013. ISBN 9781439816691.

N. Peller. *Numerische Simulation turbulenter Strömungen mit Immersed Boundaries*. PhD thesis, Technische Universität München, 2010.

N. Peller, A. Le Duc, F. Tremblay, and M. Manhart. High-order stable interpolations for immersed boundary methods. *International Journal for Numerical Methods in Fluids*, 52: 1175–1193, 2006.

S. B. Pope. *Turbulent Flows*. Cambridge University Press, 2000. ISBN 9780521598866. URL `http://books.google.de/books?id=HZsTw9SMx-0C`.

K. R. Rajagopal. On a Hierarchy of approximate models for flows of incompressible fluids through porous solids. *Mathematical Models and Methods in Applied Sciences*, 17(2):215–252, 2007. URL `http://www.worldscinet.com/m3as/17/1702/S0218202507001899.html`.

S. Rojas and J. Koplik. Nonlinear flow in porous media. *Phys. Rev. E*, 58:4776–4782, 1998.

D. Ruth and H. Ma. On the derivation of the forchheimer equation by means of the averaging theorem. *Transport in Porous Media*, 7:255–264, 1992.

E. Sanchez-Palencia. *Non Homogeneous Media and Vibration Theory, Lecture Notes in Physics*. Springer, 1980.

A. S. Sangani, D. Z. Zhang, and A. Prosperetti. The Added Mass, Basset, and Viscous Drag Coefficients in Nondilute Bubbly Liquids Undergoing Small-Amplitude Oscillatory Motion. *Phys. Fluids A*, 3:2955–2970, 1991.

D. Sanyal and N. Maji. Thermoregulation through skin under variable atmospheric and physiological conditions. *J. Theor. Biol.*, 208:451–456, 2001.

A. E. Scheidegger. *The Physics of Flow Through Porous Media*. Univ. of Toronto Press, 1960.

A. M. Shapiro. *Fractured porous media: equation development and parameter identification*. PhD thesis, Princeton Univ, 1981.

E. Skjetne and J.-L. Auriault. High-velocity laminar and turbulent flow in porous media. *Transport in Porous Media*, 36:131–147, 1999.

E. Skjetne, A. Hansen, and J. S. Gudmundsson. High-velocity flow in a rough fracture. *J . Fluid Mech.*, 383:1–28, 1999.

J. C. Slattery. Flow of viscoelastic fluids through porous media. *AIChE J.*, 13:1066–1071, 1967.

J. C. Slattery. Single-phase flow through porous media. *AIChE J.*, 15:866–872, 1969.

G. Smith. Comparison of stationary and oscillatory flow through porous media. Master's thesis, Queens' University, 1991.

C. K. Sollitt and R. H. Cross. Wave transmission through permeable breakwaters. In *Proc. 13th Coastal Eng. Conf., ASCE*, volume 3, pages 1827–1846, 1972.

H. P. A. Souto and C. Moyne. Dispersion in two-dimensional periodic porous media. part i. hydrodynamics. *Physics of Fluids*, 9:2243–2252, 1997.

Y. Swapna and S. V. K. Varmab. Exact solution of mhd mixed convection periodic flow in a rotating vertical channel with heat radiation. *Asia Pacific Journal of Research*, 1: 150–170, 2014. ISSN 2320-5504.

M. R. Tek, K. H. Coats, and D. L. Katz. The effect of turbulence on flow of natural gas through porous reserviors. *J. Petrol Technol.*, 14:799–806, 1962.

N. Tilton and L. Cortelezzi. Linear stability analysis of pressure-driven flows in channels with porous walls. *J . Fluid Mech.*, 604:411–445, 2008.

S. Wahid. *Novel Catalytic Material with Enhanced Heterogeneous Contacting Efficiency for VOC Removal at Ultra-short Contact Time*. PhD thesis, Auburn University, 2014.

C. Y. Wang. The starting flow in ducts filled with a Darcy–Brinkman medium. *Transport in Porous Media*, 75:55–62, 2008. ISSN 0169-3913. doi: 10.1007/s11242-008-9210-3. URL `http://dx.doi.org/10.1007/s11242-008-9210-3`.

S. Whitaker. Diffusion and dispersion in porous media. *AIChE J.*, 13:420–427, 1967.

S. Whitaker. Advances in the theory of fluid motion in porous media. *Ind. Eng. Chem.*, 61: 14–28, 1969.

S. Whitaker. Laws of continuum physics for single-phase, single-component systems. In G. Hetsroni, editor, *Handbook of Multiphase Systems*, pages 1–35. Hemisphere Publ., 1982.

S. Whitaker. Flow in porous media I: A theoretical derivation of Darcy's law. *Transport in Porous Media*, 1(1):3–25, 1986.

S. Whitaker. The Forchheimer equation: a theoretical development. *Transport in Porous Media*, 25(1):27–61, 1996.

J. H. Williamson. Low-storage Runge-Kutta schemes. *J. Comput. Physics*, 35(1):48–56, 1980.

G. C. Winston, B. B. Stephens, E. T. Sundquist, J. P. Hardy, and R. E. Davis. Seasonal variability in c02 transport through snow in a boreal forest. *Biogeochemistry of Seasonally Snow-Covered Catchm*, pages 2789–2797, 1995.

J. R. Womersley. Method for the calculation of velocities, rate of flow and viscous drag in arteries when the pressure gradient is known. *The Journal of Physiology*, 127:553–563, 1955.

T. Zhu and M. Manhart. Oscillatory darcy flow in porous media. *Transport in Porous Media, accepted*, 2015.

T. Zhu, C. Waluga, B. Wohlmuth, and M. Manhart. A study of the time constant in unsteady porous media flow using direct numerical simulation. *Transport in Porous Media*, 114:161–179, 2014.

Z. Żmudka and S. Postrzednik. Inverse aspects of the three-way catalytic converter operation in the spark ignition engine. *Journal of KONES Powertrain and Transport*, 18:509–516, 2011.